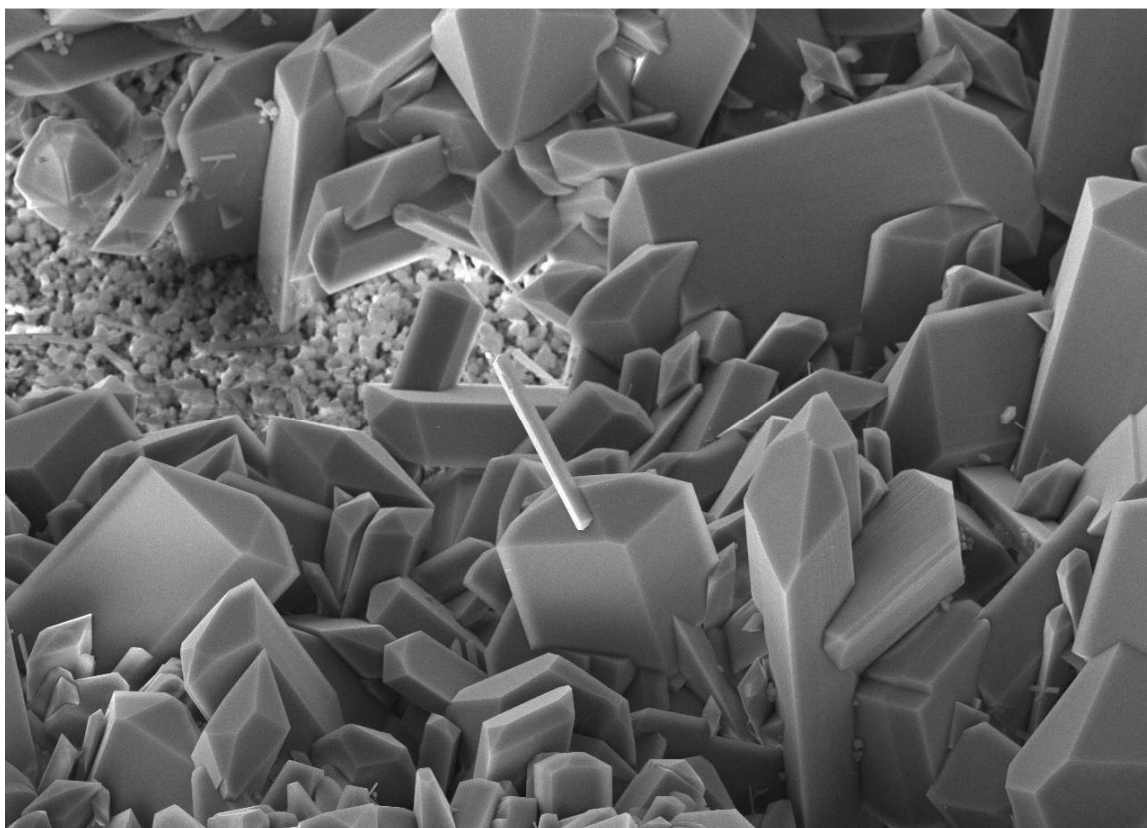


BOOK OF EXTENDED ABSTRACTS

**JOINT ANNUAL MEETING OF THE
SLOVAK SILICATE SCIENTIFIC-TECHNOLOGICAL
SOCIETY
&
WORKSHOP
PROCESSING AND PROPERTIES OF
ADVANCED CERAMICS**



Institute of Materials Research, Slovak Academy of Sciences, Košice, Slovak Republic

© 2015

BOOK OF EXTENDED ABSTRACTS

**JOINT ANNUAL MEETING OF THE
SLOVAK SILICATE SCIENTIFIC-TECHNOLOGICAL
SOCIETY**

&

WORKSHOP

**PROCESSING AND PROPERTIES OF
ADVANCED CERAMICS**

Organized by
Institute of Materials Research, Slovak Academy of Sciences, Košice
and
Slovak Silicate Scientific-Technological Society



November, 25 – 27, 2015 Hotel Lesanka-Košická Belá

Committee and Advisory Board:

Ján Dusza, IMR SAS, Košice

Pavol Šajgalík, IICH SAS, Bratislava

Dušan Galusek, VILA, Trenčín

František Lofaj, IMR SAS Košice

Organizing Committee:

František Lofaj

Alexandra Kovalčíková

Petra Hviščová

Published by:

Institute of Materials Research, Slovak Academy of Sciences, Košice, Slovak Republic

© 2015

Phone: +421 55 792 2402

Fax: +421 55 792 2408

http: www.imr.saske.sk

Autors: Alexandra Kovalčíková, Petra Hviščová

ISBN: 978-80-89782-03-1

Cover photo: Monika Tatarková, IMR SAS (corrosion of Al₂O₃ in water)

CONTENTS

MASTER SINTERING CURVE FOR ANISOTROPIC SYSTEMS V. Pouchlý	6
STUDY OF TRANSITION FROM OPEN TO CLOSED POROSITY STAGE DURING SINTERING OF ADVANCED CERAMIC MATERIALS T. Spusta	10
EFFECT OF ACIDIC AND BASIC MEDIA ON MECHANICAL PROPERTIES AND CORROSION RESISTANCE OF DENTAL CERAMICS A. Švančárková	14
PREPARATION OF POLYCRYSTALLINE CERAMIC NANOFIBERS E. Múdra	19
TECHNOLOGY AND MECHANICAL PROPERTIES OF CERAMIC COATINGS P. Hviščová	23
THERMAL STABILITY OF MULTICOMPONENT HARD COATINGS BASED ON NITRIDES M. Mikula	27
DEPOSITION OF HARD YET MODERATELY DUCTILE M_0BC COATINGS BY PULSED-DC MAGNETRON SPUTTERING P. Souček	32
Ti-B-Si-N COATINGS WITH ENHANCED THERMAL STABILITY PREPARED BY MAGNETRON SPUTTERING M. Pleva	36
ELECTRICALLY CONDUCTIVE COMPOSITES BASED ON SiC R. Bystrický	41
MICROSTRUCTURE AND MECHANICAL PROPERTIES OF ELECTRICALLY CONDUCTIVE SiC BASED CERMETS. M. Fides	46
PREPARATION AND CHARACTERIZATION OF SILICON NITRIDE - GRAPHENE COMPOSITES O. Hanzel	50
IMPROVEMENT OF MECHANICAL PROPERTIES OF B_4C CERAMIC COMPOSITES BY GRAPHENE PLATELETS ADDITION R. Sedlák	55
OXIDATION RESISTANCE OF HfO_2 DOPED ZrB_2-SiC CERAMICS. Ľ. Bača	59
DISLOCATION BASED PLASTICITY IN ZrB_2 MICROPILLARS T. Csanádi	63

HYDROTHERMAL CORROSION OF POLYMER DERIVED GLASS CERAMIC LAYERS	
I. Petříková	68
CORROSION OF METAL/GLASS JOINTS IN ACETIC ACID VAPOURS	
A. Nowicka	72
POLYMER DERIVED GLASS CERAMIC LAYERS FOR CORROSION PROTECTION OF METALS	
M. Parchovianský	77
THE EFFECT OF THERMAL TREATMENT OF Ce³⁺ DOPED GLASS ON LUMINESCENCE PROPERTIES IN THE SYSTEM Y₂O₃-Al₂O₃	
K. Haladejová	81
WILLEMITE BASED PHOTO LUMINESCENT MATERIALS. Grain morphology and florescent spectra by using different activators of luminescence.	
P. Švančárek	84
CRYSTALLIZATION KINETICS OF YTRIUM ALLUMINIUM GARNET	
J. Chovanec	89
USE OF THERMALLY STIMULATED LUMINESCENCE FOR DIAGNOSTIC OF PLASMA TREATED ALUMINA POWDER	
T. Morávek	93
VARIOUS SYNTHESIS ROUTES FOR PREPARATION OF CE-MN-DOPED SILICATE PHOSPHORS AND THEIR INFLUENCE ON LUMINESCENCE	
P. Veteška	98

UNIVERSÁLNÍ SLINOVACÍ KŘIVKA PRO ANISOTROPICKÉ SYSTÉMY

MASTER SINTERING CURVE FOR ANISOTROPIC SYSTEMS

V. Pouchlý¹, D. Drdlík¹, K. Maca¹²

¹ CEITEC BUT, Brno University of Technology, Technická 10, 616 00 Brno, Czech Republic

² Faculty of Mechanical Engineering, Brno University of Technology, Brno, Czech Republic

ABSTRACT

During a sintering of a multilayer composites, the densification is hindered by generated internal stresses. Retarded densification can be measured by means of high temperature dilatometry, which can be also used for calculation of activation energy of sintering process by Master Sintering Curve (MSC) theory. However, the raw MSC theory deals with isotropic densification. Therefore we modify the MSC theory for anisotropic systems. To experimentally clarify these modifications, we sintered multilayer alumina/zirconia composites prepared by EPD. MSC analysis revealed that for this composite, the sintering rate was rapidly hindered by interactions between individual layers which led to higher creep strain and surface rippling. MSC theory was also able to quantify the difference of activation energy in individual directions.

Keywords: sintering, multilayer ceramics, high-temperature dilatometry

INTRODUCTION

One of theories which is used for description of sintering process is the model of Master Sintering Curve [1] (MSC in the following). Three basic assumptions have to be fulfilled in this model:

- the grain size evolution in the course of sintering is independent of thermal history and it is only a function of density;
- the ceramic green bodies under evolution must have the same microstructure, i.e. they have to be prepared from the same powders by the same technology;
- one sintering mechanism dominates whole sintering process.

Under these conditions Hansen et al. [2] formulated following equation:

$$\frac{k}{\gamma\Omega D_0} \int_{\rho_0}^{\rho} \frac{(G(\rho))^n}{3\rho\Gamma(\rho)} d\rho = \int_0^t \frac{1}{T} \exp\left(-\frac{Q}{RT}\right) dt \equiv \Theta, \quad (1)$$

where γ is the surface energy, Ω is the atomic volume, k is the Boltzmann constant, R is the gas constant, T is the thermodynamic temperature, G is the mean grain size, ρ is sample density, D_0 is the coefficient of a diffusion process (only one dominant diffusion process is considered), Q is the activation energy of sintering, Γ represents scaling parameters that relate different geometric features as the driving force of sintering and the mean diffusion distance to the grain size, t is the time and n has the value 3 (for volume diffusion) or 4 (for grain boundary diffusion). When the above mentioned assumptions are fulfilled, the left side of Eq. (1) becomes only a function of density. Relation between density and function Θ (describing thermal history of the sintering with the help of parameter Q) is called MSC. The MSC model can be used for determination of sintering activation energy and also for prediction of sintering behaviour of any chosen heating profile, which can be helpful for optimizing the sintering schedule of multi layer materials.

It must be noted that above mentioned theory works with isotropic shrinkage only, therefore it is not suitable for anisotropic systems. The main goal of this work was to recalculate the MSC theory for shrinkage, instead of density, of the samples and to work with this modified MSC to judge the anisotropic sintering behaviour of alumina/zirconia composites.

EXPERIMENTAL

The monolithic alumina (A) and zirconia (Z) materials as well as layered alumina/zirconia (Z33=33%zirconia, Z50=50%zirconia) layered composites were prepared by EPD. The sintering of composites was performed at 1500°C with 2 h dwell with different heating rates 2, 5, 10, and 20°C/min and cooling rate 5°C/min in order to obtain different sintering profiles for MSC construction. All calculations associated with MSC model were performed with the help of an automatic procedure [3]. The composite was measured in longitudinal as well as in transversal direction (see Fig.1).

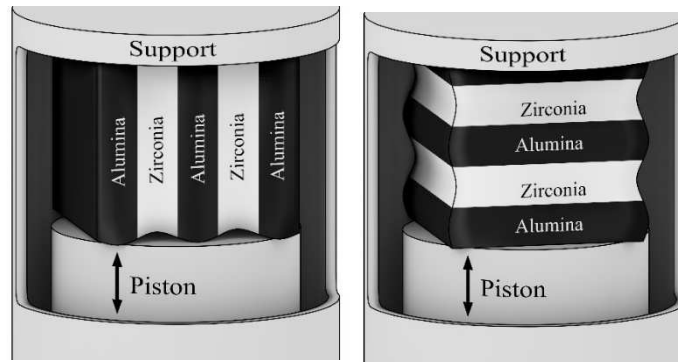


Fig. 1 Scheme of dilatometric measurement of ceramic laminate in the a) longitudinal direction b) transversal direction

RESULTS AND DISCUSSION

In presented laminates, the densification rate in the longitudinal direction exhibits only a small increase of densification rate at temperatures where zirconia layers should sinter, but the maximum densification rate was observed at the same temperature as was identified for alumina monolith (see Fig. 2). The sintering of individual layers led to a drag in of zirconia layers by alumina layers near the interface regions usually denoted as a surface rippling, as observed at the free edges [4]. Due to this phenomenon, the measured shrinkage (and shrinkage rate) in the longitudinal direction of Z50 and Z33 is mainly given by the shrinkage of alumina layers.

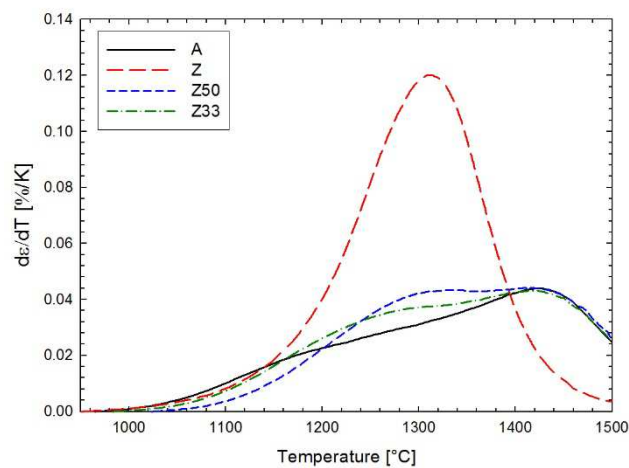


Fig. 2 Densification rates for heating rate 5°C/min in the longitudinal direction

In the longitudinal direction both Z50 and Z33 laminates exhibit higher activation energies of the sintering process than A and Z monoliths in the same direction. In the laminates, alumina and zirconia layers are strongly bonded and due to different shrinkage rate (see Fig.2) they sinter under compression and tension constraint. Constraint during sintering led to the hindering of densification that is reflected by the increase of activation energy of sintering.

CONCLUSIONS

The modification of the MSC theory allows its usage also for materials with anisotropic sintering behaviour. The activation energies of sintering of composites significantly differ for each compositions and investigated composite orientation. In the longitudinal direction, the composites exhibits activation energies with higher activation energies than in transversal directions. The sintering in a longitudinal direction was therefore hindered by the constraint between different layers and this retardation slightly increases with the number of interfaces.

ACKNOWLEDGEMENT

The authors gratefully acknowledge the funding provided by the Grant Agency of the Czech Republic under Grant no. 13-08717P and 15-06390S. This work was realized in CEITEC – Central European Institute of Technology with research infrastructure supported by the project CZ.1.05/1.1.00/02.0068 financed from European Regional Development Fund.

LITERATURE

- [1] Su, H. H., Johnson, D. L. Master sintering curve: A practical approach to sintering. *Journal of the American Ceramic Society* 1996;79:3211-7.
- [2] Hansen, J. D., Rusin, R. P., Teng, M. H., Johnson D. L. Combined-Stage Sintering Model. *Journal of the American Ceramic Society* 1992;75:1129-35.
- [3] Pouchly, V., Maca, K. Master Sintering Curve - A Practical Approach to its Construction. *Sci Sinter* 2010;42:25-32.
- [4] Chlup, Z., Hadraba, H., Drdlik, D., Maca, K., Dlouhy, I., Bermejo, R. On the determination of the stress-free temperature for alumina-zirconia multilayer structures. *Ceramics International* 2014;40:5787-93.

**ŠTÚDIUM PRECHODU ZO ŠTÁDIA OTVORENEJ DO ŠTÁDIA UZATVORENEJ
PÓROVITOSTI PRI SPEKANÍ POKROČILÝCH KERAMICKÝCH MATERIÁLOV**

**STUDY OF TRANSITION FROM OPEN TO CLOSED POROSITY STAGE DURING
SINTERING OF ADVANCED CERAMIC MATERIALS**

T. Spusta¹, K. Maca^{1, 2}

¹ *CEITEC - Central European Institute of Technology, Brno University of Technology, Brno,
Czech Republic*

² *Institute of Materials Science and Engineering, Brno University of Technology, Brno, Czech
Republic*

ABSTRACT

Hot isostatic pressing (HIP) is advanced sintering technique for processing of fully dense ceramic materials, which have variety of structural, biological or functional applications. For successful post-HIP treatment the presintered samples have to be air tight, i.e. without open porosity. The research in the field of transition from open to closed porosity stage is rarely published in the relevant literature, therefore the experimental and theoretical study of this phenomena for several ceramic materials (Al_2O_3 , c-ZrO_2 and MgAl_2O_3) was the main goal of this work. The results obtained in this work show that the critical density (relative density of transition from open to closed porosity stage) is material characteristics depending on the dihedral angle, in accordance with theoretical models of Beere and Carter & Gleaser.

KEYWORDS: Oxide ceramics, sintering, post-HIPing, open porosity, closed porosity

INTRODUCTION

One of the advanced technologies to produce ceramics with required microstructure (density and grain size) is a sintering process called “post-HIPing” which consists of pressure-less presintering followed by Hot Isostatic Pressing (HIP). HIP is a kind of pressure-assisted sintering (combination of high temperature and high gas pressure), which in this approach requires air tight sample surface, therefore only closed pores. The transition from open to closed pores occurs at high relative densities. According to sintering theory and literature data [1] this threshold value is a generalised number (usually 92% t.d.) independent of sintered material. However, in practice, the critical density (the relative density when transition occurs) is not identical for all materials as it can be found in various articles about post-

HIPing treatment [2-5]. The first theoretical approach dealing with pore closure is strictly geometrical theory by Budworth [6], which defines transition from open to closed pores at approx. 92% of relative density independently on material. More advanced models of Beere [7] and Carter & Gleaser [8] created dependency of critical density on dihedral angle.

Up to now the conditions for post HIP treatment were determined mostly from expensive and time consuming trial-and-error experiments, therefore the deep research in this field is highly desirable. The goal of this study was to experimentally evaluate the critical density (relative density of transition from open to closed porosity stage) for various ceramic materials and compare them with theoretical models and other available literature data.

EXPERIMENTAL PART

Three different ceramic materials were used for experiments performed in this work. These materials have different crystallographic structures and different particle size. Totally 6 commercially produced ceramic powders were used in this work - three α -Al₂O₃ powders with particle size 100nm (Taimicron, Taimei Chemicals), 240nm (Reynolds, Malakoff Industries) and 300nm (AKP30, Sumitomo), two c-ZrO₂ powders with particle size 80nm (TZ-8Y, Tosoh) and 140nm (TZ-8YSB, Tosoh) and one MgAl₂O₄ powder with particle size 58nm (Baikalox S30CR, Baikowski).

These powders were formed by cold isostatic pressing using pressures 100MPa and 300MPa. Samples were sintered in pressure-less super-kanthal furnace at various temperatures (1300 – 1600°C) to achieve volume of open pores (V_o) to be close to 0%. Density of sintered samples and ratio of open and closed porosity were measured by Archimedes method (EN 623-2).

RESULTS

Fig. 1 shows the comparison among experimental data acquired in this paper, from the literature and from the theoretical models (these models used literature data of dihedral angle at the sintering temperatures 1300 – 1600°C - see *Tab. 1*). To be able to compare all data, the experimental results of this work, as well as experimental results from literature are present as an average value for given material regardless of initial particle size and shaping methods.

Tab. 1: Dihedral angle and calculated critical relative density by two used models

Material	ψ (for 1300 - 1600 °C)	Beere's model	C&G's model
Al ₂ O ₃	159.5°	93.6% t.d.	93.0% t.d.
ZrO ₂ (8% Y ₂ O ₃)	165.5°	93.2% t.d.	92.6% t.d.
MgAl ₂ O ₄	157.5°	93.7% t.d.	93.1% t.d.

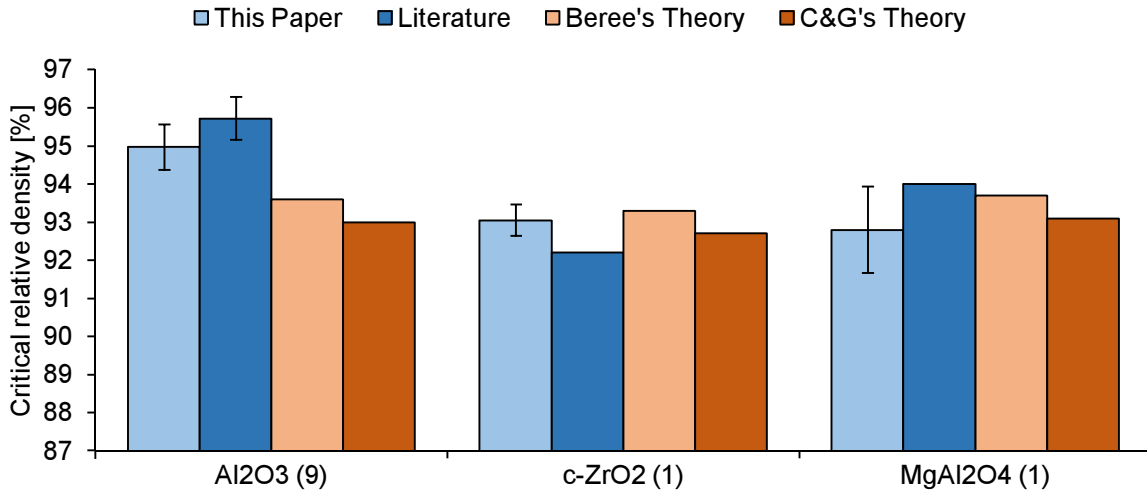


Fig. 1: Summarized comparison of critical density of all available data. Numbers next to labels represent amount of articles with critical density information.

Theoretical models exhibit that critical density is only material characteristics depending only on interfacial energies, thus on dihedral angle, independently on particle size and microstructure of green body. For cubic systems (c-zirconia and spinel) one can see that experimental values both from this work and from experiments in the literature agreed very well with theoretical models. Experimental results obtained with alumina ceramics exhibit slightly higher values of critical density than theoretical models predict. This feature will be the subject of further investigation.

CONCLUSIONS

According to authors' knowledge, in this paper it has been performed the most extensive research of critical density. It has been analysed using two theoretical models how dihedral angle in various ceramic materials influences the critical density. These values were confronted with the experimental values obtained in this work and with experimental values used in post-HIP treatments acquired from the literature. The results confirm the theoretical assumption that critical porosity is namely material characteristics depending on the dihedral angle.

ACKNOWLEDGEMENTS

The authors gratefully acknowledge the funding provided by the Grant Agency of Czech Republic under Grant no. 15-06390S. This work was realized in CEITEC supported by the project CZ.1.05/1.1.00/02.0068 financed from European Regional Development Found.

REFERENCES

- [1] KANG, S. J-L. Sintering: densification, grain growth, and microstructure. Elsevier Butterworth-Heinemann, 2005, 265 s.
- [2] TRUNEC, M., MACA, K., CHMELIK, R. Polycrystalline alumina ceramics doped with nanoparticles for increased transparency. Journal of the European Ceramic Society, vol. 35, issue 3 (2015)
- [3] LACH, R. et al. From nanometric zirconia powder to transparent polycrystal, Journal of the European Ceramic Society, vol. 34, issue 16 (2014), p. 4321-4326.
- [4] KLIMKE, J., TRUNEC, M., KRELL, A. Transparent Tetragonal Ytria-Stabilized Zirconia Ceramics: Influence of Scattering Caused by Birefringence. Journal of the American Ceramic Society, vol. 94, issue 6 (2011), p. 1850-1858
- [5] KIM, J-Y., UCHIDA, N., SAITO, K. Analysis of Hot Isotatic Pressing of Presintered Zirconia. Journal of the American Ceramic Society. vol. 73, issue 4 (1990), p. 1069-1073
- [6] BUDWORTH, W.D. Theory of Pore Closure during Sintering. Transactions of the British Ceramic Society. vol. 69 (1970), p. 29-31.
- [7] BEERE, W. A unifying theory of the stability of penetrating liquid phases and sintering pores, Acta Metallurgica, vol. 23, issue 1 (1975), p. 131-138.
- [8] CARTER, W.C., GLAESER, A.M. The morphological stability of continuous intergranular phases: Thermodynamic considerations. Acta Metallurgica, vol. 35, issue 1 (1987), p. 15-26.

VPLYV ZÁSADITÉHO A KYSLÉHO PROSTREDIA NA MECHANICKÉ VLASTNOSTI A KORÓZNU ODOLNOSŤ DENTÁLNEJ KERAMIKY

EFFECT OF ACIDIC AND BASIC MEDIA ON MECHANICAL PROPERTIES AND CORROSION RESISTANCE OF DENTAL CERAMICS

A. Švančárková^{1,2}, D. Galusková¹, J. Balko³, M. Fides³, D. Galusek¹

¹*Vitrum Laugaricio – Joint Glass Center of the Institute of Inorganic Chemistry, SAS, Alexander Dubček University of Trenčín, and Faculty of Chemical and Food Technology, Slovak University of Technology, Študentská 2, 911 50 Trenčín,*

²*Faculty of Chemical and Food Technology STU, Radlinského 9, 812 37 Bratislava, Slovakia*

³*Institute of Materials Research, Slovak Academy of Sciences, Watsnova 47, SK-043 53 Košice, Slovakia*

ABSTRACT

The objective of this study was to evaluate the effect of acidic and basic media on mechanical and chemical properties of three different types of lithium disilicate glass ceramics. The influence of 4% acetic acid (pH=2.4) and a basic solution (pH=10) on microhardness, wear resistance and corrosion resistance of lithium disilicate dental ceramics was studied. Dynamic testing in 4% acetic acid had impact on increase of wear rate of all types lithium disilicate ceramics. Static test in 4% acetic acid (16h, 80°C) caused increase of wear resistance of tested samples. The major elements leached from dental ceramics were lithium, phosphorus and potassium in the acidic environment, and phosphorus, lithium and silicon in basic solutions.

Keywords: lithium disilicate dental ceramics, corrosion, microhardness, wear

INTRODUCTION

IPS e. max CAD is a lithium disilicate glass-ceramic (LS₂) that has been designed for the CAD/CAM technique used in dental restoration. As lithium disilicate is very difficult to machine with diamond tools because of low edge stability and brittle glass base, other procedures had to be explored in order to allow this glass-ceramic to be machined with CAD/CAM equipment. This challenge was met with the development of an intermediate phase, lithium metasilicate. In the partially crystallized stage the material has very low chemical durability and poor mechanical properties. However, these properties change

significantly during the process of crystallization at about 850°C in which the lithium metasilicate is transformed into a durable lithium disilicate glass-ceramics.

Dental glass-ceramic materials are generally considered as chemically inert restorative materials. However, exposure to acidic and basic agents from food and beverages, exposure time and temperature were found to influence the durability of dental ceramics [1]. The pH range experienced in the oral cavity ranges from 1 to 10 with highly acidic conditions associated with reflux of gastric fluid. [2]. The aim of this study was to monitor the effect of basic and acidic media on mechanical properties (wear resistance and microhardness). Three types of samples with different heat treatment were tested before and after corrosion process.

EXPERIMENTAL

Three types of lithium disilicate glass ceramics were studied before and after corrosion process. Partially crystallized lithium metasilicate glass ceramics were sintered to fully crystallized lithium disilicate dental ceramics using three different two-stage heat treatment regimes: A - 500°C/2 h, 850°C/2 h; B - 500°C/1 h, 820°C/1 h; C - 850 °C/1h. The temperatures of the two stage regime were determined on the basis of data obtained from literature, where the first temperature was applied to nucleate lithium disilicate, while the second temperature was used to grow the lithium disilicate crystals [3]. This way the materials with various mechanical properties and corrosion resistance were prepared. The influence of corrosion process on properties of dental glass ceramics was monitored on the basis of results from the tests carried out under quasi-dynamic and under static conditions. Quasi-dynamic test was performed at the temperature corresponding to the temperature of human body (37°C).

Under quasi-dynamic conditions the samples were corroded in 4% acetic acid and in basic solution (pH 10) for 96 h with exchange of the corrosion medium for a fresh one in 12 h intervals. Under static conditions the samples were tested at 80°C for 16 h without a change of the corrosion medium of 4% acetic acid (according to the ISO 6872 Standards for hydrolytic resistance of dental ceramics materials) [4]. Before and after the corrosion process, the glass-ceramic samples were mechanically tested to determine the microhardness and wear. The microhardness was determined on mechanically polished surfaces of dental ceramics before and after corrosion at the load of 9.8N.

Two-body in vitro wear tests were conducted using tribometer. To better simulate real wear conditions of dental material, the choice of these parameters was based on clinical experience

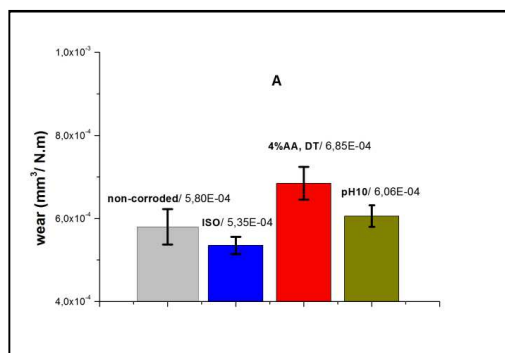
and the literature [5]. Wear testing was carried out on the tribometer in dry conditions using ball-on-flat technique. The tribological partner was a highly polished alumina ball with 6.35 mm diameter, the applied load was 10N, sliding speed 10 cm/s and sliding distance was 50 m.

RESULTS

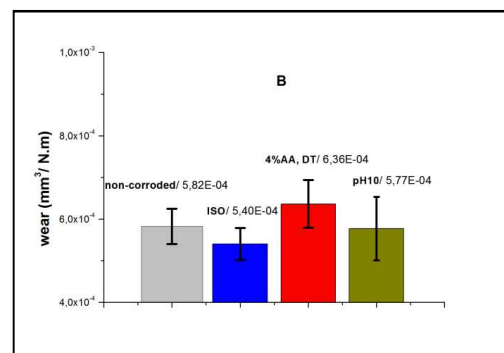
The same microhardness was observed for samples A and B (625 HV1), the lowest for the sample C (607 HV1). The Vickers hardness decreased most after corrosion process in sample A. Decrease of hardness after corrosion process for samples B and C has not been so significant.

For dynamic corrosion conditions in 4% acetic acid for all types of samples the wear rates increased in comparison to uncorroded specimens. The highest decrease of wear resistance was observed for sample A after corrosion in 4% acetic acid after 96 h of dynamic corrosion test ($6.85 \cdot 10^{-4} \text{ mm}^3/\text{N.m}$). Dynamic testing in acidic media (4% acetic acid) had higher impact on increase of wear of tested lithium disilicate ceramics than dynamic testing in basic media at pH 10 (*Fig.1*). Wear resistance after 16 h of static testing at 80 °C increased in all tested samples.

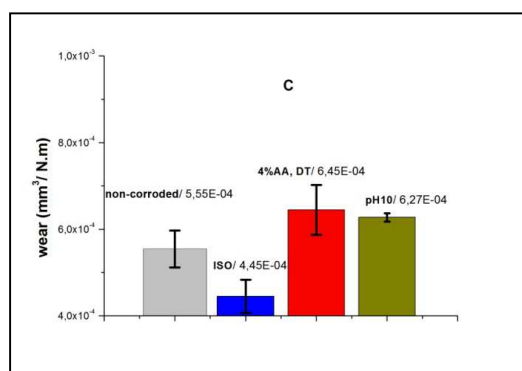
The contents of the elements leached into the solution of corrosion media during corrosion were determined by atomic emission spectrometry with inductively coupled plasma (ICP-AES). The major elements leached from dental ceramics were lithium, phosphorus and potassium in the acidic environment, and phosphorus, lithium and silicon in basic solutions. Samples B were the most resistant in the acid environment of 4% acetic acid. Corrosion resistance in alkaline medium was very similar in all samples, and linear increase in concentration of leached elements (Li, P, Si) to basic medium (pH 10) was determined.



a,



b,



c,

Fig.1 Wear rates of lithium disilicate glass ceramics by non-corroded sample, after static for 16 h at 80°C (ISO 6872) and dynamic test for 96 h (4% AA, DT) in 4% acetic acid and after dynamic test in basic solution (pH 10) a) type A, b) type B, c) type C

CONCLUSIONS

In this study a linear increase in concentration of leached elements (Li, P, K) from lithium disilicate glass ceramics to acidic media of 4% acetic acid was observed. The sample B appears to be the most resistant to the corrosion influence of 4% acetic acid. Linear increase in concentration of leached elements (Li, P, Si) to basic medium (pH10) was determined, while corrosion resistance in alkaline medium similar in all tested samples was comparable. Dynamic corrosion process in acidic and basic medium causes decrease of wear resistance of all tested dental material, which might result in permanent damage or total failure of dental restoration after prolonged or repeated exposure to both acidic and basic components of food.

ACKNOWLEDGEMENT

The financial support of this work by the grant VEGA 2/0058/11, and the grant APVV 0218-11 is gratefully acknowledged. This publication was created in the frame of the project "Centre of excellence for ceramics, glass, and silicate materials" ITMS code 262 201 20056, based on the Operational Program Research and Development funded from the European Regional Development Fund.

LITERATURE

- [1] Peampring, Ch., Sanohkan, S.: All-ceramic systems in Esthetic Dentistry: A review, Dental Journal 2012, 82-92.
- [2] Kang, S., Chang, J., Son, H.: Flexural strength and microstructure of two lithium disilicate glass ceramics for CAD/CAM restoration in the dental clinic, Restorative Dentistry and Endodontics, 2013, 134-140.

[3]Sobrinho, L.C, Knowles, J.C., Glover, R.H., Cattell, M.J.: Comparison of the wet and dry fatigue properties of all ceramic crowns, *Jornal of materials science: Material in medicine* 9, 1998, 517-521.

[4] Anusavice, K.J., Zhang, N.: Chemical durability of Dicor and lithia-based glass-ceramics, *Dent Mater* 13, 1997, 13-19.

[5] Wang, L., Liu, Y., Si, W., Feng, H., Tao, Y., Ma, Z.: Friction and wear behaviors of dental ceramics against natural tooth enamel, *Journal of the European Ceramic Society* 32, 2012, 2599-2606.

PRÍPRAVA POLYKRYŠŤALICKÝCH KERAMICKÝCH NANOVLÁKIEN

PREPARATION OF POLYCRYSTALLINE CERAMIC NANOFIBERS

E. Múdra¹, H. Bruncková¹, M. Strečková¹, J. Dusza¹, T. Sopčák¹, V. Girman²

¹*Institute of Materials Research, Slovak Academy of Sciences, Watsonova 47, 04001 Košice, Slovak Republic*

²*Institute of Physics, Faculty of Science P.J. Safarik University, Park Angelinum 9, 04001 Košice, Slovak Republic*

ABSTRACT

This paper is focused on a synthesis of ceramic polycrystalline nanofibers based on perovskite lanthanum tantalate $\text{La}_{1/3}\text{TaO}_3$ (LT) prepared by needleless electrospinning and post-electrospinning processes. The stabilization and calcinations temperatures of final fibers were 80, 250, 400, 900, and 1100 °C in air after the electrospinning. The present study focuses on a consecutive transformation from the initial amorphous phase through the pyrochlore to the final perovskite nanofibers during the thermal treatment. The PVA/LT and LT fibers were analyzed by X-ray diffraction analysis, a Raman spectroscopy, the scanning and transmission electron microscopy.

Keywords: Electrospinning, Ceramic nanofibers, Perovskite, $\text{La}_{1/3}\text{TaO}_3$

INTRODUCTION

Electrospinning is the simple and versatile method that produces nanofibers from a polymer solution. The high surface area to volume ratio in synergy with a desirable porosity of ceramic nanofibers is a key factor, which provides an extraordinary number of application opportunities. Perovskite tantalates of $\text{R}_{1/3}\text{TaO}_3$ based on rare-earth (R = La, Ce, Nd, Eu) elements represent progressive technological benefits in the form of ferroelectric ceramics and thin films for their dielectric, ferroelectric, electrolytic and magnetic properties enabling application for example in microelectromechanical systems (MEMS) [1].

EXPERIMENTAL

The polymer composite solution PVA/LT sol was composed of 7 % polyvinyl alcohol (PVA) with 5 % of H_3PO_4 and LT sol prepared by polymeric complex sol–gel method [2] mixed in the ratio 2:1. The stabilization and calcinations temperatures of final fibers were 80, 250, 400, 900 and 1100 °C for 1 hour in air with a heating rate of 1°C/min after the electrospinning. The transformation process started from 400 °C, where only the amorphous phase was found. A gradual crystallization to fluorite orthorhombic crystal structure continued up to 800 °C [2]. After annealing at 900 °C, the metastable $\text{La}_{4.67}\text{Ta}_{22}\text{O}_{62}$ transformed to the perovskite tetragonal $\text{La}_{0.33}\text{TaO}_3$ and the pyrochlore orthorhombic $\text{LaTa}_7\text{O}_{19}$ phases. At 1100 °C calcination, the phase composition was the major perovskite and the minor pyrochlore. Fig. 1a shows XRD patterns of PVA/LT fiber, which forms amorphous phase at 400 °C in contrast to perovskite and pyrochlore crystal phases formed at 900-1100 °C. The Raman spectra of PVA/LT fibers at 80 °C and after calcinations in the temperature interval 250-1100 °C are shown in Fig. 1b. The bands in the range of 450-950 cm^{-1} were assigned to the stretching modes of Ta-O bands with different strengths [3].

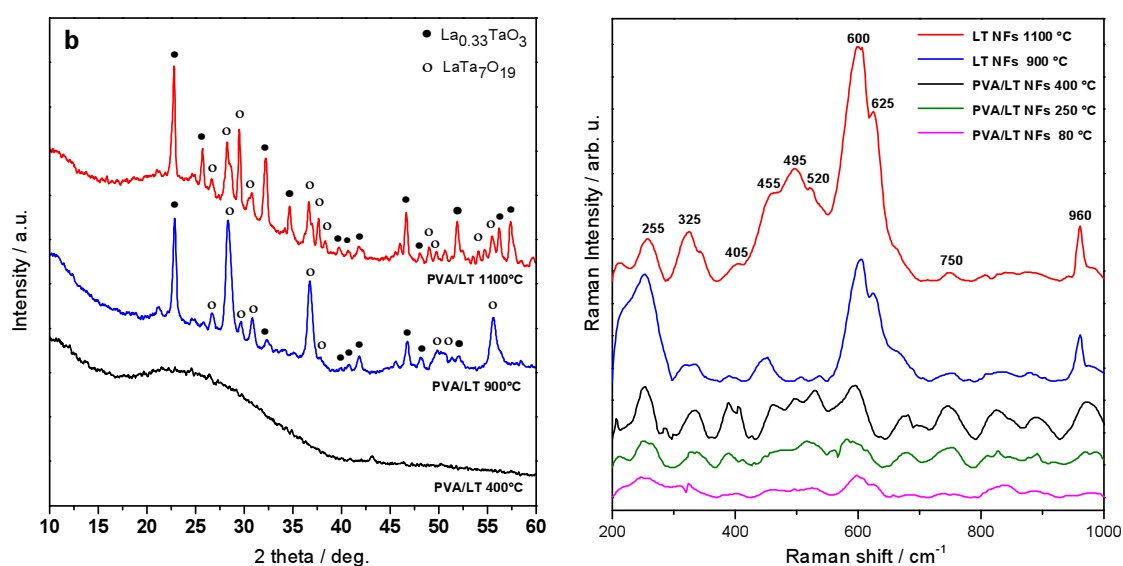


Fig. 1a) XRD patterns of PVA/LT and LT fibers after calcination at 400-1100 °C, b) Raman spectra of composite PVA/LT fibers at 80 °C -1100 °C

The evolution of morphology and microstructures of PVA/LT nanofibers during subsequent heat treatment at 80, 250, 400 and 900 °C are shown in Fig. 2. The uncalcinated precursor nanofibers had smooth surface with diameters around 100-200 nm, Fig. 2a. The fibers became thinner and porous when the PVA/LT was annealed at final temperatures, Fig. 2d.

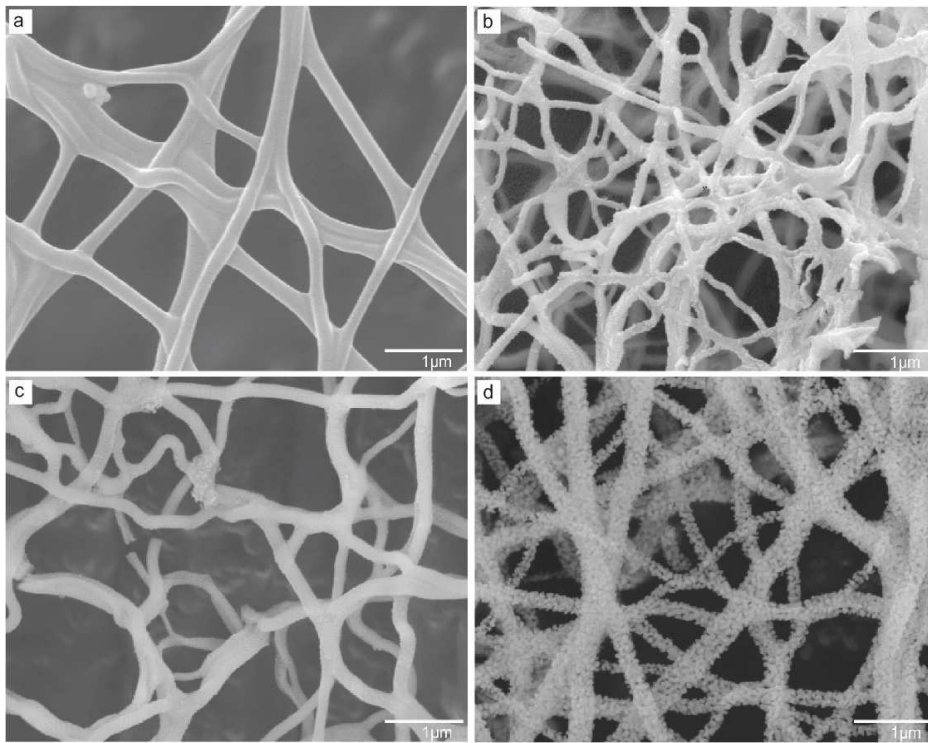


Fig. 2 SEM microstructures of PVA/LT nanofibers a) after stabilization at 80 °C and annealing at b) 250 °C, c) 400 °C and (d) 900 °C

Fig. 3 shows TEM images of the prepared fibers after annealing at 900 °C. The polycrystalline nanofiber composed of irregularly shaped nanograins of the tetragonal $\text{La}_{0.33}\text{TaO}_3$ and orthorhombic $\text{LaTa}_7\text{O}_{19}$ phase with the approximate size 20-50 nm were found after the thermal treatment. The analysis of electron diffractogram of the LT fibers has clearly verified an existence of two different LT phases after annealing at 900 °C.

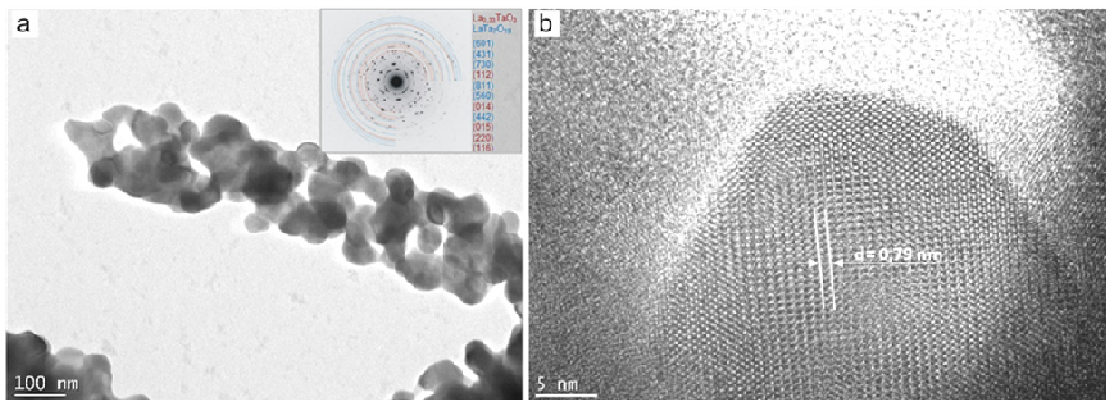


Fig. 3a) TEM image of LT fibers after annealing at 900 °C with electron diffractogram of the tetragonal and orthorhombic phases, b) HRTEM image of $\text{La}_{0.33}\text{TaO}_3$ grain

CONCLUSION

The ceramic LT nanofibers were prepared by the electrospinning and post-electrospinning processes from PVA and LT sol. The PVA and organic compounds completely decompose at temperatures higher than 500 °C. XRD analyses has confirmed that the phase transformation from the amorphous phase at 400 °C to the major perovskite $\text{La}_{1/3}\text{TaO}_3$ phase and the minor pyrochlore $\text{LaTa}_7\text{O}_{19}$ phase occurs in fibers at the annealing temperatures 900 °C and 1100 °C. Raman spectra have verified different lanthanum tantalate structures of the LT fibers at 400, 900 and 1100 °C. The microstructure analysis indicates a strong effect of the annealing temperature on the final morphology of LT fibers. HRTEM and SAED patterns have confirmed a presence of the major $\text{La}_{0.33}\text{TaO}_3$ phase in the fibers at 900 °C. The ceramic LT nanofibers were used as sensitive layers for resistive chemical sensors showing high sensitivity and reproducibility.

ACKNOWLEDGMENTS

This work was supported by the Operational Program “Research and Development” financed through European Regional Development Fund through project „Research Centre of Advanced Materials and Technologies for Recent and Future Applications “PROMATECH” and the project NanoCEXmat II: ITMS 262201220035.

REFERENCES

- [1] Kennedy, B. J., Howard, C. H. J., Kubota, Y., Kato, K. Phase transition behavior in the A-site deficient perovskite oxide $\text{La}_{1/3}\text{NbO}_3$. *Journal of Solid State Chemistry*, 2004, 4552-4556
- [2] Brunckova, H., Medvecký, L., Durisin, J., Girman, V. Phase transformation and particle morphology of perovskite $\text{La}_{1/3}\text{TaO}_3$ precursors prepared by polymeric tartrate complex sol-gel method. *Materials Letters*, 2014, 184-186
- [3] Noked, O., Melchior, A., Shuker, R., Livneh, T., Steininger, R., Kennedy, B. J., Sterer, E. Pressure-induced amorphization of $\text{La}_{1/3}\text{TaO}_3$. *Journal of Solid State Chemistry*, 2013, 38-42

TECHNOLÓGIA A MECHANICKÉ VLASTNOSTI KERAMICKÝCH POVLAKOV

TECHNOLOGY AND MECHANICAL PROPERTIES OF CERAMIC COATINGS

P. Hviščová^{1,2}, F. Lofaj¹, M. Novák^{1,3}, M. Ferdinandy¹

¹*Institute of Materials Research of Slovak Academy of Sciences, Watsonova 47, Košice, Slovakia*

²*Faculty of Metallurgy, Technical University of Košice, Park Komenského 11, 040 01 Košice, Slovakia*

³*Slovak University of Technology, Faculty of Materials Science and Technology, Institute of Materials Science, Bottova 25, Trnava, Slovak Republic*

ABSTRACT

This work is focused on the comparison of magnetron sputtering deposition technologies including DC MS (direct current magnetron sputtering), MPP (modulated pulse power) and HiPIMS (high power impulse magnetron sputtering) and their effect on the coating properties. Tungsten carbide and chromium nitride coatings properties were studied as a function of deposition parameters. They involve working pressure, reactive gas ratio and negative bias in DC MS and in the pulsed regimes, power density, frequency of pulse and duty cycle. The coatings prepared by DC MS and MPP had a similarly hardness, deposition rate and other properties. In the case of HiPIMS coating the deposition rate was significantly lower compared to DC MS.

Keywords: DC magnetron sputtering, MPP, HiPIMS, W-C coatings, Cr-N coatings

INTRODUCTION

In the present W-C a Cr-N coatings are attractive for the industrial applications because of good wear resistance and higher hardness. The chromium nitride coatings achieved relatively high hardness (20 – 25 GPa), good adhesion to substrate and good corrosion resistance. However, they have superior properties such as Titanium, they are studied less [1-5]. The structure, phase composition, grain size, texture and their properties are dependent on the nitrogen content, substrate temperature, power density, duty cycle and negative bias. Cr-N coatings can be formed several phases: Cr, Cr₂N, CrN or mixture of these phases depending on nitrogen content [6-9]. Tungsten carbide coatings are characterised by high hardness (~ 40 GPa) and relatively low coefficient of friction (~ 0.2). One possibility of achieving a

high hardness is to create nanocomposite structure, which consists of nanocrystallite WC in the amorphous C or DLC matrix [10, 11]. In the case of DC magnetron sputtering, W-C coatings are substoichiometric therefore it is necessary add carbon in form reactive gas. For example Czyzniewski et al. [12, 13] used reactive sputtering with acetylene for creation of WC/a-C:H coatings. They reached hardness up to 45 GPa and low CoF (~ 0.18) at the same time.

The aim of this work was to investigate the dependencies of mechanical properties of W-C and Cr-N coatings on the deposition parameters in three different regimes of magnetron sputtering: DC MS (direct current magnetron sputtering), MPP (modulated pulse power) and HiPIMS (high power impulse magnetron sputtering).

EXPERIMENTAL DETAILS

Tungsten carbide and chromium nitride was deposited by DC MS, MPP and HiPIMS regime in the equipment Cryofox Discovery 500. Constant power 150 W and deposition time 20 minutes were used for DCMS W-C coatings. The working pressure was in the range 0.25 – 1.2 Pa. C_2H_2 , N_2 , N_2+SiH_4 and their mixtures, 1 – 9 vol % from total gas flow were used as a reactive gas. In the case of pulse regime, W-C coatings were prepared with constant working pressure 0.5 Pa and 2 vol. % acetylene. The power densities were 0.22 – 3.86 kW/cm². The frequency was varied from 60 to 600 Hz. The duty cycle was in the range 0.4 – 6 %. In the both cases, the influence of negative bias was studied in the interval from floating bias (≈ -20 V) to -300 V.

CrN coatings were deposited by DC MS with constant power of 700 W under pressure of 0.2 – 1.2 Pa and with nitrogen content of 0 – 70 vol. % from total gas flow. The negative bias was the same as for W-C coatings. Constant pressure of 0.5 Pa and nitrogen content of 48 vol. % were used for HiPIMS regime. The power density was in the interval 0.5 – 2 kW/cm². The influence of duty cycle was monitored in the range from 0.2 to 0.8 %.

The thickness, hardness and indentation modulus were measured on the coatings. TEM, SEM and XRD diffraction was carried out in the some cases to determine the impact deposition conditions on the coatings properties.

RESULTS

The coatings prepared by DC MS were used as a reference material. The deposition rate increased with increase working pressure from 0.2 to 0.5 Pa and further increase of the pressure did not caused significant change of deposition rate. The addition of reactive gas – acetylene has the greatest impact to deposition rate. The negative bias has a positive influence only to -150 V, over this value deposition rate decreased. The deposition rates of the coatings deposited in pulse regime were assessed as a function of the power density, frequency of pulse and duty cycle. The deposition rate in this case was increased when power density and duty cycle has been growing. The duty cycle less than 1 % resulted in dramatic decreasing of the deposition rate below 10 nm/min. W-C coatings deposited by both regime were primarily amorphous, the phase composition changed according to the volume fraction of the acetylene: the coatings consisted from mixture of the $W_2C + WC_{1-x}$ phases for lower acetylene contents up to $WC_{1-x} +$ free carbon for higher C_2H_2 contents. The coating composition strongly affected their final properties: the MPP coatings hardness was around 18-22 GPa, whereas DC MS W-C coatings had a hardness in the range 15-21 GPa. Coefficient of friction could be reduced below 0.2 when the carbon amount in the coating was sufficiently high.

The deposition rate of Cr-N coatings prepared by DC MS was in the range 80 – 160 nm/min depending deposition conditions especially on nitrogen volume fraction. The deposition rate dramatically decreased from 160 nm/min for pure Cr coating to 80 nm/min when the nitrogen content was 70 vol. %. The deposition rate in the HiPIMS regime was significantly lower (< 5 nm/min) than in the DC regime. Both type of coatings has a textured nanocrystalline structure, consisting of columnar grains with diameter up to 25 nm. The phase composition changed with the increase of nitrogen content in the Ar atmosphere from Cr via Cr_2N to near stoichiometric CrN, which strongly affected hardness and coefficient of friction. The maximum Cr-N hardness was ~ 22 GPa for 50 vol % N_2 in the Ar atmosphere, whereas the lower hardness values of HiPIMS Cr-N were strongly affected by substrate due to considerably thickness lower. The coefficient of friction of Cr-N coatings was in the range 0.4-0.6.

CONCLUSION

The deposition rate and hardness of W-C coatings deposited by DC MS and MPP were comparable, with a slight improvement in hardness in the case of MP regime. The coefficients of friction W-C coatings prepared by DC MS were around 0.4 – 0.5 whereas for MPP regime

the values were below 0.3. MPP pulse mode was more advantageous in terms of deposition rate and consequently the achieved hardness and friction coefficient due to significantly higher power density. The deposition rates of DC MS Cr-N coatings were 10 – 20 times higher than those of HiPIMS mode due to too short pulses. To achieve of the better mechanical and tribological properties of Cr-N coatings prepared by HiPIMS mode, the next optimization in the Cr-N system is necessary.

ACKNOWLEDGEMENTS

This work has been supported by the Ministry of Education of the Slovak Republic and the Slovak Research and Development Agency under the contract numbers APVV-14-0173 and VEGA 2-098/14

REFERENCES

- [1] Liu B.: Corros. Sci. 43, 1953 (2001)
- [2] Baba K., Hatata R.: Surf. Coat Technol. 66, 368 (1994)
- [3] Ibrahim M. A. M., Korablov S. F., Yoshimura M.: Corros. Sci. 44, 298 (2002)
- [4] Navinsek B., Panjan P., Milosev I.: Thin Solid Films 281 – 282, 298 (1997)
- [5] Sant S. B., Gill K. S.: Surf. Coat. Technol. 68 – 69, 152 (1994)
- [6] Ehisarian A. P., Hovsepien P. E., Hultman L., Helmersson U.: Thin Solid Films 457, 222
1. (2004)
- [7] Foriés E., Escobar Galindo R., Sánchez O., Albella J. M.: Surf. Coat. Technol. 200, 6047
2. (2006)
- [8] Wei G., Scharf T. W., Zhou J. N., Huang F., Weaver M. L., Barnard J. A.: Surf. Coat.
Technol. 146/147, 357 (2001)
- [9] Lin J., Moore J. J., Mishra B., Sproul W. D., Rees J. A.: Surf. Coat. Technol. 201, 4640
(2007)
- [10] Radic N., Grzeta B., Milat O., Ivkov J., Stubicar M.: Thin solid films 320 (1998) 192
- [11] Voevodin A. A., O'Neill J. P., Zabinski J.S.: Surf. Coat. Technol. 116-119 (1999) 34
- [12] Czyzniewski, A.: Thin Solid Films 433 (2003) 180
- [13] Czyzniewski A., Precht W.: J. Mat. Proc. Technol. 157-158 (2004) 274

TEPLOTNÁ STABILITA MULTIKOMONENTNÝCH NITRIDOVÝCH TVRDÝCH VRSTIEV

THERMAL STABILITY OF MULTICOMPONENT HARD COATINGS BASED ON NITRIDES

M. Mikula^{1,2}, D. Plašienka¹, T. Roch¹, K. Štyráková¹, L. Satrapinsky¹, M. Drienovský³, V. Girman⁴, B. Grančič¹, A. Pleceník¹ and P. Kúš¹

¹*Faculty of Mathematics Physics and Informatics, Comenius University, Mlynská dolina, Bratislava, Slovakia*

²*Institute of Materials and Machine Mechanics, SAS Račianska 75, Bratislava, Slovakia*

³*Slovak University of Technology in Bratislava, Faculty of Materials Science and Technology in Trnava, Paulinska 16, 917 24 Trnava, Slovakia*

⁴*Department of Condensed Matter Physics, Institute of Physics, P.J. Šafárik University, Park Angelinum 9, Košice, Slovakia*

ABSTRACT

Alloying of transition metal nitrides (TMAIN) with additional elements (Nb, Ta, V, Mo, W and Y) is a promising concept for improving their thermal stability. In this work, analysis of structural evolution and oxidation resistance of reactively sputtered CrAlYTaN with Ta content 0÷10.4 at.% is presented. The presence of Ta in the solid solution shifts the start of decomposition process to higher temperatures (> 1000°C for Ta content of 10.4 at.%), leading to improvement of thermal stability compared to CrAlYN (~ 900°C).

Keywords: hard coatings, Cr-Al-Y-Ta-N, magnetron sputtering, thermal stability,

INTRODUCTION

Typical representatives of nanostructured hard coatings are ternary and quaternary transition metal nitrides (TMNs - Ti-, Cr-, ZrN), where their attractive mechanical and chemical properties arise mainly from strong bonds between the atoms, which can generally be present as mixtures of metallic, ionic and covalent contributions. The structures of most commonly ternary Al-containing $Ti_{1-x}Al_xN$ and $Cr_{1-x}Al_xN$ coatings consist of metastable face-centered cubic NaCl-type (B1) *fcc*-TiAlN and *fcc*-CrAlN solid solutions. However, diffusion-driven processes activate enough energy to initiate decomposition at sufficiently elevated temperatures and subsequent formation of nanostructured material. Spinodal decomposition (900°C) is characteristic for $Ti_{1-x}Al_xN$ and it leads to the formation of nanocomposites

consisting of fcc-TiN and fcc-AlN-enriched coherent phases. [1] In the case of $\text{Cr}_{1-x}\text{Al}_x\text{N}$ precipitation of incoherent hexagonal ZnS-type (wurtzite) w -AlN nanograins occurs within the solid solution at the temperature of about 700°C. [1] The continuing process of decomposition leads to the dual-phase structure containing stable w -AlN and fcc -TiN or fcc -CrN phases, grain coarsening and degradation of mechanical properties. Nowadays, research activity is focused on improvement of thermal stability and oxidation resistance of ternary nitrides via a concept of alloying TMNs with additional elements from group III-VI (Y, Zr, Hf, V, Nb, Ta, Mo, W), where alloying is realized by substitution of TM and Al atoms in the metallic sublattice. [2] Investigations of several authors [3-5] showed that Ta alloying (a pentavalent element) results in a pronounced increase in thermal stability of $\text{Ti}_{1-x-y}\text{Al}_x\text{Ta}_y\text{N}$ by shifting the onset of the nitride phase decomposition by $\sim 200^\circ\text{C}$. Additionally, alloying Ta into $\text{Ti}_{1-x}\text{Al}_x\text{N}$ is also very beneficial for oxidation resistance [3]. Unlike for $\text{Ti}_{1-x}\text{Al}_x\text{N}$, effects of alloying TM elements on the improvement of $\text{Cr}_{1-x}\text{Al}_x\text{N}$ coatings are much less investigated. Rovere [4-6] reported enhanced oxidation resistance of $\text{Cr}_{0.30}\text{Al}_{0.68}\text{Y}_{0.02}\text{N}$ with very small content of yttrium (~ 1 at.%). In this study, we investigate the influence of tantalum content (0÷10.4 at.%) on the phase stability of $\text{Cr}_{1-x-y-z}\text{Al}_x\text{Y}_y\text{Ta}_z\text{N}$ coatings prepared by reactive magnetron co-sputtering with various analysis techniques and supported by *ab initio* calculations.

EXPERIMENTAL DETAILS

Cr-Al-Y-Ta-N coatings were reactively deposited using unbalanced magnetron co-sputtering from powder metallurgically prepared CrAlY target (49.5/49.5/1 at.%, 100 mm dia., 99.5 % purity) and Ta target (100 mm dia., 99.99 % purity) in Ar+N₂ discharge. More details, see Ref. 7. The as-deposited Cr-Al-Y-Ta-N coatings deposited on polished Al₂O₃ plates were annealed in Ar+5%H₂ atmosphere (10⁻¹ Pa) at the temperatures of 900 °C ÷ 1200 °C for 3. Scanning electron microscopy (SEM, Tescan Lyra), energy-dispersive X-ray spectroscopy (EDS) and thermogravimetric analysis (TGA, Netzsch STA 409 CD) were used to analyze thickness, morphology, chemical composition and mass changes of the coatings, respectively. Thermal stability and decomposition route after annealing at temperatures up to 1200°C were examined using X-ray diffraction (XRD, PANalytical X'Pert PRO MRD) and transmission electron microscopy ((S)TEM, JEOL 2100). All *ab initio* calculations based on density functional theory (DFT) were done with the VASP 5.3 code.

RESULTS

The as-deposited $\text{Cr}_{1-x-y-z}\text{Al}_x\text{Y}_y\text{Ta}_z\text{N}$ coatings are stoichiometric with $\text{N}/(\text{Cr}+\text{Al}+\text{Y}+\text{Ta}) = 1$ and compositions of $\text{Cr}_{0.49}\text{Al}_{0.50}\text{Y}_{0.01}\text{N}$, $\text{Cr}_{0.46}\text{Al}_{0.46}\text{Y}_{0.01}\text{Ta}_{0.07}\text{N}$, $\text{Cr}_{0.45}\text{Al}_{0.42}\text{Y}_{0.01}\text{Ta}_{0.12}\text{N}$ and $\text{Cr}_{0.42}\text{Al}_{0.36}\text{Y}_{0.01}\text{Ta}_{0.21}\text{N}$ corresponding to Ta contents of 0 at.%, 3.7 at.%, 5.7 at.% and 10.4 at.%, respectively. Typical SEM cross-sectional images of several micrometers thick $\text{Cr}_{1-x-y-z}\text{Al}_x\text{Y}_y\text{Ta}_z\text{N}$ coatings are displayed in Fig. 1. The as-deposited coatings exhibited the morphology with densely packed columnar grains (Fig. 1a). Changes in the chemical composition after annealing were also reflected in the morphological changes of the coatings when disappearance of columnar grains, formation of a dense featureless structure and reduced thickness due to N_2 loss was observed (Fig. 1b).

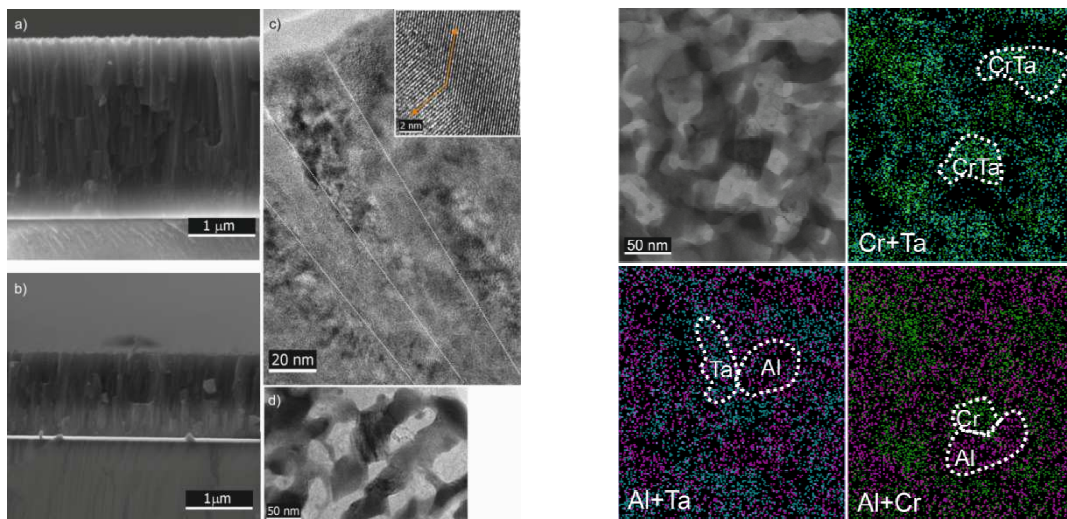


Fig. 1 a), b) Typical SEM cross-sectional micrographs of $\text{Cr}_{1-x-y-z}\text{Al}_x\text{Y}_y\text{Ta}_z\text{N}$ coatings with various Ta content; c) TEM micrograph of as dep. $\text{Cr}_{0.42}\text{Al}_{0.36}\text{Y}_{0.01}\text{Ta}_{0.21}\text{N}$ with inset showing high-angle boundary between two grains; d) BF-TEM micrograph of $\text{Cr}_{0.42}\text{Al}_{0.36}\text{Y}_{0.01}\text{Ta}_{0.21}\text{N}$ annealed at 1200°C in $\text{Ar}+\text{H}_2$ atmosphere; Fig. 2 STEM micrograph of the $\text{Cr}_{0.42}\text{Al}_{0.36}\text{Y}_{0.01}\text{Ta}_{0.21}\text{N}$ coating illustrating the structural evolution after annealing at 1200°C with EDX maps of Al, Cr and Ta.

All prepared $\text{Cr}_{1-x-y-z}\text{Al}_x\text{Y}_y\text{Ta}_z\text{N}$ coatings in the as-deposited state exhibit a single phase cubic structure identified as fcc- $\text{CrAlY}(\text{Ta})\text{N}$ solid solution (Fig. 3a). The structural investigation indicates that tantalum-free $\text{Cr}_{0.49}\text{Al}_{0.50}\text{Y}_{0.01}\text{N}$ coatings start to decompose when the annealing temperature exceeds 900°C and results in the formation of w-AlN precipitates in the remaining Cr-rich matrix. Unstable Cr-N bonds at higher temperatures and N-loss lead to dual-phase structure consisting of w-AlN and bcc-Cr. The presence of Ta in the solid solution shifts the start of the decomposition process to higher temperatures ($>1000^\circ\text{C}$ for

$\text{Cr}_{0.42}\text{Al}_{0.36}\text{Y}_{0.01}\text{Ta}_{0.21}\text{N}$ with Ta content of 10.4 at.%), leading to improvement of thermal stability compared to CrAlYN (Fig. 3b). This improved thermal stability can be attributed to higher cohesive energies of the Ta-containing solid solutions, according to *ab initio* calculations. Decomposition of solid solutions during gradual increase of temperature to 1200°C accompanied by a loss of nitrogen continues with the formation of cubic and hexagonal Cr- and Ta-containing binaries or ternaries. DFT calculations found negative values of mixing free energies for cubic $\text{Cr}_{1-x}\text{Ta}_x\text{N}$ at 1600K indicating its stability over the whole composition range with respect to the cubic binaries. This prediction was confirmed by the STEM investigation, where the presence of CrTa-containing grains after annealing at 1200°C was clearly visible (Fig. 2).

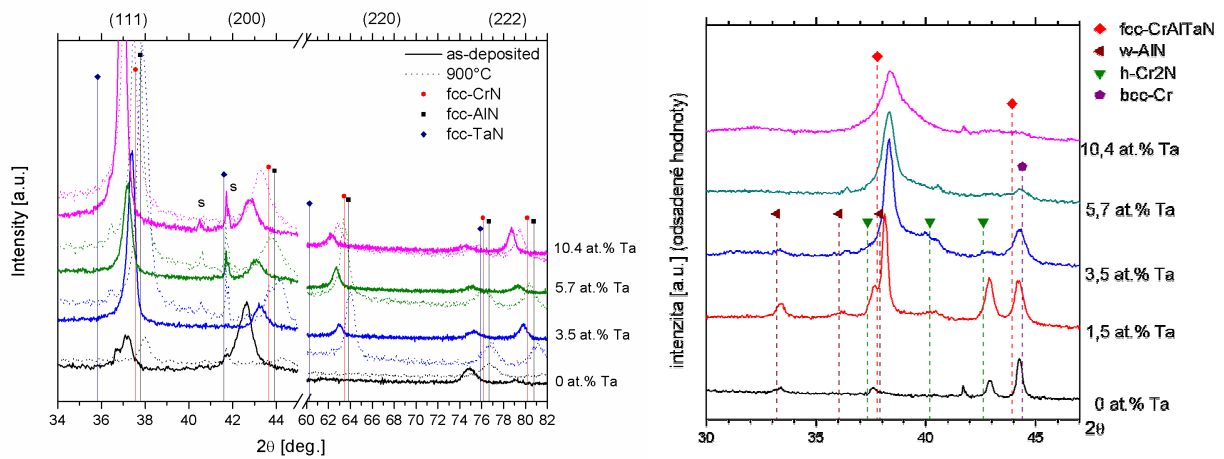


Fig. 3a) The difference in the structure of as-deposited $\text{Cr}_{1-x-y-z}\text{Al}_x\text{Y}_y\text{Ta}_z\text{N}$ coatings with various compositions; b) Comparison of XRD patterns of the coatings with various Ta content annealed at 1000°C in $\text{Ar}+\text{H}_2$ atmosphere.

CONCLUSIONS

$\text{Cr}_{1-x-y-z}\text{Al}_x\text{Y}_y\text{Ta}_z\text{N}$ coatings with various Ta content (0-10.4 at.%) were reactively sputtered and exhibited a single phase cubic (B1) structure identified as metastable fcc-CrAlY(Ta)N solid solution in the as-deposited state. The increase in tantalum content in the structure increases the temperature of decomposition (from $\sim 900^\circ\text{C}$ for Ta free to $>1000^\circ\text{C}$ Ta=10.4 at.%). The result of decomposition is N_2 -depleted nanocrystalline structure containing wurtzite w-AlN, cubic $\text{Cr}_{1-z}\text{Ta}_z\text{N}$ and probably another tantalum and chromium containing phases. This is also in good agreement with the calculated phase stabilities where we found negative mixing free energies values for $\text{Cr}_{1-z}\text{Ta}_z\text{N}$ over the whole composition range.

ACKNOWLEDGEMENTS

This work has been supported by the Ministry of Education of the Slovak Republic and the Slovak Research and Development Agency under the contract numbers APVV-14-0173 and Operational Program Research and Development (projects ITMS:26240220002 and ITMS:26220220004).

REFERENCES

- [1] Mayrhofer, P. H., Rachbauer, F., Holec, D., Rovere, F., Schneider, J. M. Protective Transition Metal Nitride Coatings, *Comprehensive Materials Processing*, Volume 4 355-388, Elsevier, Amsterdam, 2014
- [2] Lind, H., Forsén, R., Alling, B., Ghafoor, N., Tasnádi, F., et al. *Appl. Phys. Lett.* 99, 091903 (2011)
- [3] Hollerweger, R., Riedl, H., Paulitsch, J., Arndt, M., Rachbauer, R., Polcik, P., Primig, S., Mayrhofer, P. H. *Surf. Coat. Technol.* 257 (2014) 78–86
- [4] Rachbauer, R., Holec, D., Mayrhofer, P. H. *Surf. Coat. Technol.* 211 (2012) 98-103.
- [5] Rachbauer, R., Holec, D., Mayrhofer, P. H. *Appl. Phys. Lett.* 97 (2010) 151901.
- [6] Rovere, F., Mayrhofer, P. H. *J. Vac. Sci. Technol. A* A26 (2007) 29-36.
- [7] Mikula, M., Roch, T., Plašienka, D., Satrapinsky, L., Švec sr., P., Vlčková, D., Dvoranová, M., Grančič, B., Gregor, M., Plecenik, A., Kúš, P. *Surf. Coat. Technol.* 259 (2014) 698 – 706

**DEPOZICE TVRDÝCH A PŘESTO TAŽNÝCH MoBC VRSTEV PULZNÍM
STEJNOSMĚRNÝM MAGNETRONOVÝM NAPRAŠOVÁNÍM**

**DEPOSITION OF HARD YET MODERATELY DUCTILE MoBC COATINGS BY
PULSED-DC MAGNETRON SPUTTERING**

P. Souček¹, V. Buršíková¹, L. Zábranský¹, J. Buršík², P. Vašina¹

*¹Ústav fyzikální elektroniky, Přírodovědecká fakulta, Masarykova univerzita, Brno,
Česká Republika*

²Ústav fyziky materiálů, Akademie věd, České Republiky, v.v.i, Brno, Česká Republika

ABSTRACT

Novel nanolaminated MoBC coatings were prepared using a combination of non-reactive direct current and pulsed direct current magnetron sputtering. Depending on the deposition conditions the coatings were either of amorphous or of nanocomposite nature. Nanocomposite coatings showed good hardness and Young's modulus and showed no tendency to form cracks even for high-load nanoindentation testing.

Keywords: magnetron sputtering, protective coatings, nanolaminate, MoBC

INTRODUCTION

Standard ceramic materials nowadays used as protective coatings such as TiN, TiAlN, c-BN, etc., exhibit high hardness and high stiffness. However these are often connected with brittle behaviour of the coating thus limiting the lifetime of the coating and of the coated tool as well. To overcome these limitations, a new generation of materials with high hardness and moderate ductility is sought for.

Recently, nanolaminate Mo₂BC coatings were predicted to have these advantageous properties [1]. However deposition conditions so far necessary to deposit Mo₂BC coatings are a limiting factor. First, deposition process utilizing combinatorial DC magnetron sputtering required substrate temperature of 900°C was reported [1]. Secondly, a low temperature synthesis method reducing the substrate temperature to 380°C required using High Power Impulse Magnetron Sputtering (HiPIMS) with compound Mo₂BC target [2]. Both of these methods pose significant problems with industrial scale production. High deposition

temperatures that are at or above tempering temperature of the tools would worsen the mechanical properties of the coated tools and HiPIMS technology is still not widely used due to its high cost and relatively complicated operation.

EXPERIMENTAL SETUP

Multi-target sputtering system equipped with four targets (B_4C , C and Mo targets were used) aimed at central RF biasable and up to 750 °C heatable substrate holder was employed for all depositions.

First the hardmetal (cemented tungsten carbide) substrates were ultrasonicated in acetone and then in isopropylalcohol. After insertion in the chamber, the samples were cleaned by argon ion bombardment for 20 minutes. Then the deposition itself commenced, B_4C and Mo targets were DC driven, while the C target was connected to a pulsed DC source. Various deposition temperatures were used. Both conditions with and without substrate bias were used.

The crystallinity of the samples was investigated using Rigaku SmartLab diffractometer with Cu $K\alpha$ radiation in grazing angle of incidence geometry. Surface of the samples was imaged using Tescan MIRA3 scanning electron microscope. Thin lamellas were prepared using FIB on Tescan LYRA 3 XMU FEG/SEMxFIB microscope and the resulting lamellas were imaged using JEOL JEM-2100F transmission electron microscope. The mechanical properties of the coatings were evaluated by TI 950 TriboIndenter by Hysitron.

RESULTS AND DISCUSSION

Pulsed DC plasma generation was used in order to increase the localized heating of the sample due to ion bombardment. Thus in order to quantify the ion flux on the growing film a simple planar Langmuir probe in place of the substrate was used to measure the saturated ion current as a function of the pulsing frequency and the duty cycle. The resulting graph is plotted in Fig. 1. It can be seen that the ion bombardment and in turn also the energy influx of the growing film intensifies as the pulsing frequency is increased and the duty cycle is decreased. Thus pulsing frequency of 350 kHz and duty cycle of 65 % were chosen for coating deposition.

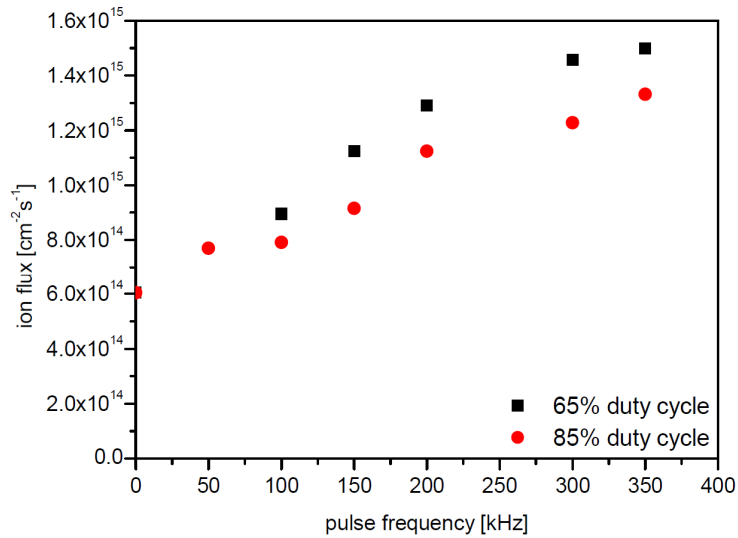


Fig. 1: Ion flux on the growing film as a function of pulsing frequency and duty cycle

Coatings with (-200 V) and without bias were prepared with C target pulsed at 350 kHz with at different substrate temperatures and the resulting diffractograms presented in Fig. 2. The reference is taken from [2] and position of the peaks corresponding to amorphous (A) and crystalline (C) Mo_2BC phase are marked.

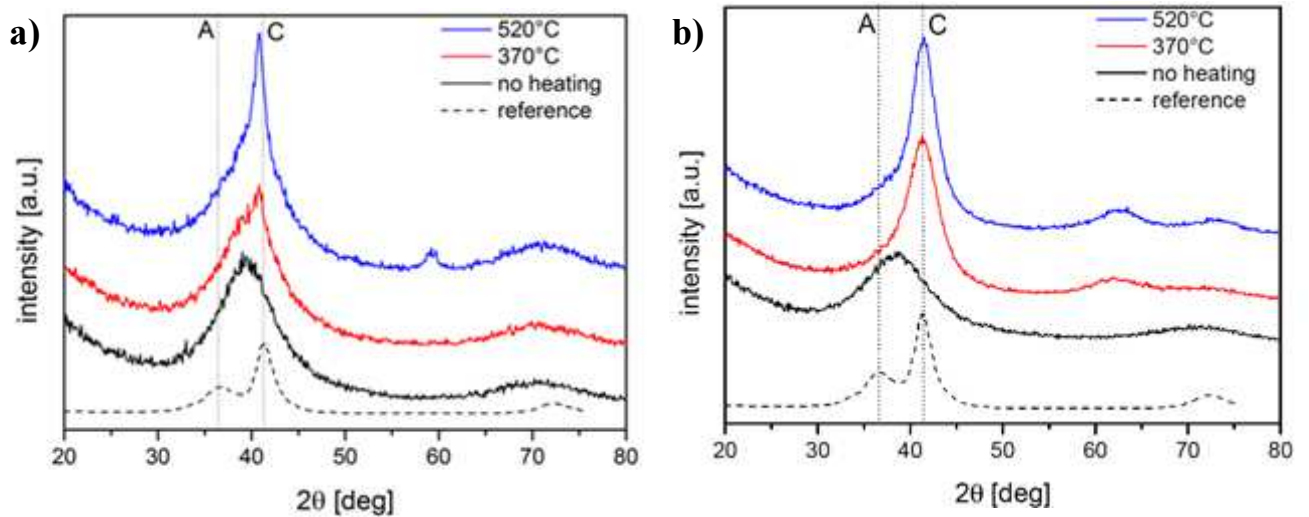


Fig. 1: XRD diffractograms of samples prepared a) with -200 V bias and b) no bias, reference taken from [2]

Both samples prepared without external heating were amorphous as was proved by TEM and selected area diffraction pattern measurements. Samples prepared at elevated temperatures

were of nanocomposite nature with crystalline Mo₂BC phase and another amorphous phase as well.

The hardness and Young's modulus were measured using nanoindentation. The nanocomposite samples show typical hardness of about 30 GPa with elastic modulus about 335 GPa, while the amorphous the average hardness of the amorphous samples is about 19.5 GPa with elastic modulus about 275 GPa. No pop-in events in load-displacement curves and no sudden drops in differential hardness even with cube corner indents were detected, this together with residual indent SEM imaging indicate no cracking inside.

CONCLUSIONS

Nanocomposite Mo-B-C coatings were prepared at lowered temperature utilizing mid-frequency pulsed DC magnetron sputtering. Coatings exhibit low roughness, good adhesion to metallic substrates, high hardness and no cracks were observed even at high load indentation tests.

ACKNOWLEDGMENT

This research has been supported by the project CZ.1.05/2.1.00/03.0086 funded by European Regional Development Fund, project LO1411 (NPU I) funded by Ministry of Education, Youth and Sports of Czech Republic and GACR project 15-17875S.

REFERENCES

- [1] Emmerlich, J., Music, D., Braun, M., Fayek, P., Munnik, F., Schneider, J. M. J. Phys. D: Appl. Phys., 2009 42 185406 (6pp).
- [2] Bolvardi, H., Emmerlich, J., Mráz, S., Amdt, M., Rudigier, H., Schneider, J. M. Thin Solid Films, 2013 542 5-7

Ti-B-Si-N POVLAKY SO ZVÝŠENOU TEPLOTNOU STABILITOU PRIPRAVENÉ POMOCOU MAGNETRÓNOVÉHO NAPRAŠOVANIA

Ti-B-Si-N COATINGS WITH ENHANCED THERMAL STABILITY PREPARED BY MAGNETRON SPUTTERING

M. Pleva^{1*}, B. Grančič¹, M. Mikula^{1,2}, M. Truchlý¹, T. Roch¹, L. Satrapinsky¹, M. Gregor¹,
P. Ďurina¹, V. Girman³, A. Plecenik¹ a P. Kúš¹

¹*Katedra experimentálnej fyziky, Fakulta matematiky, fyziky a informatiky, Univerzita
Komenského, 842 48 Bratislava, Slovensko*

²*Ústav materiálov a mechaniky strojov, Slovenská akadémia vied, 831 02 Bratislava,
Slovensko*

³*Ústav fyzikálnych vied, Prírodovedecká fakulta, Univerzita P. J. Šafárika, 041 54 Košice,
Slovensko*

ABSTRACT

Ti_{0.25}B_{0.75-x}Si_xN (0 ≤ x ≤ 0.25) coatings are deposited on sapphire substrates in reactive Ar+N₂ atmosphere using magnetron sputtering from TiB₂ and Si targets. According to the XRD and HR-TEM analyses the as-deposited coatings are amorphous. Post-deposition vacuum annealing is performed at temperatures up to 1100 °C to observe the thermal stability of coatings. Chemical analysis by EDS and XPS reveals that the composition of the coatings as well as the bonding structure is stable up to 1100 °C. Regardless of the annealing temperature, only B-N, Si-N and Ti-N bonding is visible on the XPS narrow ranges spectra. During annealing a nanocrystalline *fcc*-TiN phase (grain size of 2-4 nm) in an amorphous *a*-(Ti)BSiN matrix is formed. Whereby the increased Si content inhibits the crystal growth in the coating and increases the hardness (from 10 to 14 GPa). Even after annealing up to 1100 °C the amorphous phase continues to build dominant part of the coating volume. Consequently almost no change in hardness is visible after exposure to increased temperatures.

Keywords: Ti-B-Si-N, amorphous coatings, thermal stability, magnetron sputtering,

INTRODUCTION

Transmission metal (TM) nitrides i.e. TiN, CrN, TiAlN, CrAlN are widely used materials for protection coatings due to their excellent mechanical properties [1]. For this type of coatings columnar structure with nitride phases or solid solution is typical [2]. Critical places of crystalline coatings are grain boundaries, through them oxygen from atmosphere penetrates into material, which causes the oxidation of coating and degradation of mechanical properties. Adding elements such as boron and silicon into materials can slow down or even

prevent crystal growth. Nanocomposite coatings with hard nanograins enveloped with amorphous matrix (or amorphous coatings) are created and the penetration of oxygen through grain boundaries is inhibited. Most important attribute of this type of hard coatings is the thermal stability, coatings have to keep nanocomposite or amorphous character up to high temperatures. Nowadays this category of hard coatings is composed from nanocomposite coatings containing nanocrystalline and amorphous phase such as *nc*-TiN/*a*-Si₃N₄ [3] a *nc*-TiN/*a*-BN [1] and amorphous coatings, i.e. Si-Cr-N [4] and Ti-B-Si-N [5]. This work is focused on study of influence of increasing temperature on structure and mechanical properties on Ti-B-Si-N coatings with varied content of Si and B.

EXPERIMENTAL DETAILS AND RESULTS

Ti-B-Si-N coatings were deposited by unbalanced magnetron co-sputtering from TiB₂ (DC; 100 mm dia; 99.5% pur.; $U=500V$; $I=1.5A$) and Si (RF; 100 mm dia; 99% pur.; $P=250W$) targets on *c*-cut sapphire substrates in reactive Ar+N₂ atmosphere (pressure ratio Ar/N₂~0.7/0.3; total pressure $p=0.33Pa$) for 4 hours. The substrates were hold in three different positions relatively to targets what defined the Si content in the coating. Ti-B-N coating was deposited keeping same conditions, only the RF power on Si target was switched off and substrates were hold on position B. Post-deposition annealing at temperatures 700°C, 800°C, 1000°C, 1100°C and 1200°C of samples was performed in vacuum chamber in the Ar atmosphere for 10 min with heating speed 60°C/min.

Chemical composition of as deposited coatings shows increasing silicon content versus decreasing boron content in samples named A, B and C (table 1.). Nitrogen and titanium ratio remains almost the same in all samples and is independent on the deposition position. During the annealing almost no change in chemical composition is visible up to 1100°C (Evolution of B – Ti_{0.25}B_{0.61}Si_{0.14}N is shown on fig. 1). XPS analyses of sample B - Ti_{0.25}B_{0.61}Si_{0.14}N (as dep., annealed at 1000°C, 1200°C) confirmed the chemical composition of sample B. Detailed study of XPS core spectra indicated that every element is bonded to nitrogen Ti-N, Si-N, B-N.

The as-deposited coatings appear are X-ray amorphous. After annealing a gradual increase of *fcc*-TiN phase is visible (Fig. 3a). Typical crystalline grain size is 2-4 nm where smaller sizes belong to increased Si concentration. Comparison of XRD spectra of Ti-B-Si-N coatings annealed at 800°C and 1100°C is displayed on Fig. 3b.

Table 1. Chemical composition of Ti-B-Si-N coatings revealed by EDS

Sample	Ti (at. %)	B (at. %)	Si (at. %)	N (at. %)	O (at. %)
Ti _{0.30} B _{0.70} N	13	31.2	-	52.8	3
A - Ti _{0.25} B _{0.68} Si _{0.07} N	11.7	32.1	3.2	49.6	3.2
B - Ti _{0.25} B _{0.61} Si _{0.14} N	11.8	28.5	6.4	49.6	3.6
C - Ti _{0.26} B _{0.48} Si _{0.25} N	12	22.2	11.7	49.6	4.5

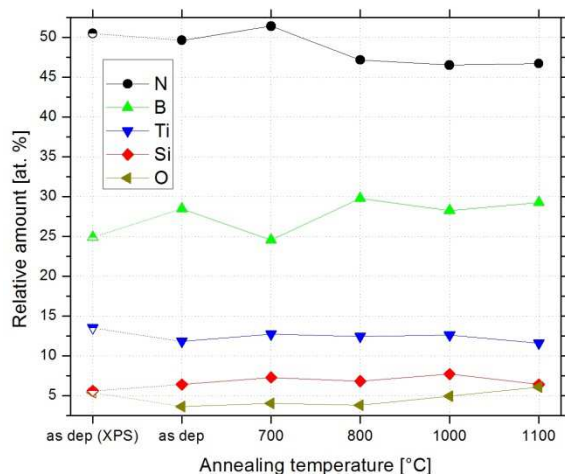


Fig. 1. Chemical composition of annealed sample B - Ti_{0.25}B_{0.61}Si_{0.14}N revealed by

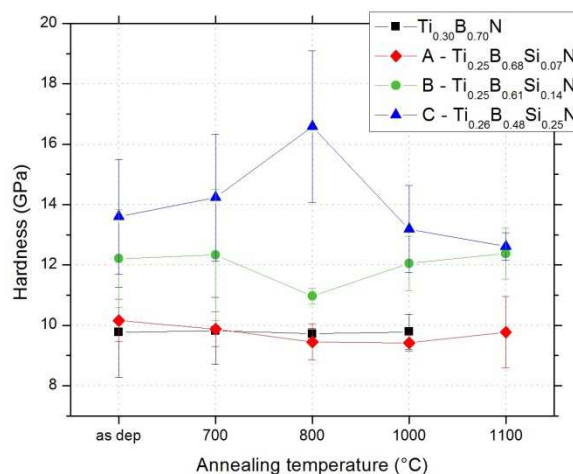


Fig. 2. Hardness evaluation of Ti-B-Si-N coatings during the annealing in vacuum.

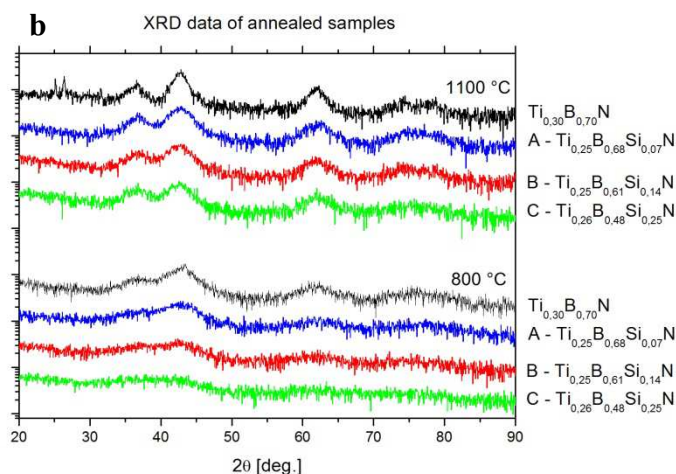
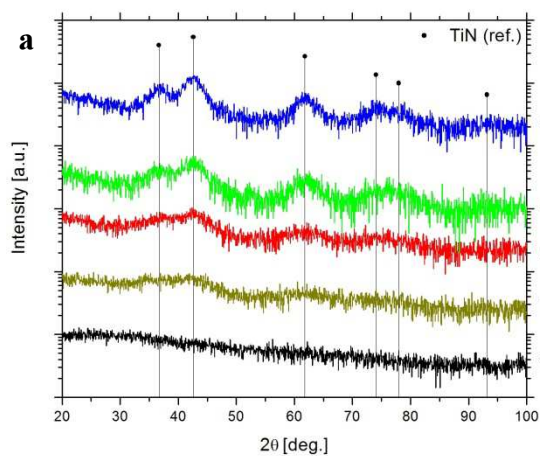


Fig. 3. a. Diffraction spectra of sample B - Ti_{0.25}B_{0.61}Si_{0.14}N annealed at different temperatures. b. Comparison of diffraction spectra of samples annealed at 800 °C and 1100 °C.

HRTEM images show amorphous phase in as deposited sample B - Ti_{0.25}B_{0.61}Si_{0.14}N. During the annealing a growth of *fcc*-TiN crystals covered with amorphous phase is visible same as in XRD spectra. After annealing small (2-4 nm) crystalline nanograins embedded in relatively thick amorphous matrix are found on the HR-TEM images. Electron diffraction analysis of as-deposited sample confirms amorphous character of coating and analysis of

annealed samples shows nanostructured character. The diffraction circles correspond to *fcc*-TiN phase.

Nanoindentation measurements show increasing hardness with increasing Si content in as-deposited coatings. Hardness evolution is not visible during the annealing up to 1100°C (Fig. 2). Age hardening effect is not visible, because the high volume fraction of amorphous *a*-(Ti)BSiN matrix has dominant effect on mechanical properties.

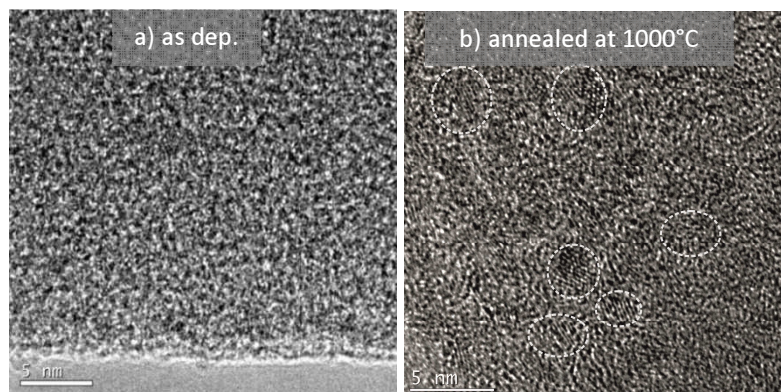


Fig. 6. On HR-TEM images of sample B – $\text{Ti}_{0.25}\text{B}_{0.61}\text{Si}_{0.14}\text{N}$ are observed:

- a) only amorphous phase in as deposited sample; b) low concentration of 2-3 nm nanograins embedded in amorphous matrix in sample annealed at 1000°C.

CONCLUSIONS

Amorphous $\text{Ti}_{0.25}\text{B}_{0.75-x}\text{Si}_x\text{N}$, $0 \leq x \leq 0.25$ coatings were deposited by reactive magnetron sputtering from TiB_2 and Si targets. Ti-N, Si-N and B-N bonds were observed by XPS. XRD and TEM investigation revealed that annealing of the coatings up to 1100°C leads to the formation of *fcc*-TiN phase with grain size of 2-4 nm embedded in a relatively thick amorphous *a*-(Ti)BSiN matrix. Coatings with increased Si content showed enhanced hardness, on the other side the Si addition suppresses the nanocrystalline phase formation at elevated temperature. The hardness remains almost constant after annealing up to the 1100°C. This corresponds to the fact that even after annealing, the coatings contain considerable amount of amorphous phase.

ACKNOWLEDGEMENT

Authors would like to thank for financial support in projects from OP Research and Development (ITMS: 26240220002 a ITMS: 2622022004), Slovak research and development agency (APVV-14-0173) and Comenius University (Grant UK/434/2015).

REFERENCES

- [1] Musil, J., Hard nanocomposite coatings: Thermal stability, oxidation resistance and toughness, *Surface & Coating Technology*, 207 (2012) 50-65.
- [2] Mayrhofer, P. H., Mitterer, C., Hultman, L., Clemens, H., Microstructural design of hard coatings, *Progress in Materials Science*, 51 (2006) 1032-1114.
- [3] Vepřek, S., Vepřek-Heijman, M. G. J., Karvankova, P., Prochazka, J., Different approaches to superhard coatings and nanocomposites, *Thin Solid Films*, 476 (2005) 1-19.
- [4] Mikula, M., Grančič, B., Drienovský, M., Satrapinskyy, L., Roch, T., Hájovská, Z., Gregor, M., Plecenik, T., Čička, R., Plecenik, A., Kúš, P., Thermal stability and high-temperature oxidation behavior of Si–Cr–N coatings with high content of silicon, *Surface & Coatings Technology*, 232 (2013) 349-356.
- [5] Fager, H., Greczynski, G., Jensen, J., Lu, J., Hultman, L., Growth and properties of amorphous Ti–B–Si–N thin films deposited by hybrid HIPIMS/DC-magnetron co-sputtering from TiB₂ and Si targets, *Surface & Coatings Technology*, 259, 442-447 (2014)

ELEKTRICKY VODIVÉ KOMPOZITY NA BÁZE SiC

ELECTRICALLY CONDUCTIVE COMPOSITES BASED ON SiC

R. Bystrický, J. Sedláček, P. Šajgalík

Ústav anorganickej chémie, Slovenská akadémia vied, Dúbravská cesta 9, 845 36 Bratislava

ABSTRACT

Mechanical, electrical and thermal properties of SiC ceramics with various content of Ti-NbC phase were characterized. Samples were prepared by hot-pressing method at 1980 °C for 1.5 h in Ar atmosphere under mechanical pressure of 30 MPa. The increasing content of Ti-NbC phase leads to the increase of hardness and indentation toughness. The highest value of hardness and toughness (21.13 GPa, 7.59 MPa·m^{1/2}) was obtained for the sample SiC50TiNbC. The presence of Ti-Nb-C phase significantly has increased the electrical conductivity of SiC composites. The highest electrical conductivity was in sample with 40 mass% addition of Ti-NbC phase. The addition of Ti-NbC phase leads to decreasing thermal properties of SiC ceramics.

Keywords: silicon carbide, electrical conductivity, hot-pressing

INTRODUCTION

Silicon carbide (SiC) is one of the most promising structural materials because of the unique combination of its good mechanical properties at room and high temperatures, high thermal conductivity, good chemical inertness, and excellent wear and corrosion resistances [1-5]. Thus, SiC ceramics are used in many industrial applications such as fusion reactor parts, turbine components, hot-gas filters, optical mirrors, structural parts, diesel particulate filters, and components for semiconductor processing equipment [6-9].

In spite of SiC ceramics are known as very difficult to machine materials [10]. One way to machine the SiC ceramics is grinding with diamond. However, there are some limitations when complex shapes have to be produced. Using electric discharge machining method may be the possible solution of this problem. On the other hand, the method can be used only for materials with sufficiently high electrical conductivity (more than 10⁻³ S·mm⁻¹). Increasing of the electrical conductivity of materials can be achieved by addition of an doping agent for example, Ti-NbC [11], C-TiCN [12], graphene [13], MoSi₂ [14].

In this work, we focused on adding a Ti-NbC as secondary phase to SiC matrix. The various amounts of Ti-NbC were added and their influence on the mechanical and electrical properties of final composite was investigated.

EXPERIMENTAL PART

The commercially available powders of β -SiC (HSC-059, Superior Graphite, USA), Ti (TOHO Titanium Co., Japan) and NbC (Japan New Metals Co., Japan) were used for the starting mixtures preparation. The SiC-based composites were prepared by the addition of the various amount of electrically conductive Ti-NbC phase what is a mixture of Ti and NbC in a molar ratio 1:1.8. The chemical composition of starting mixtures are briefly listed in Table 1.

Tab. 1. Chemical composition of starting mixtures

Sample	w[mass%]		
	SiC	Ti	NbC
SiC50TiNbC	50	18	32
SiC40TiNbC	60	14.4	25.6
SiC30TiNbC	70	10.8	18

The powder mixtures were planetary milled in water with WC balls at 150 rpm for 1 h. The homogenized suspensions were freeze dried. The pre-pressed pellets were hot pressed at 1980 °C for 1.5 h in Ar atmosphere under 30 MPa pressure.

RESULTS

This work is focused on the addition of Ti-NbC to SiC matrix and investigated the influence of the doping agent on the mechanical and electrical properties of final composite (hardness, indentation toughness, electrical conductivity and thermal diffusivity).

Table 2 shows the density, mechanical and electrical properties of sintered samples. The hardness of the samples SiC40TiNbC and SiC30TiNbC have been 18.81 GPa and 18.73 GPa, respectively. On the other hand, the hardness of the SiC50TiNbC sample has reached the value of 21.16 GPa what it is more than the reference sample made by Frajkorova et al. [11] have (20.6 GPa).

Moreover, indentation toughness of the sample SiC50TiNbC ($7.59 \text{ MPa} \cdot \text{m}^{1/2}$) was higher than of the sample SiC40TiNbC ($7.26 \text{ MPa} \cdot \text{m}^{1/2}$) and SiC30TiNbC ($7.48 \text{ MPa} \cdot \text{m}^{1/2}$). All of these

samples have had higher toughness than reference sample ($5.4 \text{ MPa}\cdot\text{m}^{1/2}$) [11] and samples with the same composition made by Frajkorova et al. [15]. The differences can be explained by higher sintering temperature when in our case higher densities of materials were achieved. Also, the prepared materials have had the better electrical conductivity than the reference samples. The highest electrical conductivity was observed for the sample SiC40TiNbC ($75.63 \text{ S}\cdot\text{mm}^{-1}$). All of the samples have values higher than reference sample of SiC ($1,4 \text{ S}\cdot\text{mm}^{-1}$) [11].

Tab. 2 Mass changes, densities and mechanical properties of samples after sintering at $1980 \text{ }^\circ\text{C}$

Sample	$\rho [\text{g}\cdot\text{cm}^{-3}]$	$HV [\text{GPa}]$	$K_{IC}[\text{MPa}\cdot\text{m}^{1/2}]$	$\sigma [\text{S}\cdot\text{mm}^{-1}]$
SiC50TiNbC	4.23	21.16 ± 0.49	7.59 ± 0.76	46.18
SiC40TiNbC	4.00	18.81 ± 0.73	7.26 ± 0.39	75.63
SiC30TiNbC	4.32	18.73 ± 0.19	7.48 ± 0.42	63.04

The dependence of the composite thermal diffusivity on the heat treatment is shown in the figure 1. Addition of Ti-NbC phase causes decreasing of thermal diffusivity of the samples. Only sample SiC40TiNbC at $400 \text{ }^\circ\text{C}$ have higher value than reference sample.

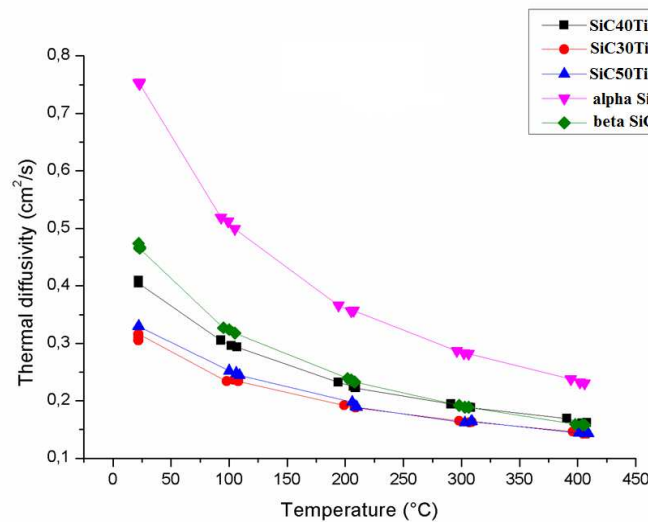


Fig. 1. Thermal diffusivity of composite and reference sample after heat treatment

CONCLUSIONS

Fully dense electrically conductive SiC composites were prepared by using NbC and Ti as sintering additives. Samples with 30, 40, 50 mass% of NbC and Ti were sintered at 1980 °C for 1.5 h.

The increasing content of Ti-NbC phase led to the increase of hardness and indentation toughness. The presence of Ti-NbC phase significantly increased the electrical conductivity of SiC composites. The highest electrical conductivity was in the sample with 40 mass% addition of Ti-Nb-C phase. The addition of Ti-NbC phase led to the decrease of thermal properties of SiC ceramics.

SiC composites with electrically conductive Ti-NbC phase are promising materials for electric discharge machining. Additionally, mechanical properties have been improved in comparison to monolithic SiC.

ACKNOWLEDGEMENT

This work was supported by the Slovak Grant Agency APVV-0108-12.

LITERATURE

- [1] Baxter, D., Bellosi, A., Monteverde, F. Oxidation and burner rig corrosion of liquid phase sintered SiC, *J. Eur. Ceram. Soc.*, 20 (2000), 367–382
- [2] Magnani, G., L. Minocari, G. L., Pilotti, L. Flexural strength and toughness of liquid phase sintered silicon carbide, *Ceram. Int.*, 26 (2000), 495–500
- [3] Sciti, D., Bellosi, A. Effects of additives on densification, microstructure and properties of liquid-phase sintered silicon carbide, *J. Mater. Sci.*, 35 (2000), 3849–3855
- [4] Rixecker, G., Wiedmann, I., Rosinus, A., Aldinger, F. High-temperature effect in the fracture mechanical behavior of silicon carbide liquid-phase sintered with AlN–Y₂O₃ additives, *J. Eur. Ceram. Soc.*, 21 (2001), 1013–1019
- [5] Strecker, K., Hoffmann, M. J. Effect of AlN-content on the microstructure and fracture toughness of hot-pressed and heat-treated LPS-SiC ceramics, *J. Eur. Ceram. Soc.*, 25 (2005), 801–807
- [6] Jenny, J. R., Malta, D. P., Muller, S. G., Powell, A. R., Tsvetkov, V.F., Hobgood, H.M., Galss, R.C., Carter Jr, C.H. High-purity semi-insulating 4H-SiC for microwave device applications, *J. Electron. Mater.*, 32 (2003), 432–436
- [7] Hayun, S., Paris, V., Mitrani, R., Kalabukhov, S., Dariel, M.P., Zaretsky, E., Frage, N.

- Microstructure and mechanical properties of silicon carbide processed by Spark Plasma Sintering (SPS), *Ceram. Int.*, 38 (2012), 6335–6340
- [8] Borrero-Lopez, O., Ortiz, A.L., Ciudad, E., Rodriguez-Rojas, F., Guiberteau, F. Microstructural evolution and contact-mechanical properties of SiC ceramics prepared colloiddally with low additive content, *Ceram. Int.*, 38 (2012), 5979–5986
- [9] Hermann, M., Standke, G., Hohn, S., Himpel, G., Gestrich, T. High-temperature corrosion of silicon carbide ceramics by coal ashes, *Ceram. Int.*, 40 (2014), 1471–1479
- [10] Luis, C. J., Puertas, I., Villa, G. Material removal rate and electrode wear study on the EDM of silicon carbide. *J. Mater. Process. Technol.*, 164/164 (2005), 889–896.
- [11] Frajkorová, F., Hnatko, M., Lenčėš, Z., Šajgalík, P. Electrically conductive silicon carbide with the addition of Ti-NbC, *J. Eur. Ceram. Soc.*, 32, (2012), 2513-2518
- [12] Unno, H., Sugawara, J., Mukai, T. Ellectrically conductive mechanism for Al₂O₃-C-TiCN, *Ceram. Trans.*, 179 (2006), 195-206
- [13] Román-Manso, B., Domingues, E., Figueiredo, F. M., Belmonte, m., Miranzo, P. Enahnced electrical conductivity of silicon carbide ceramics by addition of graphene nanoplatelets, *J. Eur. Ceram. Soc.*, 35 (2015), 2723-2731
- [14] Raju, G. B., Basu, B., Suri, A. K. Thermal and electrical properties of TiB₂-MoSi₂, *Int. J Refr. Met & Hard Mat.*, 28 (2010), 174-179
- [15] Frajkorová, F., Lenčėš, Z., Šajgalík, P. Electrically conductive silicon carbide without oxide sintering additives, 49(2012), 342-346

MIKROŠTRUKTÚRA A MECHANICKÉ VLASTNOSTI ELEKTRICKY VODIVÝCH KOVO-KERAMICKÝCH KOMPOZITOV NA BÁZE SiC.

MICROSTRUCTURE AND MECHANICAL PROPERTIES OF ELECTRICALLY CONDUCTIVE SiC BASED CERMETS.

M. Fides^{1,2}, A. Kovalčíková¹, P. Hvizdoš¹, R. Sedlák^{1,2}, R. Bystrický³, J. Sedláček³

¹*Slovak Academy of Sciences, Institute of Materials Research, Watsonova 47, Košice,
Slovakia*

²*Technical University of Košice, Faculty of Metallurgy, Letná 9, Košice, Slovakia*

³*Slovak Academy of Sciences, Institute of Inorganic Chemistry, Dúbravská cesta 9,
Bratislava, Slovakia*

ABSTRACT

A range of complex composites based on SiC matrix with 30, 40 and 50 wt. % of additives were prepared. The microstructure and chemical composition were studied by SEM equipped with EDX analyzer. Hardness and fracture toughness of prepared materials were evaluated by means of Vickers indentation. Propagation of indentation cracks was analyzed using light microscopy and SEM. Additionally, the electric conductivity as function of fraction of additives was determined.

Keywords: silicon carbide, cermet, indentation, hardness, crack propagation

INTRODUCTION

Silicon carbide (SiC) is one of the most studied synthetic materials of the last century due to its excellent oxidation resistance, high mechanical strength, high hardness, and high thermal shock resistance. Because of these properties it is hard to machine. To enable electric discharge machining (EDM) [1], electro conductive phases (TiNbC) have been added to SiC ceramics. EDM process made machining of extremely hard materials and/or their shaping with high precision possible. The aim of this work is to evaluate microstructure and mechanical properties of such a like prepared SiC – TiNbC cermets.

EXPERIMENTAL MATERIALS AND METHODS

Three types of silicon carbide based cermets with different amount of electrically conductive TiNbC phase (Ti and NbC with ratio of 9:16) were studied. Prepared materials containing TiNbC additives of 30, 40, and 50 wt% were sintered at 1980 °C in air atmosphere and pressed under the pressure of 30 MPa.

The microstructure, porosity and chemical composition were observed by SEM and EDX (ZEISS AURIGA Compact).

Hardness of the materials as a whole was evaluated by means of Vickers indentation (Eq. (1)) with the load of 9.8 N. Fracture toughness was determined by the Anstis method [2] (Eq. (2)) from the lengths of radial cracks and indent diagonals made at load 98 N.

$$HV = \frac{1.8544 \cdot P}{d^2} \quad (1)$$

$$K_{IC} = 0.016 \cdot \left(\frac{E}{H} \right)^{\frac{1}{2}} \cdot \left(\frac{P}{c^{\frac{3}{2}}} \right) \quad (2)$$

Electrical conductivity through surface was measured by four point probes at room temperature 23.3 °C, air humidity 66.9 %.

RESULTS AND DISCUSSION

Resulting materials were relatively hard. With increasing volume fraction of the conductive additives hardness increased from HV1 = 20.10 ± 1.4 GPa for 30 % of TiNbC up to HV1 = 27.39 ± 1.94 GPa for 50 % of TiNbC. This is in a good agreement with the trend found in [1].

Similarly, fracture toughness improved, from 2.52 ± 0.67 MPa.m^{1/2} for 30 % additives of TiNbC up to 3.21 ± 0.53 MPa.m^{1/2} for 50 % of TiNbC. These values are slightly lower than those reported in [1] for lower amounts of TiNbC.

Both trends, for hardness and fracture toughness, are shown on the plots in Fig. 1.

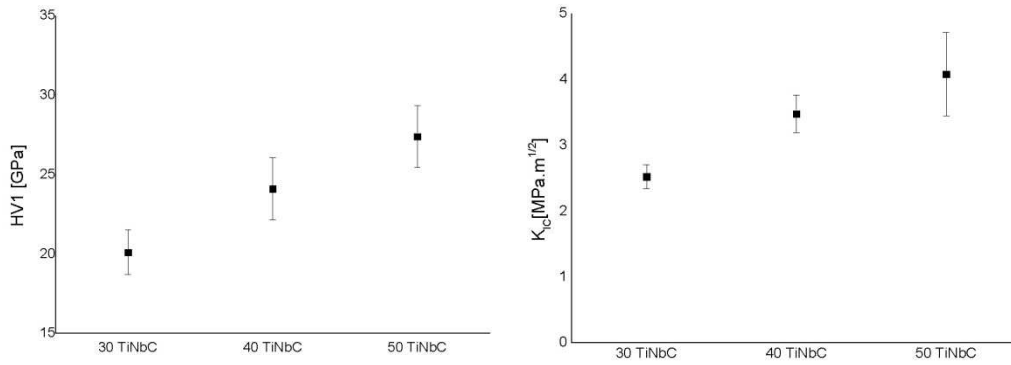


Fig. 1. Hardness (HV1) and fracture toughness (K_{IC}) in SiC - TiNbC cermets

Indentation cracks displayed below propagated mostly intergranularly, though partially also transgranularly through the grains in both of the main phases (SiC and TiNbC) as it is indicated in Fig. 2. The crack paths in TiNbC are frequently deflected and occasionally branched, suggesting the potential of toughening mechanisms in this phase.

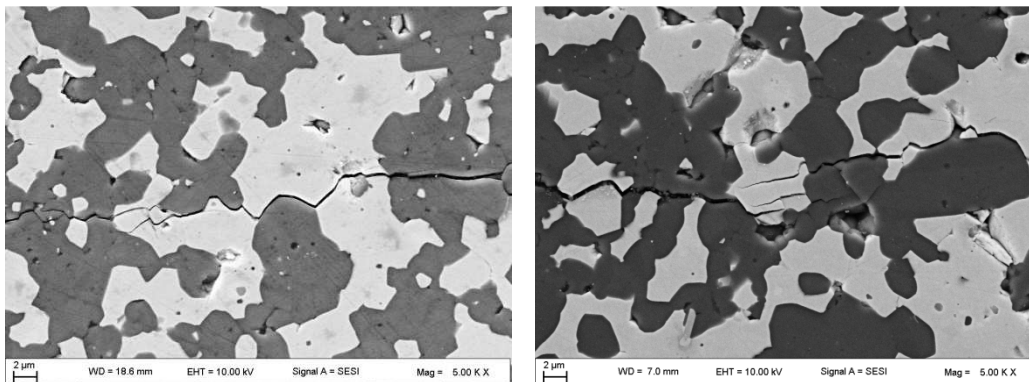


Fig. 2. Propagation paths of the indentation cracks through the individual grains in SiC with 30 wt% addition of TiNbC.

Under the normal conditions silicon carbide is a semiconductor with electrical conductivity approximately 10 Sm^{-1} [3]. TiNbC phase increased the electrical conductivity of presented samples in all cases by about four orders of magnitude (e.g. $8.7 \cdot 10^4 \pm 0.3 \cdot 10^4 \text{ Sm}^{-1}$ for 30 % TiNbC). The results obtained from the measurements of conductivity are shown in Fig. 3. It can be observed that the volume fraction of TiNbC was above the necessary percolation threshold in all cases and thus the resulting conductivity of the composites with additives above 30 % had basically a constant value, regardless of amount of the conducting additive. The measured conductivity is approximately three times lower than that of pure metallic titan ($2.381 \cdot 10^6 \text{ Sm}^{-1}$).

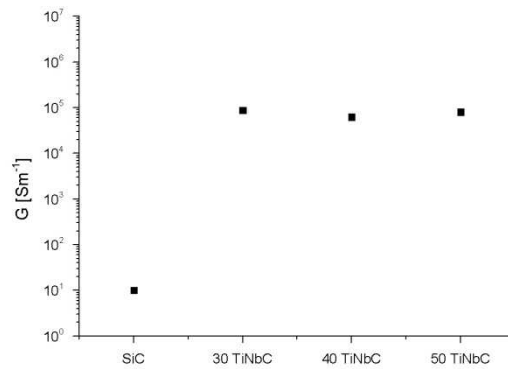


Fig. 3. Electric conductivity of SiC and SiC with different additives of TiNbC.

CONCLUSIONS

Measured hardness increased with increasing amount of additives from 20.10 ± 1.4 GPa for 30 % additives of TiNbC up to 27.39 ± 1.94 GPa for 50 % additives of TiNbC. Furthermore, measured fracture toughness also slightly increased, from 2.52 ± 0.67 MPa.m^{1/2} for 30 % additives of TiNbC up to 3.21 ± 0.53 MPa.m^{1/2} for 50 % additives of TiNbC. Indentation cracks propagated intergranularly and partially transgranularly through the grains in both of the phases SiC and TiNbC. Electric conductivity of basic SiC material is typically around the values of 10 Sm^{-1} . The prepared composite samples in all cases had the conductivity approximately four orders higher due to the presence of TiNbC phase. The conductivity of the composites was basically the same for all amounts of additives, its average value was $7.6 \cdot 10^4 \pm 0.4 \cdot 10^4 \text{ Sm}^{-1}$.

ACKNOWLEDGEMENT

This work was financially supported by the projects: VEGA 2/0075/13 and APVV-0108-12.

REFERENCES

- [1] Frajkorová, F. , Hnatko, M. , Lenčoš, Z. , Šajgalík, P. Electrically conductive silicon carbide with the addition of TiNbC, *J. Eur. Ceram. Soc.*, vol. 32 (2012) 2513–2518.
- [2] Anstis, G. , Chantikul, P. , Lawn, B. , Marshall, D. A critical evaluation of indentation techniques for measuring fracture toughness: I Direct crack measurements, *J. Am. Ceram. Soc.*, vol. 46 (1981) 533–538.
- [3] Kobayashi, R. , Tatami, J. , Wakihara, T. , Meguro T. , Komeya K. Temperature Dependence of the Electrical Properties and Seebeck Coefficient of AlN-SiC Ceramics, *J. Am. Ceram. Soc.*, vol. 89 (2006) 1295–1299.

PRÍPRAVA A CHARAKTERIZÁCIA KOMPOZITOV Si_3N_4 S PRÍDAVKOM GRAFÉNU

PREPARATION AND CHARACTERIZATION OF SILICON NITRIDE - GRAPHENE COMPOSITES

O. Hanzel¹, M. Tatarková², J. Sedláček¹, P. Šajgalík¹

¹*Slovak Academy of Sciences, Institute of Inorganic Chemistry, Dúbravská cesta 9, 845 36
Bratislava, Slovakia*

²*Slovak Academy of Sciences, Institute of Materials Research, Watsonova 47 - 040 01 Košice,
Slovakia*

ABSTRAKT

Silicon nitride-graphene composites were prepared by different ways and from different forms of graphene. In this work we used commercially available graphene nanoplatelets (GNPs) functionalised by carboxyl and amine groups and also we successfully synthesized graphene oxide (GO). In order to reach delamination of graphene layers and homogeneous distribution of graphene layers in composite powders we use strong ultrasound agitation, centrifugation, planetary ball milling and freeze granulation. Composite powders prepared by these ways and from different graphene forms were sintered by hot press at 1650°C and 1700°C for 1 hour and load 30 MPa under overpressure of nitrogen. Hardness and indentation fracture toughness were measured on prepared composites. Thermal diffusivity of composites were measured at room temperature by laser flash technique.

Keywords: graphene nanoplatelets, graphene oxide, thermal diffusivity, silicon nitride

INTRODUCTION

Graphene was discovered by Geim and Novoselov in 2004 [1]. Graphene is an allotropic form of carbon and basically it is a monolayer of graphite. As a result of its unique two dimensional crystal structure and ultra-strong sp^2 carbon bonding network graphene offers extraordinary mechanical, electrical, thermal and optical properties and also very high specific surface area [2]. Therefore incorporation of graphene in to ceramic matrix could improve mechanical and functional properties of ceramic-graphene composites. There are two forms of graphene which are used in composites: graphene nanoplatelets which are generally composed from three and more layers of graphene and graphene oxide which is oxidized form of graphene

monolayer. In this work we study influence of graphene form on microstructure, mechanical properties and thermal diffusivity of silicon nitride-graphene composites.

EXPERIMENTAL

For preparation composite powders with GNPs we used procedure which consist of several steps. First we dispersed and delaminated GNPs in isopropanol using strong ultrasound agitation for 100 minutes. Then we separated single or bilayer graphene from a few layer graphene by centrifugation at 6000 rpm for 15 min. We repeated this process five times, collected suspension with fine fraction of GNPs and added silicon nitride and sintering additives (magnesium oxide and cerium oxide). This mixture was planetary ball milled at 450 rpm for 6 hour. After this isopropanol was evaporated in rotary evaporator. Composite powders was dried and sieved through a microscreen. The same way we used for preparation composite powders with GNPs functionalized with carboxyl and amine groups.

Sedimented fraction was again ultrasonicated and silicon nitride with sintering additives were added. This mixture was planetary ball milled at 450 rpm for 6 h. After this isopropanol was evaporated. Composite powder was dried and sieved through a microscreen.

In order to know what the content of graphene in powders is, we used elemental analysis. Composite powders which contains fine fraction of GNPs (denoted by letter f) have very small content of carbon from 0.58 to 0.94 wt. %. Contrary to this composite powders which contains sedimented fraction of GNPs (denoted by letter s) have higher content of carbon from 5.34 to 6.24 wt. % (Tab. 1).

Tab.1: Content of carbon in prepared silicon nitride-graphene composite powders

Sample	Content of C (wt. %)
G4s	5.34
G4f	0.94
G4-COOHs	5.87
G4-COOHf	0.58
G4-NH ₂ s	6.24
G4-NH ₂ f	0.77

For preparation composite powders with graphene oxide (GO) we synthesized first graphene oxide from GNPs. We used process described by Marcano et al. [3]. It is important to check whether the graphite or GNPs has been fully oxidized to graphite oxide. For this X-ray diffraction is a powerful tool. Natural graphite and GNPs exhibit strong sharp peak at 26.5°,

indicating a highly order structure. This peak disappears after oxidation of the graphite, while a new one arises at 11.5° . This correspond to the interplannar distance 0.77 nm (Fig. 1). The implication of this is that the intersheet van der Waals interactions in graphite oxide are significantly weaker in comparison to the original graphite structure. It is therefore far easier to exfoliate graphite oxide into graphene monolayers.

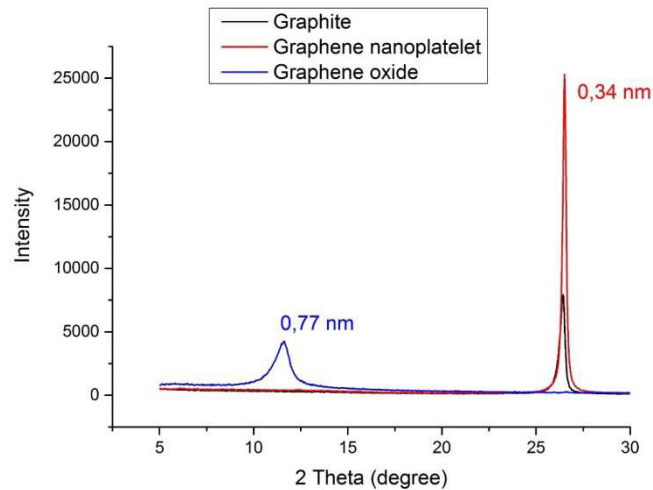


Fig. 1: XRD analysis of graphite, graphene nanoplatelets and graphene oxide

After synthesis, we prepared composites with GO by following process. Graphene oxide was ultrasonicated for 100 minutes in distilled water. Silicon nitride and sintering additives was added into solution. Suspension was mixed several hours on stirrer and after that sprayed into the liquid nitrogen. Subsequently frozen powders was placed into freeze dryer in order to remove water by sublimation. Elemental analysis shows that content of carbon in composite powder was 1.5 wt. %.

Composite powders prepared by different ways and forms of graphene (GNPs and GO) were sintered in hot press at 1650°C and 1700°C for 60 min, load 30 MPa under overpressure of N_2 .

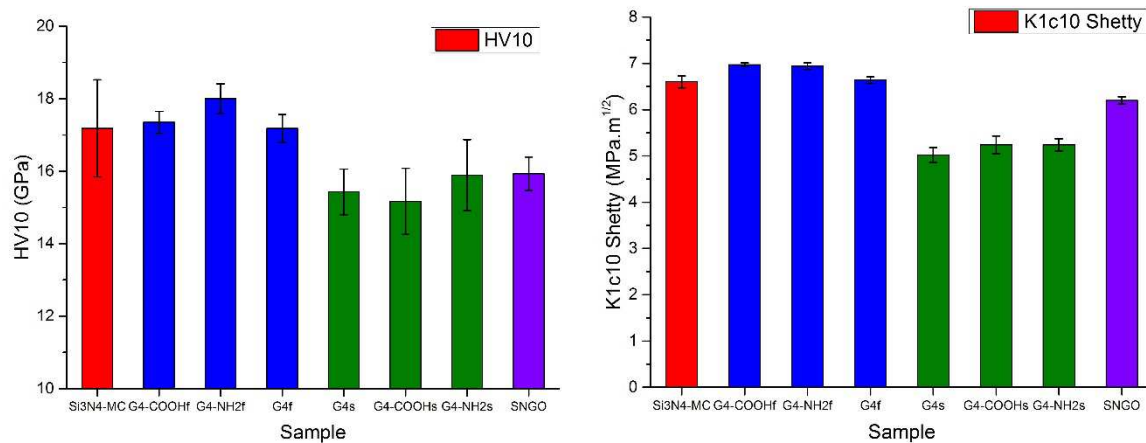


Fig. 2: Vickers hardness and indentation fracture toughness for Si₃N₄-graphene composites

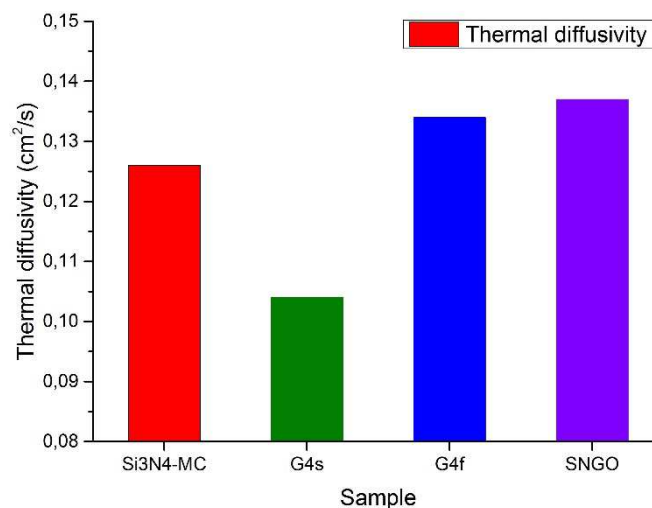


Fig. 3: Thermal diffusivity at room temperature for Si₃N₄-graphene composites

CONCLUSIONS

In this work we prepared silicon nitride composites with addition of graphene. Preparation procedures were focused on achievement of monolayer of graphene and its homogeneous distribution in ceramic matrix. Composites with fine fraction of graphene and graphene oxide exhibits similar or slightly decreased hardness and fracture toughness in comparison with reference sample without graphene. Composites with fine fraction of graphene and graphene oxide exhibits improvement in thermal diffusivity. These are only preliminary results and more investigation about microstructure, interfacial boundaries between matrix and graphene as well as influence of various content of graphene in composites must be done in order to fully understand this behaviour.

ACKNOWLEDGEMENT

This work was supported by the Slovak Grant Agency VEGA Project No. 2/0065/14 and APVV-0161-11.

REFERENCES

- [1] Geim, A. K., Novoselov, K. S. The rise of graphene. *Nat Mater* (2007);6(3):183–91.
- [2] Koratkar, N. A. *Graphene in composite materials*. DEStech Publications, Inc. (2013), ISBN 978-1-60595-056-3
- [3] Marcano, D. C. et al.: Improved Synthesis of Graphene Oxide. *ACS Nano*, (2013), vol. 4, p. 4806-4814.

**ZLEPŠENIE MECHANICKÝCH VLASTNOSTÍ B₄C KERAMICKÝCH
KOMPOZITOV PRÍDAVKOM GRAFÉNOVÝCH PLATNIČIEK**

**IMPROVEMENT OF MECHANICAL PROPERTIES OF B₄C CERAMIC
COMPOSITES BY GRAPHENE PLATELETS ADDITION**

R. Sedlák^{1,2}, A. Kovalčíková¹, P. Rutkowski³, J. Dusza¹

¹*Institute of Materials Research, Slovak Academy of Sciences, Department of Structural
Ceramics, Watsonova 47, 040 01 Košice, Slovakia*

²*Technical University of Košice, Faculty of Metallurgy, Letná 9, 040 01 Košice, Slovakia*

³*AGH University of Science and Technology in Krakow, Faculty of Material Science and
Ceramics, al. A. Mickiewicza 30, 30-059 Krakow, Poland*

ABSTRACT

Boron carbide (B₄C) based composites, containing 4–10 wt.% of graphene platelets (GPLs) as sintering additive (approximately 4 wt.%) and reinforcing phase were prepared by hot-pressing (HP) at 2100 °C for 1 h. The effect of GPLs content on microstructure and mechanical properties has been investigated. All investigated mechanical properties were the highest in the case of B₄C + 4.5 wt.% composite with bending strength of 398 MPa and fracture toughness of 5.89 MPa.m^{1/2}. Higher GPLs content resulted in lower mechanical properties except fracture toughness. Processing flaws in the form of GPLs agglomerates and structural inhomogeneities were identified as fracture origins. The main toughening mechanisms, responsible for the increased fracture toughness are crack deflection, crack branching and crack bridging.

Keywords: Boron carbide; Graphene platelets; Mechanical properties; Composites

INTRODUCTION

Boron carbide is an interesting material because of its excellent hardness (third behind diamond and cubic boron nitride), low density, high melting point, good chemical and wear stability. Due to these outstanding properties, boron carbide ceramics have great potential for many structural applications as neutron absorber, abrasive and polishing media for hard

materials and wear resistant components, armours, etc. [1–2]. Despite the excellent properties, the application of the B_4C is limited due to the difficulties in densification, low fracture toughness and low oxidation resistance beyond 1000 °C. With the aim to solve the brittle character of ceramics during the last few years new ceramic/carbon based filler composites have been developed.

Graphene is a one-atom thick layer of carbon atoms arranged into a two-dimensional (2D) honeycomb lattice. Graphene has remarkable mechanical properties, which makes it potentially a good reinforcement in ceramic composites. It also has unique electrical and thermal properties, which makes it an attractive filler for producing multifunctional ceramics for a wide range of applications [3–4].

EXPERIMENTAL MATERIALS AND METHODS

The B_4C + GPLs composites were sintered from commercial powders: micron boron carbide powder and graphene Gn(12). To avoid graphite contamination graphene was added as sintering additive instead of resin precursor. The overall content of graphene was 4 wt.% as sintering additive plus 0–6 wt.% as dispersed phase. The prepared compositions were homogenized in high-energy rotary-vibratory mill using WC-Co milling media. The homogenized and dried mixtures were hot-pressed (Thermal Technology LLC) at 2100 °C for 1 h under 25 MPa in argon flow. After sintering, specimens were cut, ground and polished to a 3 μm finish by routine ceramography procedure. Further details about material preparation can be found elsewhere [5]. Apparent densities of the sintered samples were calculated by the Archimedes method in water. The microstructures were observed by SEM (ZEISS AURIGA Compact), as shown in Fig. 1.

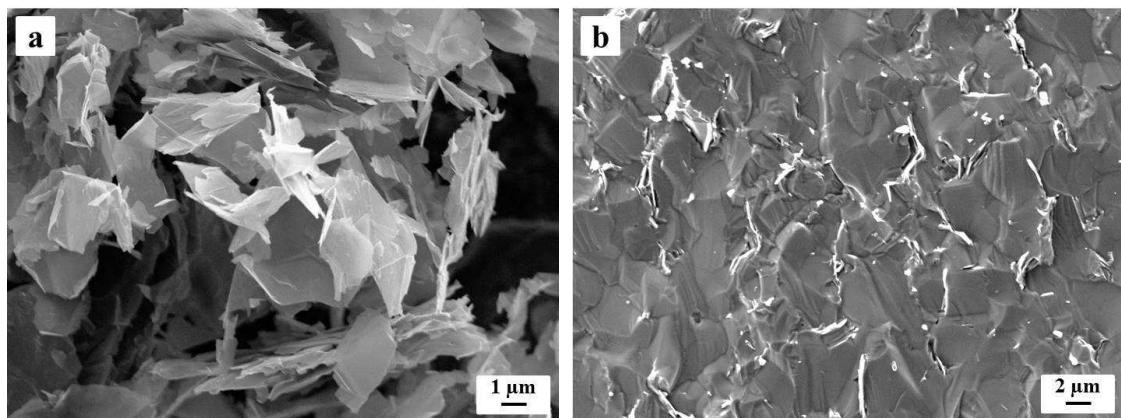


Fig. 1. a) Morphology of the GPLs; b) Microstructure of the B_4C + 4.5 wt.% GPLs system

Mechanical characterization was performed in terms of measurement of basic mechanical properties of bulk materials such as hardness and fracture toughness using indentation methods. Hardness was determined by Vickers indentation (Wolpert Wilson 432 SVD Vickers Hardness Tester) under load of 9.81 N with a dwell time of 15 s. In order to determine the indentation toughness at least 10 Vickers imprints per specimen were introduced with the load of 98.07 N in a direction parallel and perpendicular to the HP direction.

The indentation toughness was calculated from the lengths of radial cracks and indents diagonals using a formula valid for semi-circular crack systems as proposed by Shetty. Elastic modulus was measured by resonant frequency method (Buzz-o-sonic Lab Kit 5.9 by BuzzMac International, LLC) on specimens with dimensions 3 mm x 4 mm x 45 mm. The four-point bending strength values for HP samples were determined by bending tests on a tensile/loading machine (Lloyd LR 5KPlus) using specimens with dimensions 2 mm x 3 mm x 25 mm. Fractographic analysis of broken flexural specimens was used to characterize the processing flaws.

RESULTS AND CONCLUSIONS

Boron carbide + graphene composites up to 10 wt.% GPLs were fabricated by hot-pressing and the influence of graphene platelets on the mechanical properties was studied. Almost fully dense composites up to 6 wt.% GPLs was achieved. Hardness, bending strength and fracture toughness were improved at addition of 4.5 wt.% GPLs. Further increase of GPLs addition decreased apparent density and mechanical properties expect of fracture toughness, as shown in Fig. 2.

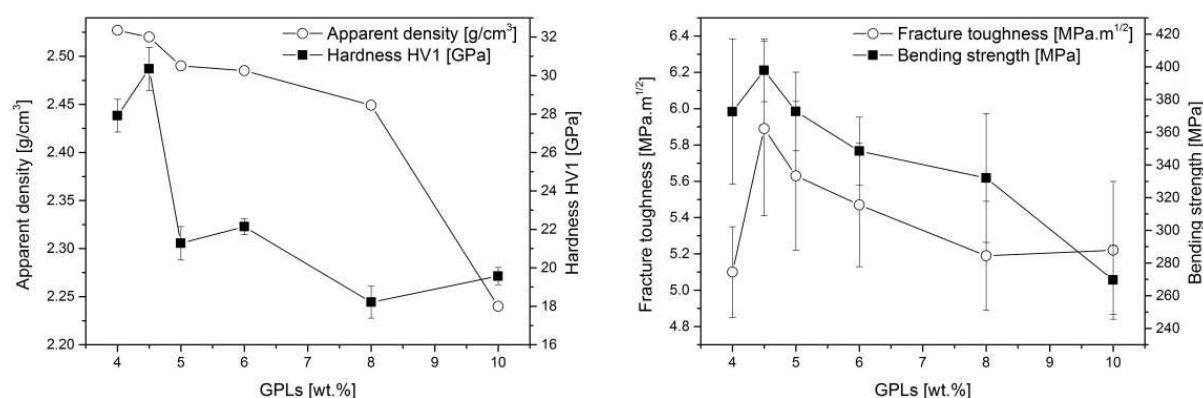


Fig. 2. Mechanical properties of the B₄C + GPLs systems

Main fracture origins during the bending strength test were processing flaws in the form of graphene agglomerates with an average size approximately 20 μm and large structural inhomogeneities. The toughening mechanisms (Fig. 3.) were similar in all composites, and were in the form of crack deflection, crack bridging in the form of graphene pull-out and/or graphene necking.

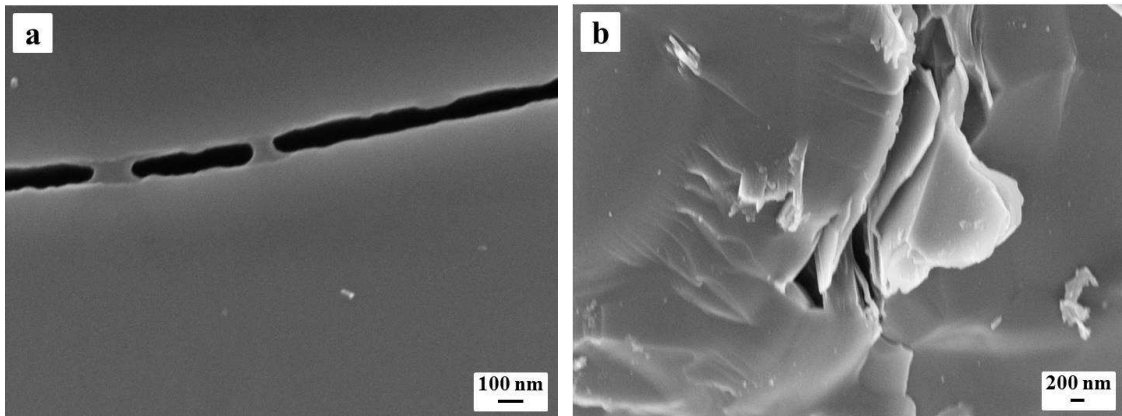


Fig. 3. Most often observed toughening mechanisms in the form of: a) bridging through GPLs necking; b) bridging in the form of GPLs pull-out

ACKNOWLEDGEMENT

The authors gratefully acknowledge for the financial support from projects: MVTs 7RP ERA.NET – GRACE, CE – CFNT-MVEP Centre of Excellence 08/2011-06/2015, VEGA 2/0043/14, VEGA 2/0189/15, APVV- 0161-11 and APVV-0108-12.

REFERENCES

- [1] Thevenot, F. Boron carbide- a comprehensive review, *Journal of the European Ceramic Society*, 6 (1990) 205–225.
- [2] Lee, H., Speyer, R.F. Pressureless sintering of boron carbide, *Journal of the American Ceramic Society*, 86 (2003) 1468–1473.
- [3] Liu, J., Yan, H., Jiang, K. Mechanical properties of graphene platelet-reinforced alumina ceramic composites, *Ceramics International*, 39 (2013) 6215–6221.
- [4] Porwal, H., Grasso, S., Reece, M.J. Review of graphene-ceramic matrix composites, *Advances in Applied Ceramics*, 112 (2013) 443–454.
- [5] Kovalčíková, A., Sedlák, R., Rutkowski, P., Dusza, J. Mechanical properties of boron carbide + graphene platelet composites, *Ceramics International*, 42 (2016) 2094–2098.

ŠTÚDIUM OXIDAČNEJ ODDOLNOSTI ZrB₂-SiC KERAMIKY DOPOVANEJ HfO₂

OXIDATION RESISTANCE OF HfO₂ DOPED ZrB₂-SiC CERAMICS.

Ľ. Bača^{1,2}, Z. Kováčová^{1,3}

¹ *Department of Ceramics, Glass and Cement, Institute of Inorganic Chemistry, Technology and Materials, Faculty of Chemical and Food Technology, Slovak University of Technology, Radlinského 9, 812 37 Bratislava*

² *Aerospace & Advanced Composites GmbH, Viktor-Kaplan-Strasse 2, 2700 Wiener Neustadt, Austria*

³ *RHP-Technology GmbH, Forschungs- und Technologiezentrum, A-2444 Seibersdorf, Austria*

ABSTRACT

Oxidation behaviour of HfO₂ doped ZrB₂-SiC ultra-high temperature ceramics prepared by rapid hot-pressing technique at 1900°C was investigated. Scanning electron microscopy (SEM) together with EDX analysis revealed the formation of core-shell microstructure of Zr(Hf)B₂ solid solution due to the reduction of HfO₂ on grain boundaries during sintering. In comparison to the undoped ZrB₂-SiC ceramics the oxidation resistance of HfO₂ doped ZrB₂-SiC UHTCs seem to be slightly higher at temperatures up to 1500 °C in static air atmosphere.

Keywords: ZrB₂-SiC, HfO₂, oxidation resistance, microstructure

INTRODUCTION

Refractory diborides especially HfB₂ and ZrB₂ are being studied with great interest because of their high melting point (3380 °C vs. 3245 °C), metal like thermal (> 60 W m⁻¹K⁻¹) and electrical conductivity (~ 10⁷ S m⁻¹), chemical inertness against molten metals and superb thermal shock resistance. These properties make them attractive candidates for high temperature and extreme applications such as thermal protection materials on hypersonic aerospace vehicles or future re-usable atmospheric re-entry civilian aircrafts flying up to Mach 6. ^{1,2}

Since the 1960s, studies have revealed that these diborides are the most resistant to oxidation among other diborides, first HfB₂ followed by ZrB₂. However, an advantage of ZrB₂ is lower price and theoretical density. For monolithic ZrB₂ the oxide formed on the oxidation is B₂O₃, which is liquid above 450 °C and wets the zircon dioxide grains until it volatilizes at temperatures above 1100 °C. This is followed by parabolic oxidation kinetics due to the mass gain from ZrO₂ and B₂O₃ formation and mass loss from B₂O₃ vaporization up to 1400 °C. A significant improvement of oxidation characteristics of above mentioned diborides has been done by addition of SiC in optimum amount of 15 – 20 vol. %. This and other additives in diboride matrix produce borosilicate glass when oxidised. This glass acts then as a barrier to diffusion of oxygen to the substrate, however only up to ~ 1650 °C, when the combination of aerodynamic flow and high heat flux together with oxygen atmosphere decreases oxidation protection. A promising approach in the further improvement of oxidation resistance seems to be an application of other additives that affect the composition and structure of the crystalline oxide scale (inhibiting of the ZrO₂ polymorphic transformation, forming protective refractory phases or modifying the microstructure of the ZrO₂ scale) at temperatures above 1650 °C.³

In this work the addition of hafnia on the oxidation resistance of ZrB₂-SiC UHTCs was investigated.

EXPERIMENTAL

Discs with 50 mm diameter were fabricated by rapid hot-pressing (DSP518, Dr. Fritsch Sondermaschinen GmbH, Germany) using a graphite die from ZrB₂ (6.1 μm, ABCR) and SiC (0.9 μm, ESK GmbH) powders. The powder mixtures of ZrB₂ - 20 wt. % SiC (ZS) and 5 wt.% HfO₂ doped ZrB₂ - 20 wt. % SiC (ZS-5H) were homogenized on rolls in cyclohexane using zirconia balls for 24 hours and dried in evaporator. Small cylinders with diameter 10 mm and height 4-5 mm were cut out from hot-pressed discs by electrical discharge machining (EDM) and exposed to oxidation. Oxidation tests were carried out in a furnace at 1100, 1300, 1500 and 1650 °C for 60 minutes in stagnant air. The phase compositions of selected samples was analysed by an X-ray diffraction Stoe Theta-Theta with CoK α radiation). Oxidation resistance was evaluated according to the mass changes and layer thickness after oxidation. The specimen surfaces and microstructure were observed using light (Leica DMI 5000M equipped with digital camera DP 25 Olympus and with a soft imaging system “Scandium” for image processing and 2D/3D image analysis) and field emission scanning electron microscopy (FE SEM, Carl Zeiss SUPRA TM 40VP).

Depending on the selected temperature ZrB_2 -SiC ceramics undergo oxidation according to reactions very well described in the literature.⁴ The physical and chemical processes that occur at the exposed surface depend on the microstructure and composition, having beneficial or detrimental effect on the material's oxidation resistance. The addition of 5 wt. % of HfO_2 into the ZrB_2 -SiC UHTCs is studied based on the consideration that hafnia can positively influence the oxidation resistance of UHTCs by partial stabilization of zirconia. Hafnia, like zirconia, undergoes a reversible monoclinic-tetragonal crystallographic inversion when heated to its transformation temperature, but the hafnia crystallographic transformation is far less destructive. This is because the volume change in hafnia is about half of that experienced by zirconia.⁵ Moreover the transformation (monoclinic-tetragonal) occurs at a much higher temperature (approx. 1700° C) over a smaller temperature range and with less thermal stress.⁶

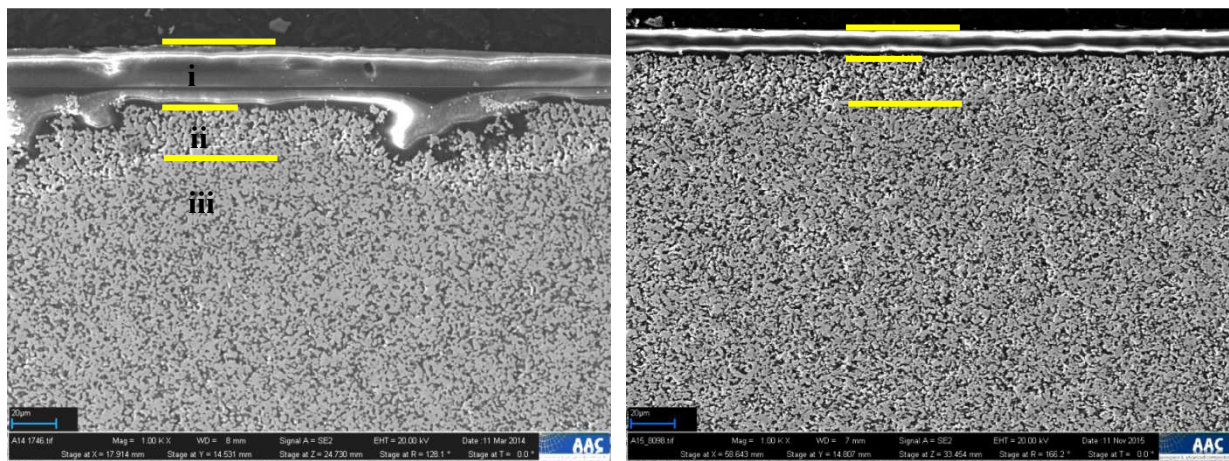


Fig. 1. SEM images of cross-sections of a) ZrB_2 -SiC (ZS) and b) ZrB_2 -SiC doped with 5 wt. % HfO_2 (ZS-5H) samples after oxidation at 1500 °C for 1h in static air.

Figure 1 shows the cross-sectional micrographs of the oxidized undoped and HfO_2 doped ZrB_2 -SiC UHTCs at 1500°C for 1h in static furnace atmosphere. Both samples showed similar layered characteristics typical for oxidized ZrB_2 -SiC ceramics containing (i) a silica rich glass outer layer, (ii) a subscale of zirconia/zirconia hafnia embedded in silica, and finally (iii) unaltered material. However the thickness of the oxide scale for ZS-5H was far less than that for ZS. The surface of sample ZS was covered approximately 20 μm thick glass layer in comparison with 5 μm thick glass layer of ZS-5H sample. On the other hand the thickness of subscale ZrO_2/HfO_2 – SiO_2 layer in ZS-5H sample was only 5 μm thinner as for basic UHTC sample. These preliminary results showed, that the glassy layer in ZS-5H sample is almost 3 times thinner as for sample without HfO_2 addition. It could indicate that the HfO_2 can increase the viscosity of borosilicate glass (BS) and thus slow down the oxygen diffusion to the

unaltered material. The increase of the BS viscosity can cause the reduction of the thickness of outer borosilicate glass layer. Similar behaviour was also observed in the case of La_2O_3 doped ZrB_2 -20 vol. SiC ceramics.⁷

CONCLUSIONS

Hafnia addition decreases oxide scale layer after exposure to air environment at 1500°C for one hour and seems to be beneficial for oxidation protection due to the increase of the BS viscosity. This led to the reduction of thickness of outer BS glass inhibiting the oxygen diffusion to the unaltered UHTCs.

ACKNOWLEDGMENTS

The authors acknowledge Dr.Ch.Jogl, AAC GmbH for SEM analysis.

LITERATÚRA

- [1] Wuchina, E., Opila, E., Opeka, M., Fahrenholtz, W., Talmy, I. UHTCs: Ultra-high temperature ceramic materials for extreme environment applications. *Electrochem. Soc. Interf.*, 2007, vol. 16, pp. 30-36.
- [2] Justin, J. F., Jankowiak, A. Ultra high temperature ceramics: densification, properties and thermal stability. *Onera J. Aerosp.*, 2011, vol. 3, pp. 1-11.
- [3] Eakins, E. Jayaseelan, D. D. Lee, W. E. Toward Oxidation-Resistant ZrB_2 -SiC Ultra-High Temperature Ceramics. *Metall. Mater. Trans.*, 2011, vol. 42A, pp. 878–887.
- [4] Fahrenholtz, W. G., Hilmas, G. E. Oxidation of ultra-high temperature transition metal diboride ceramics. *Int. Mater. Rev.*, 2012, vol. 57, pp. 61-72.
- [5] Curtis, C. E., Doney, L. M. and Johnson, J. R. Some properties of hafnium oxide, hafnium silicate, calcium hafnate and hafnium carbide. *American Ceramic Society Journal* 1954,37: 458-465.
- [6] Ohnysty, B. and Rose, F. K. Thermal expansion on thoria and hafnia to 4500 °F. *American Ceramic Society Journal* 1964, 47, 398-400.
- [7] Zapata-Solvas, E., Jayaseelan, D. D., Brown, P.M., Lee, W.E., Effect of La_2O_3 addition on long-term oxidation kinetics of ZrB_2 -SiC and HfB_2 -SiC ultra-high temperature ceramics. *J.Europ. Ceram. Soc.* 2014, 34, 3535-3548

DISLOKÁCIE ZALOŽENÉ NA PLASTICITE V ZrB₂ MIKROPILIEROCH

DISLOCATION BASED PLASTICITY IN ZrB₂ MICROPILLARS

T. Csanádi¹, A. Kovalčíková¹, J. Dusza¹

¹*Institute of Materials Research, Slovak Academy of Sciences, Watsonova 47, 04353 Košice,
Slovak Republic*

ABSTRACT

Room temperature deformation behaviours of ZrB₂ micropillars, fabricated by focused ion beam technique from differently oriented grains of polycrystalline ZrB₂, were investigated under micro compression. Considerable anisotropy was found showing ~80% higher yield (σ_Y) and rupture (σ_r) stress values for the basal oriented pillars compared to the prismatic pillars. Micro-scale plasticity was detected in prismatic oriented pillars, revealing the activation of the $\{10\bar{1}0\}\{11\bar{2}3\}$ type slip system both in the form of single- and multiple-slip which is anomalous for ZrB₂ and has not been reported so far in the relevant literature.

Keywords: Zirconium diboride; Micropillar compression; Slip activation; Plasticity; Anisotropy

INTRODUCTION

Zirconium diboride (ZrB₂) is an important member of the UHTCs family due to its high melting point (>3000 °C), high oxidation resistance above 1500 °C and excellent thermal and electrical conductivity [1,2]. The individual grains within the polycrystalline ZrB₂ are essentially single crystals with orientation-dependent mechanical properties. It is necessary to understand these anisotropic deformation behaviours of ZrB₂ grains in order to model and design optimized microstructures with an enhanced combination of strength, fracture toughness and wear resistance according to the requirements of the engineering applications [3].

In the last 40 years, several investigations focused on understanding the hardness anisotropy and possible deformation mechanisms at room and elevated temperatures in ZrB₂ single crystals [4-6] and polycrystalline composites [7-9]. Microindentation studies revealed higher hardness on basal oriented grains in comparison with the prismatic [4]. At that time, transmission electron microscopy (TEM) investigations confirmed the activation of the

$\{10\bar{1}0\}\{11\bar{2}0\}$ type slip system, which is typical for hexagonal crystals, as the only responsible mechanism for room-temperature plastic deformation in single crystal ZrB_2 [5]. Recent scratch [7,8] and indentation [9] investigations on polycrystalline ZrB_2 and $\text{ZrB}_2\text{-SiC}$ composites have also revealed plastic deformation features in the form of slip-lines with the activation of the $\{10\bar{1}0\}\{11\bar{2}0\}$ slip system [8]. The plasticity of brittle materials has been studied extensively in the last ten years using micropillar compression. At first, the technique was applied to metals and later it was successfully adopted for ceramics. The work presented here is the first reported investigation of the deformation behaviour of ZrB_2 micropillars.

The aim of the present work is to study the room temperature deformation anisotropy of ZrB_2 grains in polycrystalline ZrB_2 under micropillar compression.

EXPERIMENTAL

The experimental material was a spark plasma sintered (SPS) ZrB_2 sample prepared using a two steps SPS process. Further details about material preparation can be found elsewhere [10]. Prior to RT compression, the ZrB_2 sample was subjected to careful surface preparation which was followed by scanning electron microscopy (SEM) and electron backscatter diffraction (EBSD) analyses to select large grains close to basal (0001) and prismatic $\{10\bar{1}0\}$ orientations for micro-pillar fabrication, as shown in Fig. 1.

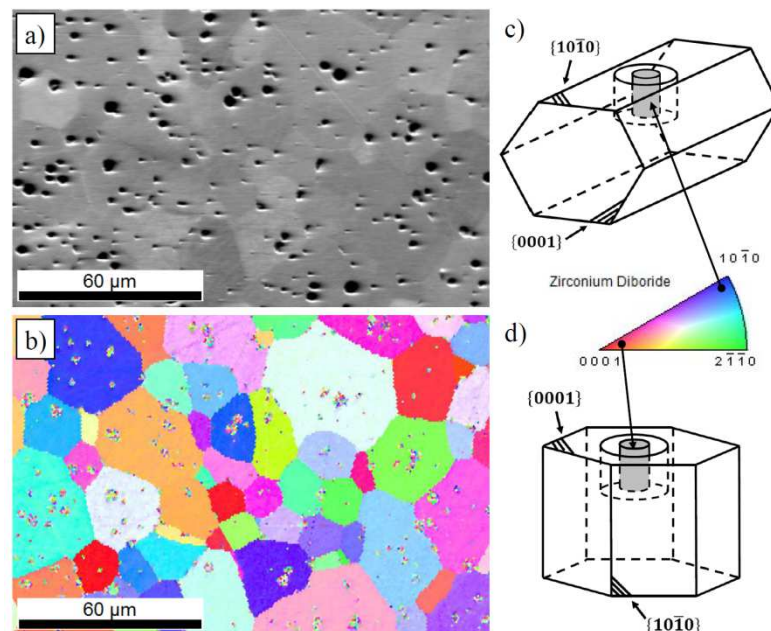


Fig. 1. Microstructure of polycrystalline ZrB_2 sample by: a) SEM and; b) EBSD. Schematic representation of micropillars fabricated in: c) prismatic and; d) basal oriented grains.

Micropillars with diameter of $\sim 2.5 \mu\text{m}$ and height of $\sim 5 \mu\text{m}$ were fabricated in pore-free regions of selected grains using the FIB technique in a FEI Quanta 3D machine. Schematic positions of micropillars in the selected grains are illustrated in Figs. 1c,d. Four pillars were prepared and tested in each orientation. Micropillar compressions were performed at room temperature using a depth-sensing indentation machine (UMIS CSIRO) fitted with a flat-ended conical diamond tip. The technical details of the compression tests and the evaluation of the yield and rupture stresses were the same as previously reported for WC and $\beta\text{-Si}_3\text{N}_4$ crystals by the present authors [11,12]. Additional details can be found in elsewhere [10].

RESULTS AND CONCLUSIONS

Room temperature deformation behaviours of ZrB_2 micropillars along basal and prismatic orientation were investigated by micro-compression tests. The anisotropic ratio between basal and prismatic orientations in yield and rupture stress values was around 1.8 with values of $\sigma_{Y,basal} = 13.4 \pm 1.0 \text{ GPa}$, $\sigma_{r,basal} = 13.4 \pm 1.0 \text{ GPa}$ and $\sigma_{Y,prism} = 6.4 \pm 0.9 \text{ GPa}$, $\sigma_{r,prism} = 7.6 \pm 0.8 \text{ GPa}$, respectively.

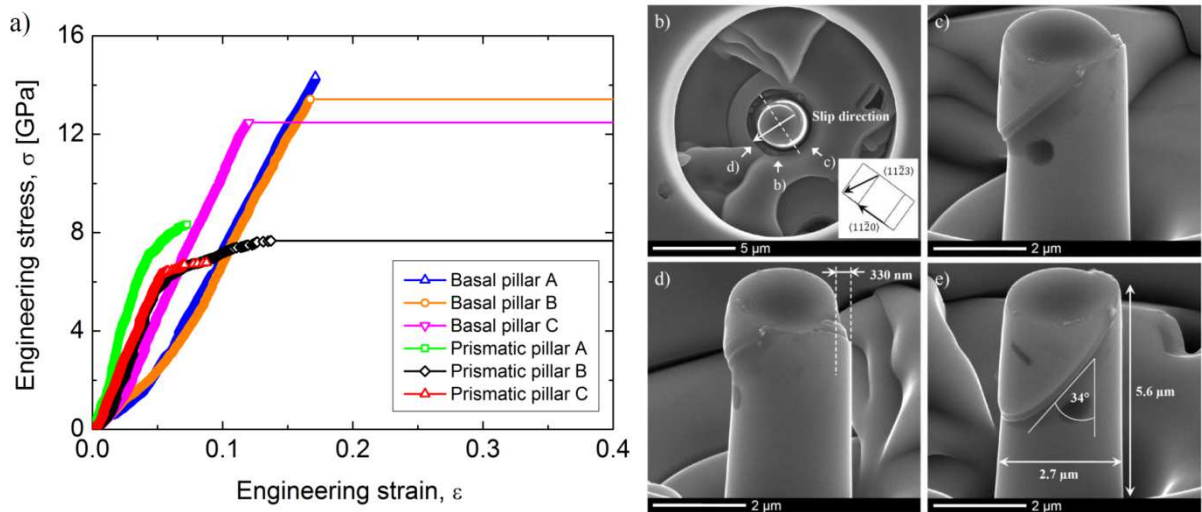


Fig.2. Characteristic engineering stress-strain curves for a) basal and prismatic oriented grains under micro-compression together with a graph showing microplasticity. Single-slip activation during micro-compression of Prismatic pillar C from a) top and b) side and side views after a rotation of c) -45° and d) 45° .

Micro-scale plasticity was observed in prismatic orientations due to the activation of the $\{10\bar{1}0\}\{11\bar{2}3\}$ type slip system both in the form of single- and multiple-slip which has not been previously reported for ZrB_2 . Schmid-factor calculations revealed that this slip system has a lower critical resolved shear stress compared to the commonly reported $\{10\bar{1}0\}\{11\bar{2}0\}$

slip system. Finally, dislocation energetic calculation confirmed the presence of the $\frac{1}{3}\langle 11\bar{2}3 \rangle$ Burgers vectors in ZrB₂ which is the consequence of the dissociation of (0001) type dislocations into partials. Further details can be found in our recent paper [10].

ACKNOWLEDGEMENTS

The work was supported by the project Slovak Grant Agency for Science, grant No. 2/0122/12 and by CE SAS CLTP-MREC. The work of NQC was supported by Hungarian Scientific Research Fund (OTKA) under Grants No. K109021 and K109570. The authors would like to thank G. Varga and Z. Dankházi (ELTE University, Budapest) for EBSD measurement and SEM investigation. The support of Keysight Technologies is greatly acknowledged.

REFERENCES

- [1] Sciti, D., Monteverde, F., Guicciardi, S., Pezzotti, G., Bellosi, A. Microstructure and mechanical properties of ZrB₂-MoSi₂ ceramic composites produced by different sintering techniques. *Mater. Sci. Eng. A* 434 (2006) 303-309.
- [2] Li, H., Zhang, L., Zeng, Q., Wang, J., Cheng, L., Ren, H., Guan, K. Crystal structure and elastic properties of ZrB compared with ZrB₂: A first-principles study. *Comp. Mater. Sci.* 49 (2010) 814-819.
- [3] Guo, S-Q. Densification of ZrB₂-based composites and their mechanical and physical properties: A review. *J. Eur. Ceram. Soc.* 29 (2009) 995-1011.
- [4] Nakano, K., Imura, T., Takeuchi, S. Hardness anisotropy of single crystals of IVa-diborides. *Japan. J. Appl. Phys.* 12 (1973) 186-189.
- [5] Haggerty, J.S., Lee, D.W. Deformation anisotropy of ZrB₂ single crystals. *J. Am. Ceram. Soc.* 54 (1971) 572-576.
- [6] Xuan, Y., Chen, C-H., Otani, S. High temperature microhardness of ZrB₂ single crystals. *J. Phys. D: Appl. Phys.* 35 (2002) L98-L100.
- [7] Ghosh, D., Subhash, G., Radhakrishnan, R., Sudarshan, T.S. Scratch-induced microplasticity and microcracking in zirconium diboride-silicon carbide composite. *Acta Mater.* 56 (2008) 3011-3022.
- [8] Ghosh, D., Subhash, G., Bourne, G.R. Room-temperature dislocation activity during mechanical deformation of polycrystalline ultra-high-temperature ceramics. *Scripta Mater.* 61 (2009) 1075-1078.

- [9] Guicciardi, S., Melandri, C., Monteverde, F.T. Characterization of pop-in phenomena and indentation modulus in a polycrystalline ZrB_2 ceramic. *J. Eur. Ceram. Soc.* 30 (2010) 1027-1034.
- [10] Csanádi, T., Szommer, P., Chinh, N.Q., Grasso, S., Dusza, J., Reece, M. Plasticity in ZrB_2 micropillars induced by micropillar compression. *J. Eur. Ceram. Soc.* (2015) <http://dx.doi.org/10.1016/j.jeurceramsoc.2015.10.035>
- [11] Csanádi, T., Břanda, M., Duszová, A., Chinh, N.Q., Szommer, P., Dusza, J. Deformation characteristics of WC micropillars. *J. Eur. Ceram. Soc.* 43 (2014) 4099-4103.
- [12] Csanádi, T., Chinh, N.Q., Szommer, P., Dusza, J., Lenčés, Z., Šajgalík, P. Deformation and fracture of β -silicon nitride micropillars. *J. Am. Ceram. Soc.* 98 (2015) 374-377.

HYDROTERMÁLNA KORÓZIA KERAMICKÝCH VRSTIEV PRIPRAVENÝCH Z ORGANOKREMIČITÝCH PREKURZOROV

HYDROTHERMAL CORROSION OF POLYMER DERIVED GLASS CERAMIC LAYERS

I. Petříková¹, M. Parchoviansky¹, G. Barroso², G. Motz², D. Galusková¹, D. Galusek¹

¹*Vitrum Laugaricio – Joint Glass Center of the IIC SAS, TnU AD, and FCHT STU,
Študentská 2, 911 50 Trenčín, Slovakia*

²*University of Bayreuth, Ceramic Materials Engineering, D-95440 Bayreuth, Germany*

ABSTRACT

The work was aimed at development of an environmental barrier coating system for corrosion protection of steel consisting of polymer derived ceramic (PDC) bond-coat and PDC top-coat with glass and ceramic fillers. In order to investigate the environmental protection ability of the coatings, static corrosion tests under hydrothermal conditions were conducted. SEM investigation showed that the composite coatings before tests were not fully dense, thus the corrosive medium could penetrate through defects to the metal/coating interface and cause delamination and failure of the coatings.

Keywords: polymer derived ceramics, glass microspheres, coatings, hydrothermal corrosion

INTRODUCTION

Polymer derived ceramics (PDC) matrix composite coatings are a promising candidate to be used as alternative environmental barrier coatings, such as in corrosion protection. The coatings are mainly based on silicon containing precursors like polysilazanes [1]. The precursor technique exhibits a relatively low-cost and easy approach to produce polymeric and ceramic coatings, which are able to provide excellent oxidation and corrosion protection of metal substrates [2]. The greatest disadvantage of PDCs is the shrinkage of the polymer during pyrolysis, which can be higher than 50% by volume [3]. Residual stresses caused by the high volume shrinkage lead to the formation of defects, cracks or even delamination of the coatings. By adding passive fillers like SiC, BN, ZrO₂, Al₂O₃ and/or active fillers like TiSi₂,

or $ZrSi_2$ the volume change due to polymer to ceramic conversion can be significantly reduced. Furthermore, depending on the properties of the substrate, the thermal expansion coefficient of the coatings can be adjusted by an adequate filler material. Moreover, by incorporation of glass fillers it is also possible to generate coatings with additional functionalities and increase the efficiency as environmental barrier coating [2].

The work was aimed at development of corrosion resistant environmental barrier coating system. For that purpose, a double layer coating, consisting of a PDC bond-coat, and a PDC top-coat with ceramic and specially tailored glass fillers ($SiO_2-Al_2O_3-ZrO_2$) in the form of microspheres with high melting temperature were prepared and studied from the point of view of their corrosion resistance under hydrothermal conditions.

EXPERIMENTAL

The preparation of the EBCs consisted of two main steps: the synthesis of the glass fillers and the processing of the coatings. At first, the glass microspheres were prepared by combination of a modified Pechini sol-gel method and flame synthesis. Five compositions with different $SiO_2-Al_2O_3-ZrO_2$ weight ratios were prepared (80-10-10; 60-30-10; 50-40-10; 50-30-20; 50-20-30). Flat stainless steel (AISI 441) plates were cut into sheets, ultrasonically cleaned in acetone and dried. The bond-coat was prepared from preceramic polymer PHPS (perhydropolysilazane, AZ Electronic Materials GmbH) by dip-coating of the metal sheets. The pyrolysis of the bond-coat was performed in air at a temperature of 500 °C for 1 h with heating and cooling rates of 5 K/min. The top coat was prepared by mixing defined volume fractions of ceramic filler particles (YSZ, $ZrSi_2$), glass microspheres ($SiO_2-Al_2O_3-ZrO_2$) of various compositions and a liquid polysilazane Durazane 1800 by spray-coating technique. The pyrolysis of the composite coatings was performed in air (electric oven Nabertherm® LH 60/14, Nabertherm, Germany) at the temperature 1000 °C with the heating and cooling rates of 3 K/min and a holding time of 1 h. The corrosion tests were performed in Teflon-lined pressure corrosion reactors with the inside volume of 26 cm³ filled with deionized water as a corrosion liquid and heated in laboratory drying oven. Static tests were carried out at the temperature of 200°C with the duration between 1 and 8 days. The corrosion medium was not changed during the whole duration of test. The SEM/EDS examination of coatings before and after corrosion tests was conducted with the use of a FEG SEM JEOL 7600f and was focused at evaluation of homogeneity, adhesion and possible failures of the coatings.

Fig. 1a shows the SEM micrograph of a top coat before corrosion tests. The composite coatings were not fully dense, and contained small closed pores and cracks. Occasionally also

delamination was observed both within the coating or at the metal/ceramic interface of the approximately 10 μm thick coatings, due to high volume shrinkage of the precursor during pyrolysis. On the other hand, the adhesion of the bond coat at the metal/PHPS and PHPS/top coat interfaces was very strong. Due to reactivity of PHPS, direct chemical bonds between the stainless steel substrates and the PHPS were formed [2]. Glass microspheres with diameter of approximately 10 μm deliberately added as a passive filler were also observed.

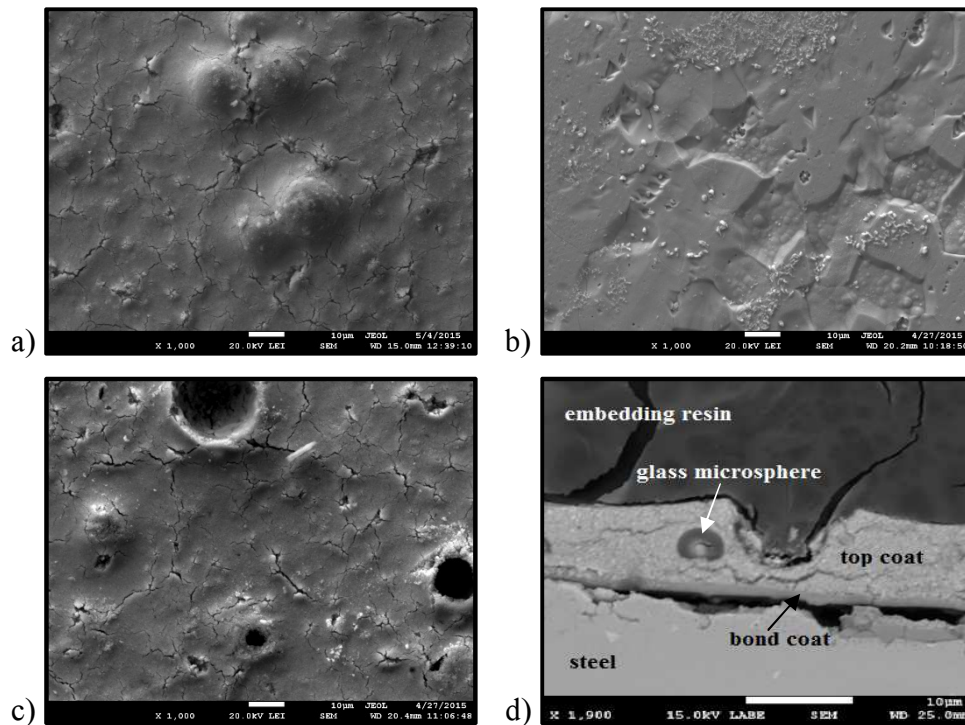


Fig. 1. SEM micrographs of a) top coat before corrosion tests, b) uncoated steel sheet after 8 days of hydrothermal corrosion at 200 °C, c) surface of the top coat corroded under the same conditions, d) cross-section of the composite coating after corrosion

Fig. 1b shows the SEM micrograph of steel surface after corrosion tests. The uncoated steel substrate is partially oxidized after corrosion tests at the temperature 200°C after 8 days, the crystals visible at the metal surface were identified by EDS analysis as a mixture of iron and chromium oxide. No oxidation of the top coat can be detected after the static corrosion tests (Fig. 1c). However, randomly distributed spherical craters approximately 10 μm in diameter can be seen on the surface of the top coat, formed by pull out of glass microspheres. This can be attributed to the differences of thermal expansion coefficients of the fillers and the PDC matrix and the absence of chemical bonding between coating and the glass filler, which results in penetration of corrosion medium to glass/ceramic interfaces and eventually to preferential dissolution of material at the glass/coating boundary followed by pull-out

of microspheres from the ceramic layer. Since the prepared coatings were not fully dense, coated samples were not protected by the PDC coatings. The composite coating system with a thickness of about 15 μm did not adhere to substrate after the corrosion test and contained numerous cracks, which penetrated to the metal surface (Fig. 1d). The corrosive medium (water) was thus able to penetrate through the defects to the ceramic-metal interface. It then reacted with the metal near the interface, causing the coating to debond from the substrate and allowing further exposure to the corrosive environment. Therefore, the pre-existing defects in the composite coatings have a significant impact on their corrosion resistance.

CONCLUSION

In this work, a double layer polysilazane-based environmental coating system for steel was prepared and studied from the point of view of its corrosion resistance under hydrothermal conditions. Since the prepared coatings were not fully dense, the static corrosion tests did not deliver promising results. Application of the static conditions caused delamination of the bond coat from steel substrate and the failure of composite coatings. In order to increase corrosion resistance it is necessary to prepare dense coatings, through optimization of the composition of coatings and use of glass filler microspheres with higher thermal expansion coefficient and smaller diameter.

ACKNOWLEDGEMENTS

Financial support of this work by the grant VEGA 2/0058/14, and by the Alexander von Humboldt Foundation in the frame of the institutional cooperation grant scheme is gratefully acknowledged. This publication was created in the frame of the project "Centre of excellence for ceramics, glass, and silicate materials" ITMS code 262 201 20056, based on the Operational Program Research and Development funded from the European Regional Development Fund.

LITERATURE

- [1] Lukacs, A. Polysilazane precursors to advanced ceramics, *Am. Ceram. Soc. Bull.*, 86 (2007) 9301-9306.
- [2] M. Günthner et al. High performance environmental barrier coatings, Part I: Passive filler loaded SiCN system for steel, *J. Eur. Ceram. Soc.*, 31 (2011), 3003 – 3010.
- [3] P. Greil. Active-Filler-Controlled Pyrolysis of Pre ceramic Polymers, *J. Am. Ceram. Soc.*, 78 (1995) 835–848.

KORÓZIA KOVU V KONTAKTE SO SKLOM V PARÁCH KYSELINY OCTOVEJ

CORROSION OF METAL/GLASS JOINTS IN ACETIC ACID VAPOURS

A. Nowicka¹, D. Galusková¹, E. Greiner – Wronowa², D. Galusek¹

¹*Vitrum Lauguricio – Joint Glass Center of the IIC SAS, TnU AD, and FCHT STU,
Študentská 2, 911 50 Trenčín, Slovakia*

²*AGH- Technical University of Science and Technology, Ave.Mickiewicz 30, Kraków, Poland*

ABSTRACT

Most of the museum exhibitions are located in the old and often historical buildings where it is difficult to have stabilized temperature and humidity. Moreover the environmental control in housing institutions was oriented towards the convenience of the visitors and staff. Cyclical changes of temperature and relative humidity along with the presence of volatile organic compounds emitted from plywood and wood products can deteriorate historical value of displayed objects. The aim of this work was investigation of corrosion resistance of glass/metal joints in contact with the acidic vapour simulating environmental museum condition (collections including jewellery or other glassy historical objects). Two environmental conditions were applied: constant temperature and relative humidity and night/day cycle mode. Specimens were in contact with vapours generated from 50% acetic acid. Samples before and after corrosion test were examined by the optical microscopy and scanning electron microscopy. Metal and glass interacted individually with the acetic acidic vapours, but mutual interactions between metal and glass were also observed as a result of glass induced metal corrosion.

Keywords: corrosion, glass, metal, volatile organic compounds, museum environment.

INTRODUCTION

The mechanism of corrosion of glass and metal is well known, but it is worth to pay attention to the glass/metal connections. The deterioration of ancient and historic glass/metal joints within museum collection results in visual alteration and physical damages [1]. Historical objects are exposed to different corrosion agents occurring in museum environment. Temperature and relative humidity (RH) variations, gaseous and particulate pollution all play an important role in deterioration of museum objects [2]. Acetic acid is major corrosive pollutant in indoor cultural heritage premises. In particular acetic acid is known to be emitted

from all natural woods with hardwoods, e.g. oak, being thought to emit the highest concentrations of acetic acid. The source of acetic acid is, in part, due to the hydrolysis of acetyl group esters in the hemicellulose, which constitutes roughly one-third of total carbohydrates in the wood [3]. Acetic acid with appearance of high relative humidity causes corrosion of historical objects such as glass, metals and their joints. Sodium copper formate acetate is detected on high alkali glass/metal objects exposed to long term emissions from wood. A higher pH value may also lead to basic compounds, which normally do not form. Corroding glass forms alkaline surface films, which may lead to the metal corrosion products in the contact zone, for example different sodium copper carbonates. Most of the corrosion products in glass/metal connection remain unspecified as yet [4].

EXPERIMENTAL

To study the corrosion mechanism between glass/metal joints and the acetic acid vapors two different parameters, e.g. temperature (T) and relative humidity (RH) were used. The first experiment was carried out for 20 days in the climatic chamber with average parameters of temperature and relative humidity: T=51.9°C, RH= 45.3%. Secondly the day/night cycle mode simulating the real parameters of temperature and relative humidity in museums was carried out 336 hours (14 d). The following conditions were set up:

- a) day mode: RH 45%; T 25°C
- b) night mode: RH 60%; T 20°C.

A specimen of glass with high content of alkaline elements covered with a copper tape were corroded in vapours generated from the solution containing 50 % of the acetic acid. The composition of high alkaline glass (73,94% SiO₂; 14,48% K₂O; 9,26% CaO; 0,84% Na₂O; 0,64% B₂O₃; 0,59% MgO; 0,14% BaO; 0,066% PbO; 0,065% Al₂O₃; 0,056% Fe₂O₃) is similar to a glass dated to the 18th century, which is part of the collection of the National Museum in Cracow [5].

RESULTS

The surface of the corroded specimen was analyzed with the Optical (OM) and Scanning Electron Microscopy (SEM) in order to evaluate the surface changes and to compare influence of different parameters of the test (T, RH, cycle mode). Examination of the metal surface after the test by the optical microscopy (Fig 1 a) showed significant changes of microstructure and presence of unknown phase of a globular shape (Fig. 1 b). Near the contact zone between copper and glass were observed deposits of the unknown corrosion product.

Wavy but relatively smooth appearance of the uncorroded metal surface (Fig 2 a) significantly changed and angular units of a different dimension completely covered the copper tape. Globular units assembled from the angular crystals were randomly scattered on the corroded Cu tape (Fig 2 b).

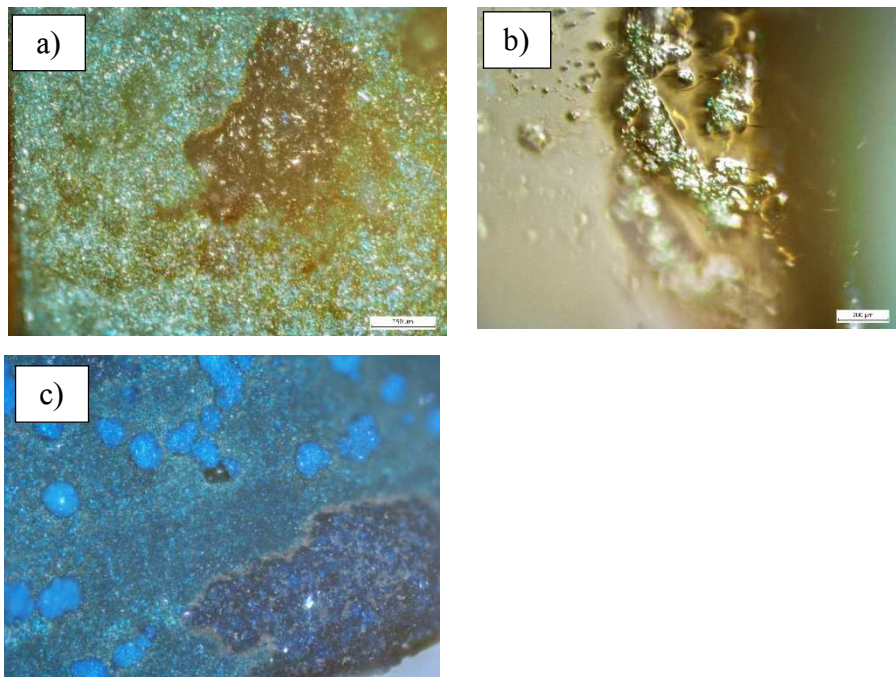
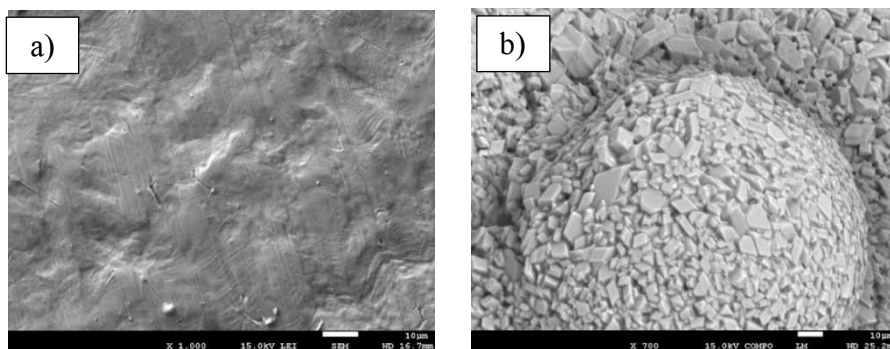


Fig.1: Surface of metal exposed to the acetic acid vapours under constant conditions a); deposits of an unknown phase scattered on the glass surface b); surface of metal covered with globular precipitates after application of night/day cycle mode c).



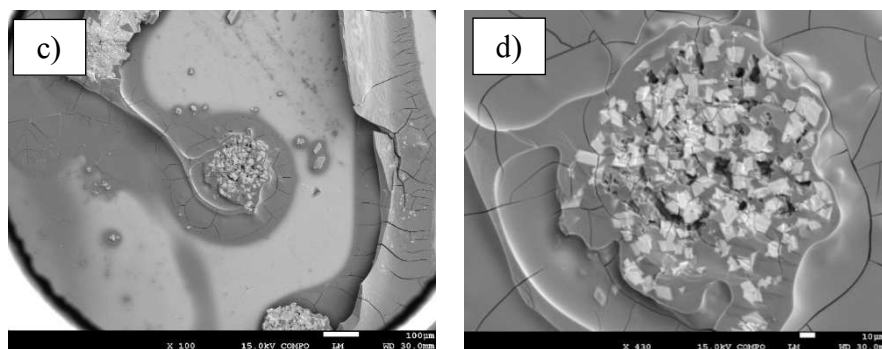


Fig.2: SEM micrographs of the copper surface before corrosion test (a); SEM micrograph of the globular precipitate on a corroded Cu tape (b). Metal/glass joint area after corrosion test c) and detail of the unknown internal crystalline phase in the metal/joint area d).

Unknown crystalline phase was also detected in the area where metal was connected to the glass (Fig 2 c and d). In the area of the metal/glass joint acetic vapours could be trapped and accumulated, and change the corrosion environment into more concentrated with respect to the content of acetate ions. Additionally corrosion effect could be enhanced by leaching of alkalies from the glassy surface. Changing of conditions from acidic to alkaline often results in attack on the silica network itself. It is assumed that glass induced metal corrosion accompanied with electrochemical reactions between metal and leached alkaline elements from the glass could result in formation of crystalline precipitates, resulting in visible deterioration of the historical objects.

CONCLUSIONS

Alkaline silicate glasses compositionally related to the historical glass from the 18th century were tested in acetic acidic vapours. The attention was focused on corrosion resistance of the metal (Cu)/glass joints.

Based on the analysis from the electron microscopy we can conclude that metal and glass interact individually with the acetic acidic vapours but mutual interactions between metal and glass occurs as a result of glass induced metal corrosion.

Microstructure of the metal and glass changes due to formation of corrosion products of as yet unknown chemical and phase composition.

ACKNOWLEDGEMENTS

The financial support of this work by the VEGA grant 2/0058/14 is gratefully acknowledged. The publication was created in the frame of the project "Centre of excellence for ceramics, glass and silicate materials", ITMS code 26220120056, based on the Operation Program Research and Development funded from the European Regional Development Fund.

REFERENCES

- [1] Robinet, L., Coupry, C., Eremin, K., Hall, K. Raman investigation of the structural changes during a;teration of historic glasses by organic pollutants, *Journal of Raman Spectroscopy*, 2006; 37:1278-1286.
- [2] Gysels, K., Delalieux, F., Deutsch, F., Van Grieken, R., Camuffo, D., Bernardi, A., Sturaro, G., Busse, HJ., Wieser, M., Indoor environment and conservation in the Royal Museum of Fine Arts, Antwerp, Belgium, *Journal of Cultural Heritage*, 2004, 5: 221-230.
- [3] Prosek, T., Taube, M., Dubois, F., Thierry, D., Application of automated electrical resistance sensors for measurement of corrosion rate of copper, bronze and iron in model indoor atmospheres containing short-chain volatile carboxylic acids, *Corrosion Science*, 2014, 87, 376-382.
- [4] Eggert, G., Corroding glass, corroding metals: survey of joint metal/glass corrosion products on historic objects, *Corrosion Engineering, Science and Technology*, 2010, vol. 45, no 5.
- [5] Greiner-Wronowa, E., Corrosion of Ancient Glasses, *Papers of the Commission on Ceramic Science Polish Ceramic Bulletin*, 2004, vol. 85, 95.

**KERAMICKÉ VRSTVY PRIPRAVENÉ Z ORGANOKREMIČITÝCH
PREKURZOROV PRE PROTİKORÓZNU OCHRANU KOVOV**

**POLYMER DERIVED GLASS CERAMIC LAYERS FOR CORROSION
PROTECTION OF METALS**

M. Parchovianský¹, I. Petříková¹, G. Barroso², G. Motz², D. Galusková¹, D. Galusek¹

¹*Vitrum Laugaricio – Joint Glass Center of the IIC SAS, TnU AD, and FCHT STU,
Študentská 2, 911 50 Trenčín, Slovakia*

²*University of Bayreuth, Ceramic Materials Engineering, D-95440 Bayreuth, Germany*

ABSTRACT

The work was aimed at development of a relatively thick, protective, dense and well adherent coating system on steel. For that purpose, a double layer coating consisting of a polymer derived ceramic (PDC) bond coat, and a PDC top coat with glass and ceramic fillers were prepared. In order to increase the application temperature of the coatings, which is usually limited by the softening temperature of the used glass frit, special aluminosilicate-zirconate glasses ($\text{SiO}_2\text{-Al}_2\text{O}_3\text{-ZrO}_2$) were prepared in the form of microspheres by flame synthesis. The coating thickness was adjusted between 10 and 20 μm . XRD patterns of coating detect two crystalline phases, namely monoclinic and tetragonal ZrO_2 .

Keywords: polymer derived ceramics, glass microspheres, flame synthesis, PDC coatings

INTRODUCTION

Polymer-derived ceramic (PDC) coatings have been intensively studied for many years. The PDC coatings are predominantly based on silicon containing precursors like polysiloxanes, polycarbosilanes or polysilazanes. The PDC processing enables the application of liquid or diluted polymers by simple lacquer methods like dip-coating, spray-coating, or spin-coating as well as by typical ceramic shaping methods like tape-casting, and the transformation to an amorphous ceramic at relatively low temperature [1]. In order to obtain thicker coatings, suitable active or passive fillers have to be added to the pre-ceramic polymer. The incorporation of passive fillers like BN, ZrO_2 can decrease the volume fraction of shrinking while reactive filler particles like ZrSi_2 , TiSi_2 can compensate the shrinkage of pre-ceramics polymer through the expansion during the reaction with the decomposition products [1, 2]. Moreover, the addition of glasses has shown to be a suitable approach to

obtain thick and dense coatings. The glass fillers should be responsible for densification and sealing of the system, increasing the efficiency as environmental barrier coating (EBC) [3, 4].

EXPERIMENTAL

Two commercially available polysilazanes PHPS (perhydropolysilazane) and HTT1800 (both Clariant Advanced Materials GmbH, Germany) were used as precursor materials. The glass microspheres were prepared by combination of a modified Pechini sol-gel method and flame synthesis. Five compositions with different SiO₂-Al₂O₃-ZrO₂ weight ratios were prepared (**Chyba! Nenašiel sa žiaden zdroj odkazov.**). Flat stainless steel (AISI 304) plates were cut into sheets with the dimensions of 4.5 cm × 4.5 cm, ultrasonically cleaned in acetone and dried. The bond coat was prepared from a pre-ceramic polymer precursor (polysilazane PHPS, Clariant Advanced Materials GmbH) that forms a ceramic layer after heat treatment in air. The steel sample substrates were dip-coated with a hoisting apparatus and the coating thickness was adjusted by concentration of the solution and variation of the hoisting speed. Annealing of the bond coated sheets was performed in air at the temperature of 500 °C for 1 h with heating and cooling rates 3 K/min. The top coat was prepared by mixing defined volume fractions of ceramic filler particles (YSZ, ZrSi₂), glass microspheres (SiO₂-Al₂O₃-ZrO₂) of various compositions and a liquid polysilazane HTT1800. The compositions of top coats are listed in the Tab. 2. The pyrolysis of the composite coatings was performed in air (electric oven Nabertherm® LH 60/14, Nabertherm, Germany) at the temperature 1000 °C with the heating and cooling rates of 3 K/min and a holding time of 1 h.

Tab. 1: The compositions of glass microspheres

Compositions	SiO ₂ (wt.%)	Al ₂ O ₃ (wt.%)	ZrO ₂ (wt.%)
SAZ_M_80-10-10	80	10	10
SAZ_M_60-30-10	60	30	10
SAZ_M_50-20-30	50	20	30
SAZ_M_50-30-20	50	30	20
SAZ_M_50-40-10	50	40	10

Tab. 2: The composition of top coats

YSZ (vol. %)	ZrSi ₂ (vol. %)	HTT1800 (vol. %)	Glass (vol. %)
64.8	5.4	26.3	3.4

The amorphous nature of prepared glass microspheres was confirmed by X-ray powder diffraction (Fig. 1). No diffraction peaks indicating the presence of crystalline phases were present. The results of DSC analysis of glass microspheres are shown in the Fig. 2. The glass transition temperature of prepared glasses lies in the interval between 850 and 920 °C, the onset of crystallization temperatures range between 915 and 990 °C, and the temperatures of the maxima of exothermic peaks are in the range from 940 to 1020 °C. The observed differences were attributed to various compositions of studied glasses, especially different contents of silica as the component, which was expected to increase the stability of glasses in terms of their resistance against crystallization.

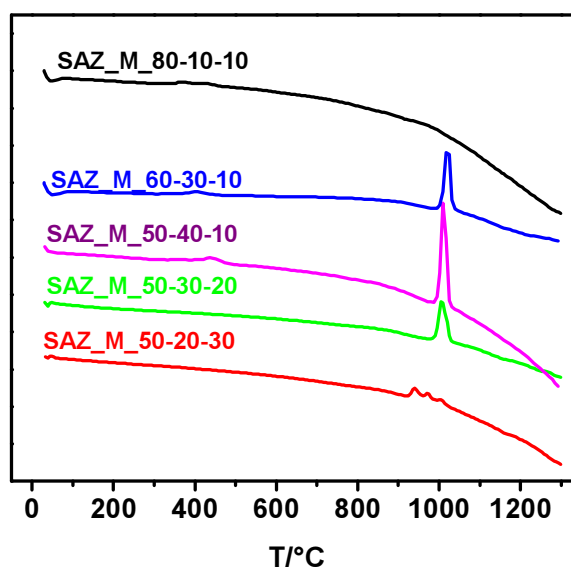
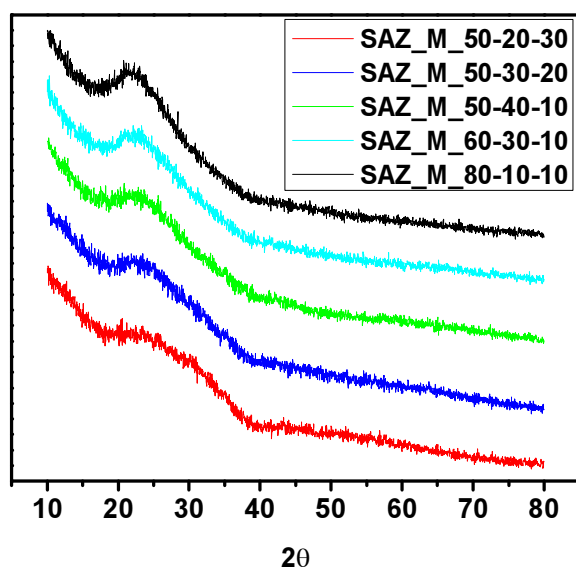


Fig. 1: XRD patterns of the glass microspheres Fig. 2: The results of DSC analysis of glass microspheres

The thickness of the coatings of various compositions is shown in the Fig. 3. The coating thickness was adjusted between 10 and 20 μm . The results of thickness measurements confirm that the combination of PDCs with tailored fillers and glass systems enable the processing of relatively thick coating systems. The phase composition and microstructure of the coatings was also investigated by X-ray diffraction studies and SEM. XRD patterns of coatings are displayed in the Fig. 4. The glass filled polysilazane-based coatings are crystalline after pyrolysis in air at the temperature 1000 °C. For the glass and zirconia filler coatings, two crystalline phases were detected in the coatings, namely monoclinic and cubic ZrO_2 . The phases created by crystallization of glass fillers or the HTT1800-derived phases were below the detection limit of the X-ray diffraction.

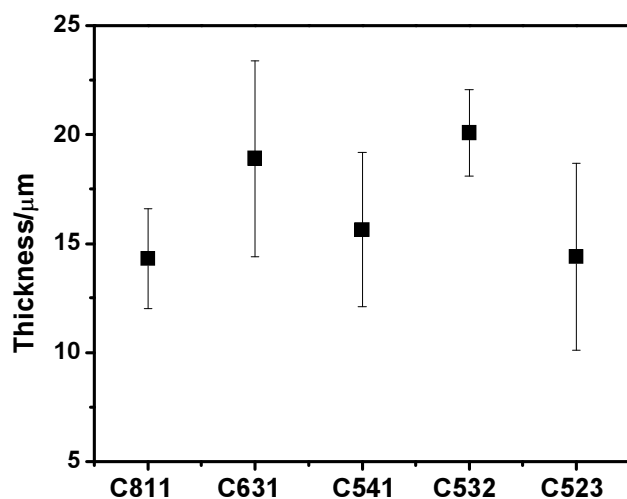


Fig. 3: The average thickness of coatings of various composition

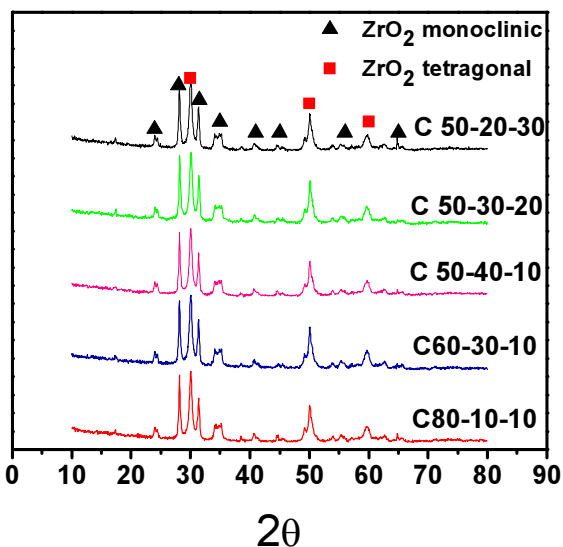


Fig. 4: XRD patterns of the coatings

CONCLUSIONS

The work was aimed at development of a relatively thick, protective, dense and well adherent coating system on steel. For that purpose, a double layer coating consisting of a polymer derived ceramic (PDC) bond coat, and a PDC top coat with glass and ceramic fillers were prepared. In order to increase the application temperature of the coatings, which is usually limited by the glass melting temperature of the used glass frit, special aluminosilicate glasses ($\text{SiO}_2\text{-Al}_2\text{O}_3\text{-ZrO}_2$) with high melting temperature were prepared in the form of microspheres by flame synthesis.

ACKNOWLEDGEMENT

Financial support of this work by the grant VEGA 2/0058/14, and the Alexander von Humboldt Foundation in the frame of the institutional cooperation grant scheme is gratefully acknowledged. This publication was created in the frame of the project "Centre of excellence for ceramics, glass, and silicate materials" ITMS code 262 201 20056, based on the Operational Program Research and Development funded from the European Regional Development Fund.

REFERENCES

1. Colombo, P. et. al. *JACS*, vol. 93, no. 7, pp. 1805–1837, 2010.
2. Torrey, J. D., Bordia, R. K. *JACS*, vol. 91, no. 1, pp. 41–45, 2008.
3. Günthner, M. et. al. *JECS*, vol. 29, no. 10, pp. 2061–2068, 2009.
4. Günthner, M. et. al. *JECS*, vol. 31, no. 15, pp. 3003–3010, 2011.

**VPLYV TEPELNÉHO SPRACOVANIA Ce^{3+} DOPOVANÝCH SKIEL NA
LUMONISCENČNÉ VLASTNOSTI V SYSTÉME $Y_2O_3-Al_2O_3$**

**THE EFFECT OF THERMAL TREATMENT OF Ce^{3+} DOPED GLASS ON
LUMINESCENCE PROPERTIES IN THE SYSTEM $Y_2O_3-Al_2O_3$**

K. Haladejová, R. Klement, A. Prnová, D. Galusek

Vitrum Laugaricio – Joint Glass Centre of the IIC SAS, TnU AD and FChPT STU, Trenčín

ABSTRACT

The Ce^{3+} doped glass with composition of 76.67 mol.% (~60 wt.%) Al_2O_3 , 23.08 mol.% (~40 wt.%) Y_2O_3 and 0.25 mol.% Ce_2O_3 was prepared by flame-straying technique. On the basis of thermal properties studied by DSC, the glass was heat-treated and the effect of the thermal treatment on luminescence intensity was studied in detail.

Keywords: Photoluminescence, Ce^{3+} doped glass, yttrium aluminate glasses, LED, phosphor

INTRODUCTION

Yttrium aluminium garnet ($Y_3Al_5O_{12}$, YAG) has been recognized as one of the best phosphor host materials for rare earth ions because of its optical transparency in the wavelength range from ultraviolet to infrared [1]. The Y^{3+} and Al^{3+} ions can be, to a certain extent, substituted by many kinds of cations with different sizes and valence [2]. When substituted with a few percent of the activator ion Ce^{3+} , $Y_3Al_5O_{12}$ is a luminescent material that has nearly ideal photoluminescence properties for excitation by a blue solid-state light source; YAG:Ce is therefore a phosphor with high quantum efficiency, excellent chemical and thermal stability, high mechanical strength and excellent optical properties [3]. Hence, developing a simple and reliable synthetic method for phosphor particles with controlled morphology and structure is still a task of particular importance. One of the possible methods involves preparation of the polycrystalline material from glass by controlled crystallization.

EXPERIMENTAL

The obtained glass microspheres with composition Y40A60Ce0.5 were first examined by optical microscopy and SEM. Closer inspection by SEM shows regular features (faces) at the surface of some microspheres indicating that some of them were at least partially crystalline. The glass microspheres were found to be XRD amorphous.

The thermal properties of the sample Y40A60Ce0.5 were examined by DSC analysis. The DSC record of the glasses microbeads is shown in Fig. 1; two crystallization effects were observed. The glass transition temperature (T_g), onset of crystallization temperature (T_{x1} , T_{x2}), and the temperature at maxima of the exothermic crystallization peaks (T_{p1} , T_{p2}) were estimated from the DSC curve. The T_g of studied glass (endothermic effect) was found to be in the range 875 – 901 °C (875 °C onset, 893 °C inflection and 901 °C end of the endothermic effect). The characteristics of exothermic effects corresponding to crystallization of the sample Y40A60Ce0.5 are: $T_{x1} = 923$ °C, $T_{p1} = 936$ °C, $T_{x2} = 989$ °C and $T_{p2} = 1000$ °C, respectively.

The time-temperature regime for heat treatment of the sample Y40A60Ce0.5 was selected on the basis of the nucleation and crystallization experiments performed on STA instrumentation. The selected temperatures are depicted as points on Fig. 1, the dwell time for heat treatment at each temperature was 3h. The phase composition of the sample after heat treatment was examined by XRD. The powder diffraction traces revealed that up to 1200 °C the major phase is YAG. The second phase, α -Al₂O₃, was only reliably observed in the XRD of sample treated at 1500 °C for 5 h.

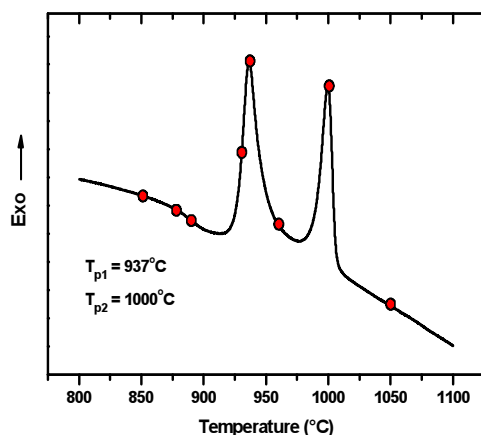


Fig. 1: DSC trace of as prepared microspheres in the system Y40A60Ce0.5

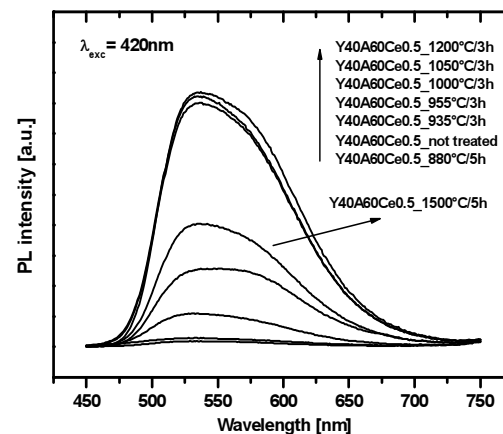


Fig. 2: PL emission spectra of crystallized glass microspheres in the system Y40A60Ce0.5. The spectra shown in order of increasing temperature.

The luminescence spectra of glass microspheres and of the heat-treated samples are shown in Fig. 2. The emission spectra consist of a peak centred at 535 nm and a shoulder at longer wavelength side ~575 nm, which can be attributed to electronic transitions of the Ce^{3+} . The former is assigned to the $5d^1 - ^2F_{5/2}$ transition and the latter to the $5d^1 - ^2F_{7/2}$ transition, respectively. The emission (PL) intensity increases with the heat-treatment temperature of the samples reaching the maximum for the sample treated at 1200 °C.

CONCLUSION

The Ce^{3+} doped glass Y40A60Ce0.5 was successfully prepared by flame-straying technique. The thermal properties were studied by DSC technique and characteristic temperatures have been estimated for two exothermic effects observed on DSC trace. On the basis of thermal properties, the glass was heat-treated at several temperatures for 3h. The emission (PL) intensity has been found to increase with the heat-treatment temperature of the samples reaching the maximum for the sample treated at 1200 °C. This effect is most likely due to the higher packing densities of Ce^{3+} ions in the crystallites than in glass.

ACKNOWLEDGEMENTS

The financial support of this work by the projects SAS-NSC JRP 2012/14 and VEGA 1/0631/14, is gratefully acknowledged. This publication was created in the frame of the project "Centre of excellence for ceramics, glass, and silicate materials" ITMS code 262 201 20056, based on the Operational Program Research and Development funded from the European Regional Development Fund.

REFERENCES

- [1] Zhou X, Zhou K., Li Y., Wang Zh., Feng Q., J. Lumin. 132 (2012) 3004.
- [2] Mu Zh., Hu Y., Wu H., Fu Ch., Kang F., J. Alloy Compd. 509 (2011) 6476.
- [3] Liang Y, Yu D., Zhu Huang W., Zhang M., Li G., Yan Ch, Mat. Sci. Semicon. Proc. 30 (2015) 92.

FOTOLUMINISCENTY NA BÁZE WILLEMITU.

Morfológia zrn a fluorescenčné spektrá pri použití rôznych aktivátorov luminiscencie.

WILLEMITE BASED PHOTO LUMINESCENT MATERIALS.

Grain morphology and florescent spectra by using different activators of luminescence.

P. Švančárek, R. Klement, L. Dvorská, D. Galusek

Vitrum Laugaricio – Joint Glass Centre of the IIC SAS, TnU AD and FChPT STU, Trenčín,
Slovakia

e-mail: peter.svancarek@tmuni.sk

ABSTRACT

In this work we observed grain morphology and spectra of Eu^{3+} doped Zn_2SiO_4 . Because Eu^{3+} is a trivalent cation it is not interchangeable with divalent Zn^{2+} ions easily. To deal with this problem, the same atomic percent of Li^+ cations was added for charge compensation. We compared morphology and fluorescent properties of four different samples - manganese doped and europium doped willemite phosphors as well as both of those phosphors co-doped by Li^+ . Li^+ addition to both Mn^{2+} and Eu^{3+} doped phosphors leads into more extensive formation of willemite phase during high temperature solid state reaction. Luminescence properties changed differently: Mn^{2+} doped willemite co-doped by Li^+ lost intensity of phosphorescence to about half of what Li^+ free specimen exhibits, Mn^{2+} doped willemite co-doped by Li^+ increased luminescence intensity about 2.5 times when compared with Li^+ free sample.

Keywords: willemite, Mn^{2+} , Eu^{3+} , green/orange-red luminescence, charge compensation

INTRODUCTION

Zinc silicate (Zn_2SiO_4) has a long history as phosphor host matrix. High efficiency of light sources depends on high quantum efficiency of the phosphor. Willemite based manganese doped phosphor ($\text{Zn}_2\text{SiO}_4:\text{Mn}^{2+}$) is used due to its properties for longer than 180 years. Its chemical and thermal stability plays also important role why this phosphor is often selected as a phosphor of choice. X-Ray, UV light or electron irradiation are used as energy carriers to charge willemite crystal lattice, and Mn^{2+} ions, which are incorporated into the lattice as a

substitute for small fraction of Zn^{2+} ions are used as photoluminescence activator for the green phosphor. They are widely used in plasma display panels, cathode ray tubes, oscilloscopes and fluorescent lamps [i, ii].

Mn^{2+} dopant is most used because it enables very strong emission in green part of spectra (523 nm). Other dopants have been used to enable different part of spectra; to obtain fluorescence in the blue spectral region, for example Ti^{3+} and/or Ti^{4+} activator was used [iii]. Cold white emission was observed when Eu^{3+} co-dopant was used in the system $\text{Zn}_2\text{SiO}_4:\text{Mn}^{2+}$. Eu^{3+} enables orange (583 nm) and red (615 nm) emission while leftover of ZnO enables emission at 400 nm (ZnO defects emission under 266 nm excitation). This phosphor has color coordinates similar to those of a white color fluorescent lamp (~5000 K) [iv].

In this work we tried to determine, whether a charge compensation of Eu^{3+} by Li^+ will allow greater incorporation of active atom into willemite lattice. This should result into higher intensity of luminescence of willemite co-doped by Eu^{3+} and Li^+ when compared with Eu^{3+} only doped willemite.

EXPERIMENTAL

The SiO_2 , ZnO , Li_2CO_3 and $\text{MnO}_2/\text{Eu}_2\text{O}_3$ chemicals of analytical grade or higher purity were weighed to obtain mixtures of powders with compositions corresponding to $\text{Zn}_{0.97}\text{Eu}_{0.03}\text{SiO}_3$, $\text{Zn}_{0.94}\text{Eu}_{0.03}\text{Li}_{0.03}\text{SiO}_3$, $\text{Zn}_{0.97}\text{Mn}_{0.03}\text{SiO}_3$ and $\text{Zn}_{0.94}\text{Mn}_{0.03}\text{Li}_{0.03}\text{SiO}_3$, respectively. Fine powders were prepared by ball milling and homogenization of powder mixtures in vibratory mill for 30 minutes. Obtained mixture of fine powders was calcined for 2 h at 1300 °C in air. For the SEM/EDX analysis (JEOL JSM-7600 Thermal FE SEM) the powders were cast into phenolic conductive resin and polished by diamond polishing disc and examined with a HR-SEM JEOL 7600f. Both emission and excitation fluorescence spectra were measured by Fluorolog 3 (FL3-21, Horiba) fluorescence spectrometer in front-face mode. The Xe-lamp (450 W) was used as an excitation source. The phase composition was determined using powder X-ray diffraction (PANalytical Empyrean Series 2 X-ray diffractometer).

RESULTS

SEM has shown significant differences in morphology of the calcined powder products. Lithium/free samples contain grains with dark un-reacted core with high silica content and lighter shell with higher zinc content and comprising the willemite phase (**Fig 1.A.**). However, addition of lithium changed the situation. Not only the shell expanded in volume,

but lighter crystals were present also in the core (**Fig. 1. A. vs B.**). This suggests the Li^+ ions promoted diffusion of Zn^{2+} and other ions into the SiO_2 particles. SEM-EDX mapping and point analysis revealed that for Mn^{2+} -containing phosphors, the distribution of Mn^{2+} ions in the samples is more homogeneous than in the case of Eu^{3+} doped samples (**Fig. 1. C. and D.**); the aggregates containing relatively high concentration of Eu^{3+} (up to 15 at. %) were observed in both europium containing specimens. It is well known that Mn^{2+} ions effectively substitute Zn^{2+} ions in the willemite structure due to the similarity of their ionic radii. The X-ray powder diffraction patterns of all four studied systems showed the presence of willemite (Zn_2SiO_4) as a major crystalline phase, together with traces of unreacted SiO_2 (cristobalite). The XRD patterns corresponding to Li^+ undoped and co-doped analogues are almost identical and no lithium containing phases were identified.

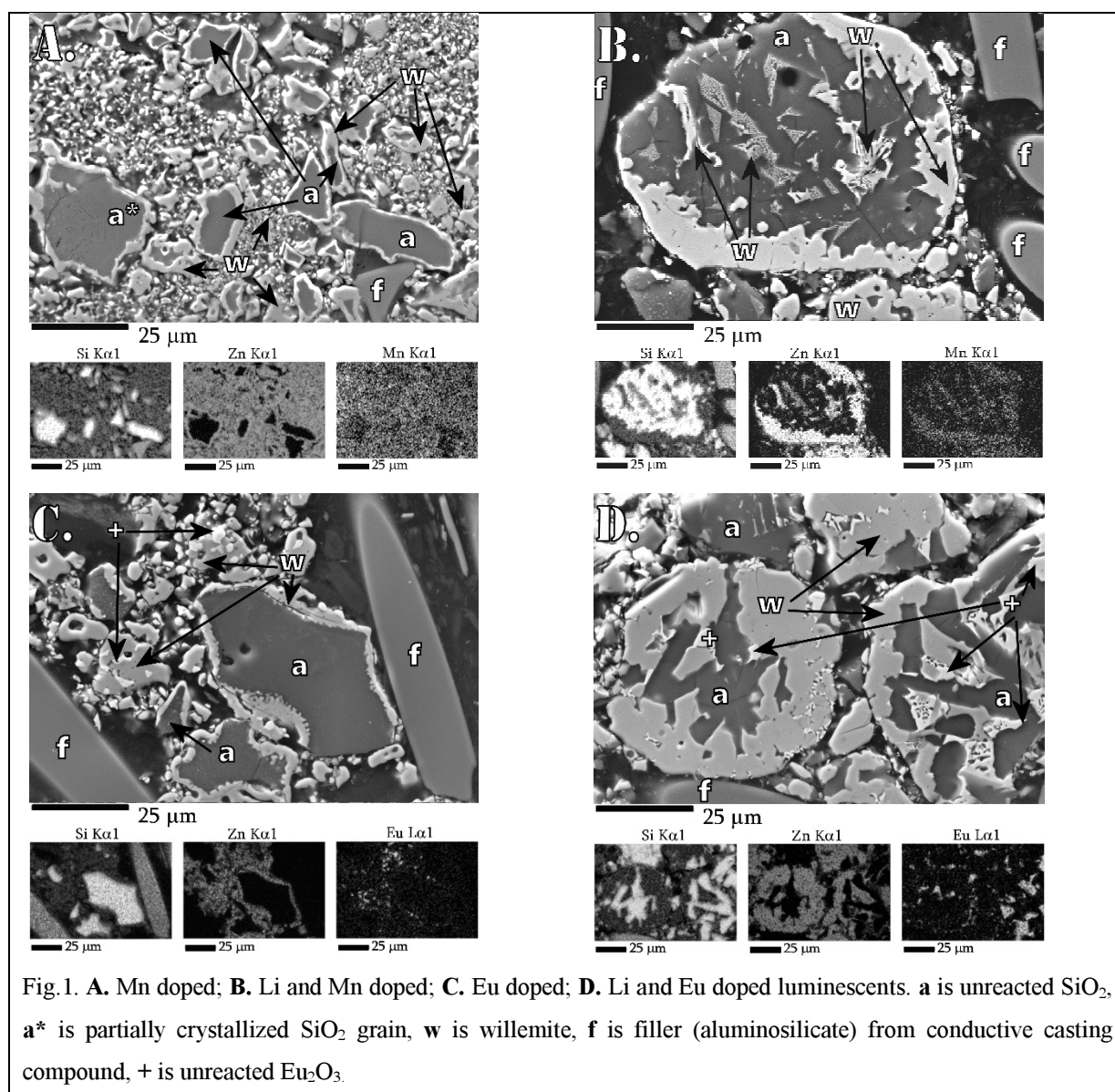


Fig.1. **A.** Mn doped; **B.** Li and Mn doped; **C.** Eu doped; **D.** Li and Eu doped luminescents. **a** is unreacted SiO_2 , **a*** is partially crystallized SiO_2 grain, **w** is willemite, **f** is filler (aluminosilicate) from conductive casting compound, **+** is unreacted Eu_2O_3 .

The photoluminescence emission spectra are shown in **Fig. 2**. Mn^{2+} doped willemite (**Fig. 2A**) exhibits strong green emission centered at 523 nm when excited at 277 nm, corresponding to the d-level spin-forbidden transition of Mn^{2+} ion (${}^4\text{T}_{1g} - {}^6\text{A}_{1g}$). Co-doping with Li^+ ions decreases the intensity of green emission to less than half, when compared to the Li^+ -free analogue, $\text{Zn}_{0.97}\text{Mn}_{0.03}\text{SiO}_3$. The excitation spectra (not shown, emission monitored at 613 nm) of Eu^{3+} doped systems $\text{Zn}_{0.97}\text{Eu}_{0.03}\text{SiO}_3$ and $\text{Zn}_{0.94}\text{Eu}_{0.03}\text{Li}_{0.03}\text{SiO}_3$ exhibit, instead of broad charge transfer band (CTB), some narrow excitation peaks originated from the f-f transitions within the $\text{Eu}^{3+} 4f^6$ configuration. The most efficient excitation peak is the one originated from ${}^7\text{F}_0 \rightarrow {}^5\text{L}_6$ transition (~ 394 nm), which means that this phosphor can be effectively excited by UV LED chip. Emission spectra exhibited five major emission lines centered at app. 578, 590, 617, 650 and 700 nm corresponding to the ${}^5\text{D}_0 \rightarrow {}^7\text{F}_J$ ($J = 0, 1, 2, 3, 4$) transitions, respectively (Fig. 2B).

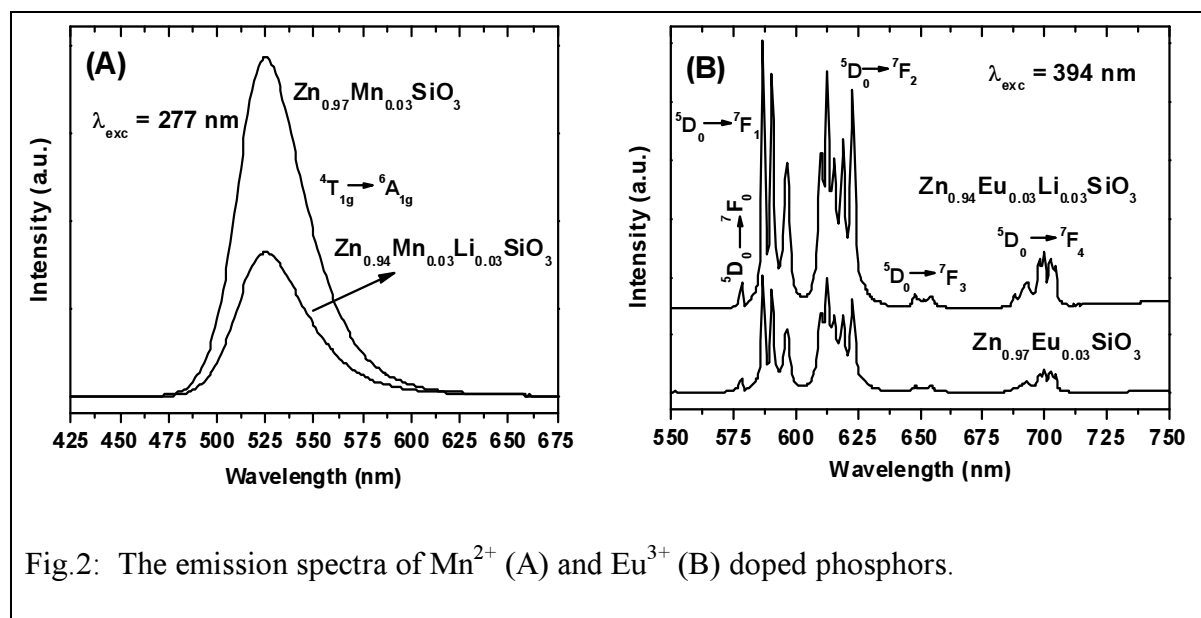


Fig.2: The emission spectra of Mn^{2+} (A) and Eu^{3+} (B) doped phosphors.

It is common knowledge that ${}^5\text{D}_0 \rightarrow {}^7\text{F}_{0,1}$ transition is directed by selection rules for intermediate magnetic-dipole coupling $\Delta J = 0, \pm 1$, and the ${}^5\text{D}_0 \rightarrow {}^7\text{F}_{2,4,6}$ are allowed electronic-dipole transitions [v]. Generally, when the Eu^{3+} ion occupies the crystallographic site with inversion symmetry, its magnetic-dipole transition ${}^5\text{D}_0 \rightarrow {}^7\text{F}_1$ orange emission dominates in the emission spectrum, while the electric-dipole transitions ${}^5\text{D}_0 \rightarrow {}^7\text{F}_{2,4}$ red emission is dominant if the Eu^{3+} ion is located at a non-inversion center. Based on such general presumptions, Eu^{3+} ions most likely occupy both inversion and non-inversion lattice sites in the studied $\text{Zn}_{0.97}\text{Eu}_{0.03}\text{SiO}_3$ and $\text{Zn}_{0.94}\text{Eu}_{0.03}\text{Li}_{0.03}\text{SiO}_3$ systems. Very well resolved splitting of ${}^5\text{D}_0 \rightarrow {}^7\text{F}_{1,2}$ transitions to three and five lines is observed due to the Stark splitting in the strong crystal field which also indicates that the symmetry at Eu^{3+} ion site is low.

CONCLUSIONS

The opposite effect of Li^+ co-doping on PL emission intensity in Mn^{2+} and Eu^{3+} doped systems can be explained by the formation of vacancies when substituting Zn^{2+} ions by the $\text{Mn}^{2+}/\text{Eu}^{3+}/\text{Li}^+$ ions. The formation of vacancies is not favorable for the emission PL activator ($\text{Mn}^{2+}/\text{Eu}^{3+}$) because the energy transfer from activator to vacancy is more efficient, and hence a certain amount of vacancies will negatively affect the photoluminescence intensity.

1. The co-doping of $\text{Zn}_{0.97}\text{Mn}_{0.03}\text{SiO}_3$ with Li^+ ions leads to significant decrease of emission intensities by the factor of ~ 2 . Lithium ion increases number of vacant positions making willemite crystal lattice less ordered. Additionally, the strong polarization effect of Li^+ ion may also affect the close coordination environment around the Mn^{2+} and structure of the host matrix.

2. The co-doping of $\text{Zn}_{0.97}\text{Eu}_{0.03}\text{SiO}_3$ with Li^+ ions leads to significant increase of emission intensities by the factor of ~ 2.5 . In this case, Li^+ ions are effectively decreasing the number of Zn vacancies (charge compensation effect)

ACKNOWLEDGEMENTS

The financial support of this work by the projects SAS-NSC JRP 2012/14 and VEGA 1/0631/14, is gratefully acknowledged. This publication was created in the frame of the project "Centre of excellence for ceramics, glass, and silicate materials" ITMS code 262 201 20056, based on the Operational Program Research and Development funded from the European Regional Development Fund.

LITERATURE

[ⁱ] Hao, Y., Wang, Y. Luminescent properties of $\text{Zn}_2\text{SiO}_4:\text{Mn}^{2+}$ phosphors under UV, VUV and CR excitation, *Journal of luminescence* 122-123 (2007) 1006-1008.

[ⁱⁱ] Cho, T. H., Chang, H. J. Preparation and characterizations of $\text{Zn}_2\text{SiO}_4:\text{Mn}$ green phosphors, *Ceram. Int.* 29 (2003) 611

[ⁱⁱⁱ] Tsai, M. T., Lu, F. H., Wu, J. M., Wang, Y. K., Lin, J. Y. Photoluminescence of Titanium-Doped Zinc Orthosilicate Phosphor Gel Films, 2011 IOP Conf. Ser.: Mater. Sci. Eng. 18 (2011) 032012

[^{iv}] Ramakrishna, P. V., Murthy, D. B. R. K., Sastry, D. L. White-light emitting Eu^{3+} co-doped $\text{ZnO}/\text{Zn}_2\text{SiO}_4:\text{Mn}^{2+}$ composite microphosphor, *Spectrochimica Acta Part A: Molecular and Biomolecular Spectroscopy* 125 (2014) 234–238

[^v] Binnemans, K. Interpretation of europium(III) spectra, *Coordination Chemistry Reviews* 295 (2015) 1–45

KINETIKA KRYŠTALIZÁCIE ALUMINA – YTRITÉHO GRANÁTU

CRYSTALLIZATION KINETICS OF YTRIUM ALLUMINIUM GARNET

J. Chovanec ¹, A. Černá ¹, J. Kraxner ¹, R. Svoboda ², D. Galusek ¹, A. Prnová ¹

¹*Vitrum Laugaricio – Joint Glass Center of the IIC SAS, TnU AD, and FChPT STU, Trenčín, Slovakia*

²*Department of Physical Chemistry, Faculty of Chemical Technology, University of Pardubice, Studentska 573, Pardubice 532 10, Czech Republic*

ABSTRACT

Differential scanning calorimetry (DSC) analysis were used to study crystallization in yttrium aluminium garnet glass under non-isothermal conditions. The crystallization kinetics was described in terms of the autocatalytic Šesták–Berggren model. An extensive discussion of all aspects of a full-scale kinetic study of a crystallization process was undertaken. The activation energy of crystallization according OZAWA was found 861 ± 15.7 KJ/mol.

Keywords: crystallization kinetics, DSC, autocatalytic Šesták - Berggren model

INTRODUCTION

Yttrium aluminum garnet (Y₃Al₅O₁₂; YAG) is very important ceramics material which is used in many applications. It is also used in optical applications such as laser materials (e.g., when doped with rare-earth cations, such as neodymium) ^{1,2}. Its low creep coupled with its very high melting temperature (1940 °C) make it particularly attractive for structural applications ⁴⁻⁶.

Crystallization process and its kinetics can be studied on various physical properties by numerous experimental techniques. Nevertheless, generally one of the two main approaches is always being applied. Either a macroscopic method, or differential thermal analysis (DTA) and differential scanning calorimetry (DSC) belong to the most commonly used techniques. Both these methods allow registering of basically every process during which enthalpy change occurs. Thorough description of these methods can be found in ⁷. Very good explanation of interpretation of crystallization kinetics can be found in ⁸.

EXPERIMENTAL PART

The crystalline yttrium garnet was prepared by Pechini method. We used flame synthesis for preparation of glasses yttrium garnet.

Crystallization behavior of the prepared glass was studied using Netzsch STA 449 F1 Jupiter TG/DTA/DSC equipped with cooling accessory (in DSC mode). Dry nitrogen was used as a purge gas. The applied heating rates were as follows: 2, 5, 10, 15, 20, 25, 30 K/min. Acquisition of the DSC crystallization peaks data was achieved by using the cubic spline interpolation of the DSC thermokinetic background.

The evaluation of crystallization kinetics usually starts with determination of the activation energy E . For this reason, the Ozawa method is frequently applied. This method requires three or more experiments at different heating rates. The activation energy of crystallization according to Ozawa was found 861 ± 15.7 KJ/mol.

The experimental data which were obtained by DSC can be described according to the following equation:

$$\theta = \Delta H \cdot A \cdot e^{-\frac{E}{RT}} \cdot f(\alpha),$$

where θ is the measured heat flow, ΔH is the crystallization enthalpy, A is the pre-exponential factor, E is the apparent activation energy of the process, R is the universal gas constant, T is temperature and $f(\alpha)$ stands for an expression of a kinetic model with α being conversion. In our case the semi – empirical autocatalytic model Šesták – Berggren (AC) by the following equation:

$$f(\alpha) = \alpha^M (1 - \alpha)^N,$$

where M and N are empirical parameters corresponding to the curvature of the respective edges of the crystallization peak. The semi-empirical nature of this model results in its high flexibility, and thus very good quality of the description was achieved (the crystallization data for the studied of YAG fitted by this model are shown in the Fig. 1). The model itself or its parameters do not have any physical basis or meaning, the description is purely phenomenological. Our data which were fitted by AC model assumed that there are two independent processes (the system contains two partially dependent processes, in fact). Therefore the interpretation of this data is not easy. In order to obtain a realistic view of

crystallization processes, it is important to measure high temperature RTG diffraction (non – isothermal and isothermal processes).

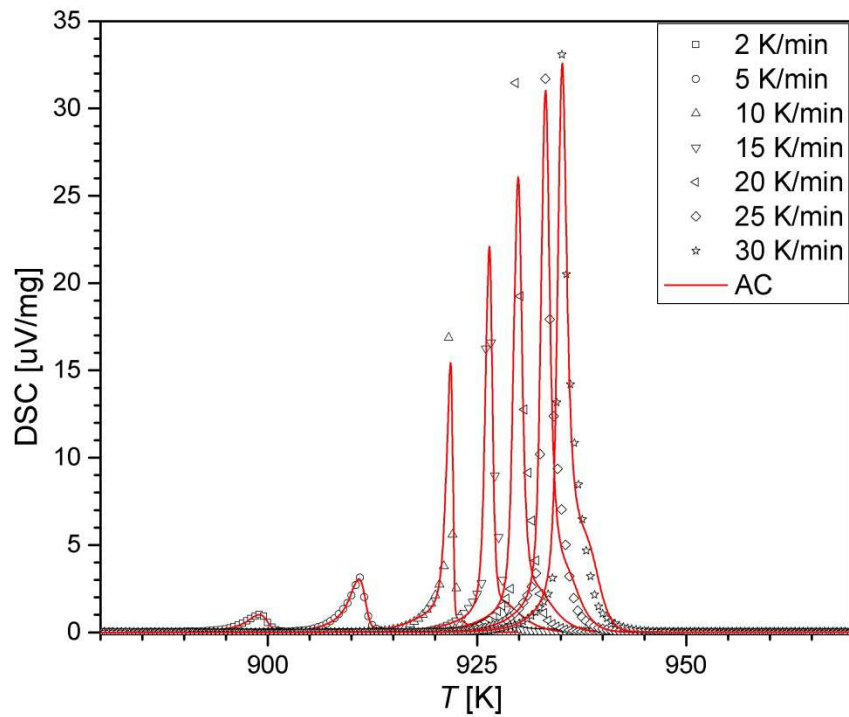


Fig. 1: Experimental crystallization DSC curves fitted by AC model.

In the Table 1, we can see the parameters for two independent processes (two peaks, which were obtained by deconvolution). The parameters such as pre-exponentially factor $\log A$, activation energy E_a and independent reaction have very similar values (for different heating rate) for both peaks. The parameters (mainly parameters m , n) of second peak are very similar too. The parameters n and m in first peak have very different values if the heating rate is changed.

Table 1: Parameters obtained by fitting experimental data using AC model for two independent processes.

Heating rate K/min	$\log A$	E KJ/mol	n	m	$\log A$	E KJ/mol	n	m	Independent reaction
2	36.94	861	0.712	1.068	36.61	861	0.99	0.89	0.60
5	37.07	861	0.745	1.120	36.67	861	0.95	0.925	0.58
10	37.50	861	0.741	1.285	36.60	861	0.94	0.91	0.60
15	37.78	861	1.24	1.37	36.48	861	0.87	0.95	0.54
20	37.80	861	1.51	1.37	36.49	861	0.95	0.87	0.54
25	37.84	861	1.79	1.38	36.55	861	0.94	0.91	0.56
30	37.85	861	1.95	1.38	36.62	861	0.89	0.94	0.53

CONCLUSIONS

Crystallization kinetics of the yttrium aluminium garnet glass was studied under non-isothermal conditions by using differential scanning calorimetry. The complete kinetics analysis was performed in terms of the Šesták – Bergger models. We have discovered that this model is useful for description of YAG glasses, which contain two independent kinetics processes.

REFERENCES

- [1] Corman, G. S. J., Mater. Sci. Lett. 12, (1993), 379.
- [2] Karato, S., Wang, X., Fujino, K., J. Mater. Sci. 29, (1994), 6458.
- [3] Caslavsky, J.L., Viechnicki, D.J. J., Mater. Sci. 15, (1980), 1709.
- [4] Weber, J.K.R., Cho, B., Hixson, A.D., Abadie, J.G., Nordine, P.C., Kriven, W.M., Johnson, B.R., Zhu, D., J. Eur. Cer. Soc. 19, (1999), 2543.
- [5] Doleman, P.A., Butler, E.G., Key Eng. Mater., 193 (1997), 127–131.
- [6] King, B.H., Halloran, J.W., J. Am. Ceram. Soc. 78, (1995), 2141.
- [7] Šesták, J., Science of Heat and Thermophysical Studies: A Generalized Approach to thermal Analysis, Elsevier, Amsterdam, 2005
- [8] Svoboda, R., Málek, J., Thermochim. Acta, 526, (2011), 237 – 251.

**DIAGNOSTIKA PLAZMOVO UPRAVENÉHO KORUNDOVÉHO PRÁŠKU
POMOCOU TEPELNE STIMULOVANEJ LUMINISCENCIE**

**USE OF THERMALLY STIMULATED LUMINESCENCE FOR DIAGNOSTIC OF
PLASMA TREATED ALUMINA POWDER**

T. Morávek, J. Ráhel

*Masaryk University, Faculty of Science, Department of Physical Electronics, Kotlářská 2,
Brno, Czech Republic*

ABSTRACT

Chemiluminescence of dielectric barrier discharge treated alumina powders could be used with advantage as an effective diagnostic method for determining the efficiency and aging of plasma treatment. However the deflection of detected signal from theoretical prediction suggests that other radiation mechanisms are participating on overall luminescence signal. Presented series of complementary experiments confirmed, that indeed chemiluminescence is the main process behind the observed light emission. Further radiation process associated with plasma treatment was identified as recombination-induced luminescence.

Keywords: chemiluminescence, DCSBD, plasma

INTRODUCTION

Chemiluminescence accompanies certain types of exothermic chemical reactions, usually of oxidative nature. It is commonly used for the detection of traces of hydrogen peroxide [1] and monitoring the oxidation stability of polymers [2,3,4]. The measurements of chemiluminescence (CL) typically consists of heating the substrate (isothermally or with steadily increasing temperature) followed by the detection of spectrally unresolved light. This is presumably emitted from the substrate due to the oxidation processes involving the hydroperoxides decay [5,6]. In our experiments we investigated the luminescence of sub-micron alumina powder treated in low-temperature coplanar dielectric barrier discharge [7]. The process of chemiluminescence associated with the presence of hydroperoxides on the powder surface was intended to be used as an indicator of the plasma treatment. A method capable of rapid assessment of plasma treatment for powders was sought, since the conventional methods based on sessile drop measurements are not well suited for particulate

materials, and capillary rise Washburn method [8], requires at least several grams of powder for a single measurement. This can be a major drawback when dealing with expensive powders, or when plasma treats at very slow rate due to its limited size or extremely large surface area of powders. On the other hand only tens of milligrams of powder are needed for the measurement of chemiluminescence. However as stated above the detected luminescence signal may comprise emission by other radiative processes besides CL. This paper presents our attempt to resolve the individual luminescence processes introduced to powder surface by dielectric barrier discharge plasma treatment.

EXPERIMENTAL

Plasma source

DCSBD (Diffuse Coplanar Surface Barrier Discharge) non-thermal plasma generator (Fig. 1) was used. It consisted of a screen-printed array of coplanar strip-like electrodes on the bottom side of a 96% purity Al₂O₃ plate with the thickness of 0.6 mm. 1.5 mm wide electrodes were separated by 1 mm gaps. The active plasma area of DCSBD unit was 8×20 cm². The electrode was cooled by circulating transformer oil, which also provides an additional electrical insulation. The system was powered by 14 kHz sinusoidal high-voltage of up to 20 kV peak-to-peak amplitude. By increasing the driving voltage, a thin layer (about 0.3 mm) of low temperature non-equilibrium plasma consisting of H-shaped microdischarges emerges on the upper surface of the ceramic plate [7].

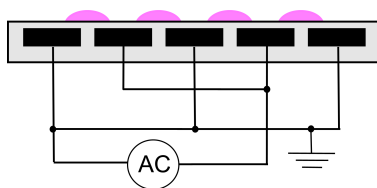


Fig. 1 - Schematics of DCSBD setup. Only a reduced number of electrodes is shown for the sake of clarity.

Material

Plasma treatment was carried out on the sub-micron alumina powder Taimicron TM-DAR (Taimei Chemicals Co.,Ltd., 99.995% purity) with surface area of 13.7 m²/g and primary particle size of 150 nm. Prior to the treatment, a small amount (approximately 1 g) of alumina powder was poured through a sieve on the surface of discharge ceramics (plasma area). The

thin powder layer was covered with the shield glass plate. Alumina powder was treated in DCSBD operating in atmospheric pressure ambient air at input power of 400W for 1 minute.

Measurement

Luminescence experiments were performed on the photon-counting instrument Lumipol 3 manufactured by the Polymer Institute of Slovak Academy of Sciences, Bratislava, Slovakia. The measurements were done in a nitrogen flow of 25 mL/min. The weight of each sample was 80.0 ± 0.5 mg. The instrument dark count rate was 1-5 counts/s at 50 °C, spectral range of instrument was 290-630 nm.

RESULTS

The shape of luminescence curve on Figure 2 clearly shows that indeed multiple processes are involved. Before the maximum is reached a shoulder appears, the origin of which had to be identified.

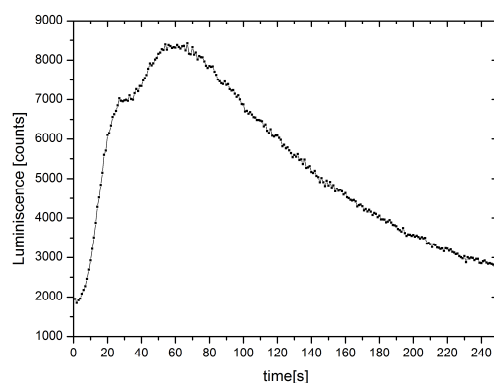


Fig. 2 - Luminescence signal detected from plasma treated alumina powder (thermally cleaned at 600°C for 1 hour) in isothermal mode at 50°C.

Plasma treated alumina powders were left to age for a certain amount of time at ambient air, before investigated by chemiluminometer set to 120°C isothermal mode. The resulting curves are shown on Figure 3. It can be seen that as the peroxides (introduced to the surface by plasma treatment) decay during the aging process, the maximum of the curve decreases as well. Hence the dominant process present during the maximum can be assigned to the chemiluminescence, which is in good agreement with [9]. One can see, however, that even after 29 hours since plasma treatment, the effect of surface activation is still present.

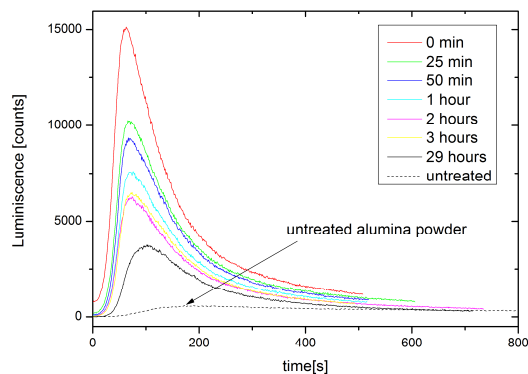


Fig. 3 - Luminescence signal detected from plasma treated alumina powder in isothermal mode at 120°C for aging times 0 - 29 hours.

CONCLUSION

Luminescence measurements were performed on alumina powders treated by DCSBD. These measurements provide a valuable option for evaluation of plasma treatment of morphologically complex materials. From the set of performed experiments it appears that the main processes contributing to the overall luminescence is the chemiluminescence, whereas the recombination induced luminescence starts to dominate in the later phases of the isothermal measurements.

ACKNOWLEDGEMENT

This work was supported in part by the Czech Science Foundation, Contract No. GA13-24635S, by project LO1411 (NPU I) funded by Ministry of Education Youth and Sports of Czech Republic and project “CEPLANT - R&D center for low-cost plasma and nanotechnology surface modifications” (Grant No. CZ.1.05/2.1.00/03.0086) funded by European Regional Development Fund.

REFERENCES

- [1] Campbell, A., Kricka, L., Stanley, P. Bioluminescence and chemiluminescence, fundamentals and applied aspects. Chichester: John Wiley & Sons, (1994).
- [2] Cerruti, P., Carfagnaa, C., Rychlý, J., Matisová -Rychlá, L. Polymer Degradation and Stability, 82, 477–485, (2003).
- [3] Cerruti, P., Malinconico, M., Rychly, J., Matisova-Rychla, L., Carfagna, C. Polymer Degradation and Stability 94, 2095–2100, (2009).
- [4] Camacho, W., Karlsson, S. Polymer Degradation and Stability, 78, 385–391, (2002).

- [5] Matisova-Rychla, L., Rychly, J., Vavreková, M. *European Polymer Journal*, Volume 14, Issue 12, 1033–1037, (1978).
- [6] Zlatkevich, L. *Luminescence technique in solid state polymer research*, New York, ISBN: 978-0824780456,93, (1989).
- [7] Šimor et al., *Applied Physics Letters*, 81, 2716 (2002).
- [8] Morávek, T. et al., *Open Chem.*, 13, 236-244, (2015).
- [9] Duran, M., Massines, F., Teysse, G., Laurent, Ch. *Surface and Coatings Technology*, 142-144, 743-747, (2001).

METÓDY PRÍPRAVY KREMIČITANOVÝCH LUMINOFOROV DOPOVANÝCH Ce/Mn A ICH VPLYV NA LUMINISCENČNÉ VLASTNOSTI

VARIOUS SYNTHESIS ROUTES FOR PREPARATION OF CE-MN-DOPED SILICATE PHOSPHORS AND THEIR INFLUENCE ON LUMINESCENCE

P. Veteška¹, D. Galusek¹, S. H. Lin², S. J. Shih², C. T. Yeh³, W. H. Tuan³

¹*FCHPT STU, Radlinského 9, 812 37 Bratislava, Slovak Republic,*

²*Department of Materials Science and Engineering, NTUST, #No.43, Sec. 4, Keelung Rd.,
Da'an Dist., Taipei City 106, Taiwan*

³*Department of Materials Science and Engineering, NTU, No.1, Sec.4, Roosevelt Rd., Taipei
10617, Taiwan*

ABSTRACT

In this work we study the influence of preparation route on the phase composition and luminescence properties of manganese-cerium-codoped luminescence materials with the Åkermanite-based matrix with nominal composition $\text{Ca}_{(1-x)}\text{Sr}_x\text{MgSi}_2\text{O}_7$ ($x=0; 1$) using $\text{Ce}^{3+}/\text{Mn}^{2+}$ as optically active doping agents. The methods for the synthesis of samples include the solid state synthesis, the sol-gel synthesis and the spray pyrolysis. The best results were obtained for strontium-based system prepared by spray pyrolysis method.

Keywords: luminescence, sol-gel, spray pyrolysis

INTRODUCTION

The rare earth elements (REE) are routinely used as activators in luminescence materials' synthesis. With the increase of price of REE, suitable and cheaper replacement is needed, with transition elements (TE) as the most promising candidates. However, proper coordination of transition elements atoms within the host lattice is crucial to their luminescent properties – the defects can significantly decrease the luminescence activity of TE phosphors. During the years, several preparation methods for inorganic REE-based phosphors have been introduced, including solid-state synthesis [1], sol-gel methods [2], flame synthesis [3], and spray pyrolysis [4].

EXPERIMENTAL

Two different matrix composition were studied – the Åkermanite – calcium magnesium silicate ($\text{Ca}_2\text{MgSi}_2\text{O}_7$) from the melilite sorosilicates group and its strontium-

substituted version ($\text{Sr}_2\text{MgSi}_2\text{O}_7$). The desired manganese and cerium content within samples was 1.5 and 1.0 mol % respectively.

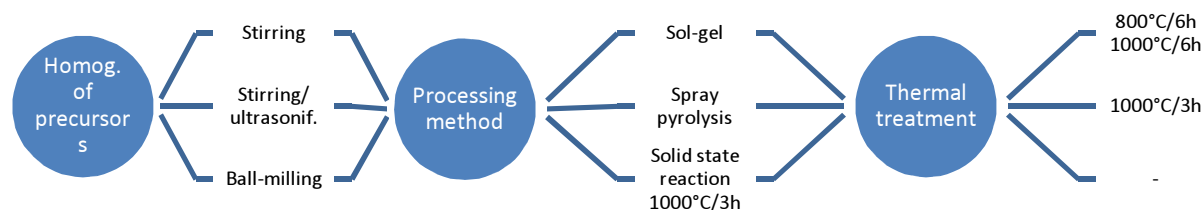


Fig. 1: Scheme of utilized preparation methods

The sol-gel (SG) samples have been prepared by modified Pechini method (MPM) used in our previous work [3]. The solution of corresponding nitrates has been mixed thoroughly and subsequently the citric acid and ethylene glycol have been introduced into the solution. The resulting solution was left to react at 85°C for 3 hours. After evaporation of solvent at 140°C for 16 hours the samples were calcinated for 2x6 hours at 800°C and 1000°C. The spray pyrolysis (SP) samples were prepared by mixing the respective nitrates solutions and TEOS and by subsequent pyrolysis of ultrasonically atomized solution in spray pyrolysis apparatus (Fig. 2). The samples were then calcined at 1000°C for 3 hours to remove possible nitrate and organic residua.

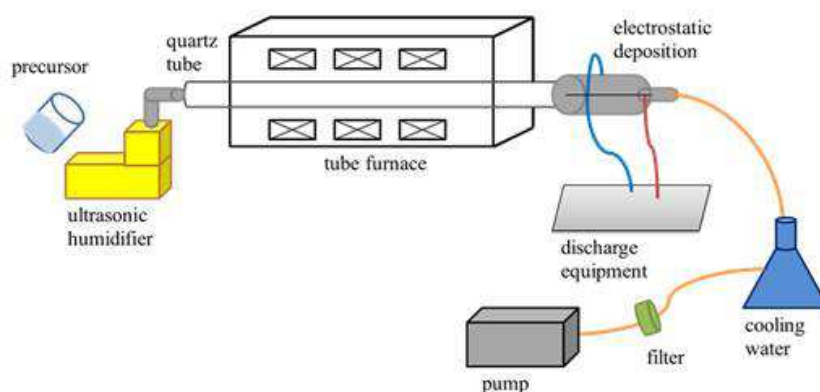


Fig. 2: Schematic of spray pyrolysis apparatus, as shown in [4]

The solid state reaction samples (SSR) were prepared by ball-milling of CaCO_3 , MgCO_3 , SiO_2 and MnO_2 precursors for 10 hours and subsequent calcination at 1000°C for 3 hours. Due to the design of our previous experiments, the solid state reaction samples were doped with manganese only (1.5% mol.). This partially obscures the comparison of luminescence properties; however, the phase homogeneity of the powder can still

be compared using the X-ray powder diffraction analysis. The presence of secondary phases is undesirable and the goal is to achieve uniform single phase composition of the phosphor.

The samples were analysed by energy-dispersive X-ray spectroscopy on JEOL JSM 7600 F/EDS/WDS/EBS. The phase composition was determined using X-ray powder diffractometer Panalytical Empyrean DY1098. The fluorescence emission spectra (excitation wavelength 330nm) of prepared powders were measured using fluorescence spectrometer Horiba Fluorolog 3.

RESULTS AND DISCUSSION

The results of X-ray diffraction phase analysis are summarized in Fig. 3. The SSR-prepared powders were strongly crystalline and consisted of at least two phases, one being Ca-åkermanite $\text{Ca}_2\text{MgSi}_2\text{O}_7$ and a secondary phase – $\text{Ca}_3\text{MgSi}_2\text{O}_8$ (merwinite) (Fig. 3a).

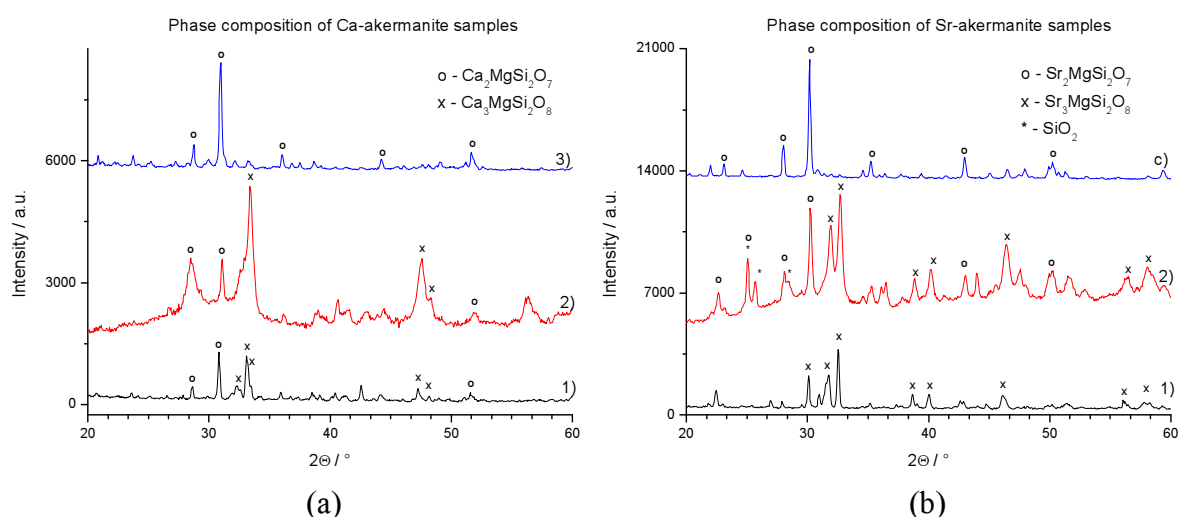


Fig. 3: Comparison of phase composition of Ca-åkermanite (a) and Sr-åkermanite (b) samples 1) SSR preparation route, 2) SG preparation route, 3) SP preparation route

The nature of phase composition in Sr-åkermanite was quite similar to the calcium-åkermanite; all samples contained some portion of main strontium-åkermanite phase, and in case of SSR and SG samples, also some minor portion of Sr-merwinite phase (Sr analogue of merwinite, i.e. $\text{Sr}_3\text{MgSi}_2\text{O}_8$) – Fig. 3b.

The Fig. 5 and 5 show the influence of matrix composition on luminescence spectra of SG and SP prepared powders. The strongest intensities were measured for Sr-based sol-gel and spray pyrolysis samples (compared to Ca-based samples prepared by the same methods).

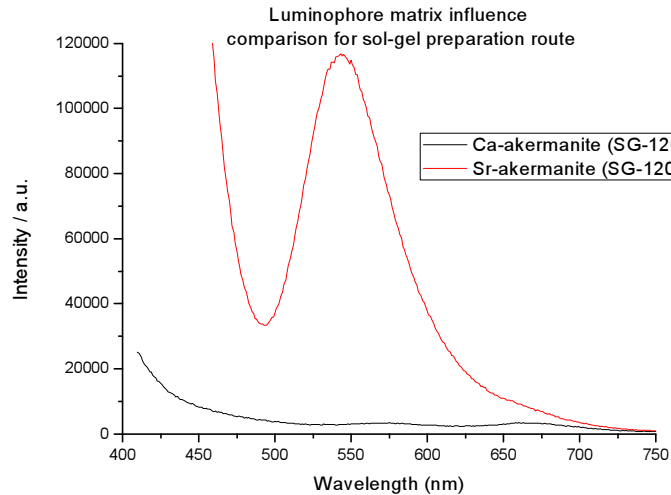


Fig. 4: Luminescence of Ca-akermanite and Sr-akermanite for SG synthesis route

The samples prepared by SG route showed minor shift in luminescence spectra towards the lower wavelengths (the emission peak maximum of SG synthesis route prepared samples located at 550nm vs. 570-580nm for SP synthesis route prepared samples).

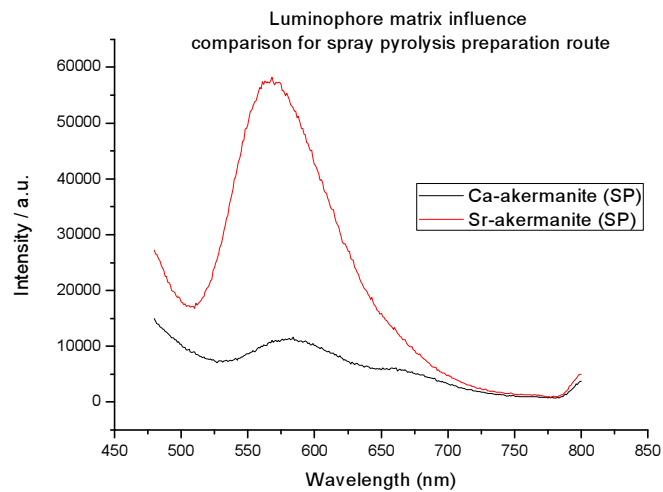


Fig. 5: Luminescence of Ca-akermanite and Sr-akermanite for SP synthesis route

One theory is that this is due to different phase composition of samples prepared by SG route – the influence of merwinite phase. Alternatively, the shift could be due to larger size of Sr cations and therefore expansion of crystal lattice, resulting in crystal field distortion. That could potentially enlarge the energy gap between the base and the excited state, thereby shifting the wavelength of emitted photons towards the blue region. However, these hypotheses require further investigation to verify the real mechanism of the shift.

CONCLUSIONS

It was found that the spray pyrolysis yields phosphors with composition of single akermanite (or strontium-akermanite) phase, while sol-gel preparation route yielded phosphors containing two phases – akermanite and merwinite, or their respective strontium analogues. The strontium-based matrix composition seems to be beneficial for luminescence applications – the intensities of luminescence for strontium – based samples were significantly higher than for calcium-based compositions.

ACKNOWLEDGEMENT

The support of the project SAS-NSC JRP-2012/14 and the grant VEGA 1/0631/14 is gratefully acknowledged. This publication was created in the frame of the project "Centre of excellence for ceramics, glass, and silicate materials" ITMS code 262 201 20056, based on the Operational Program Research and Development funded from the European Regional Development Fund.

LITERATURE

- [1] Herval, L.K.S. , et al., Enhancement of the luminescence intensity by co-doping Mn^{2+} into Er^{3+} -doped $SrAl_2O_4$, Journal of Luminescence, Volume 163, July 2015, Pages 17-20
- [2] Pan, W., et al. , Sol-gel processed Ce^{3+} , Tb^{3+} codoped white emitting phosphors in $Sr_2Al_2SiO_7$, Journal of Rare Earths, Volume 26, Issue 2, April 2008, Pages 207-210
- [3] Prnová, A. , Bodišová, K. , Klement, R. , Preparation and characterization of Yb_2O_3 – Al_2O_3 glasses by the Pechini sol–gel method combined with flame synthesis, Cer. Int., Vol. 40, Iss. 4, (2014), pp. 6179-6184
- [4] National Taiwan University of Science and Technology. Method for preparing silver particles and core-shell silver particles. Inventors: SHIH Shao-ju, CHIEN I-Chen, WU Yu-Hsuan. United States patent application. US2015010769 (A1). 08.01.2015
